

Charles University in Prague
Faculty of Mathematics and Physics

DOCTORAL THESIS



Zoltán Mics

Dynamics of delocalized states in molecular systems studied by time-resolved THz spectroscopy

Department of Chemical Physics and Optics

Supervisor: RNDr. Petr Kužel, Dr.,

Consultants: Hynek Němec PhD., doc. RNDr. Pavel Jungwirth
DSc.,

Study programme: Physics

Specialization: Quantum Optics and Optoelectronics

Prague 2012

Acknowledgments

There are many people to whom I would like to express my gratitude for their help in completing of this thesis.

I am grateful to my supervisor, Petr Kužel, for his guidance and support. I have learnt from him almost everything I know about nonlinear optics and THz spectroscopy. I appreciate very much his critical reading of the present manuscript, which resulted in great improvement of the thesis.

I would like to thank Pavel Jungwirth for his valuable advice on the photochemistry of water. I am also indebted to Stephen E. Bradforth for a help with the equipment for the experiments with water and for useful discussions.

The investigation of nanocrystalline materials could not be carried out without Hynek Němec. He has introduced me into this topic and the interpretation of data were largely based on the Monte Carlo simulations of carrier mobility which he developed. I am grateful to him also for reading very carefully the thesis. His suggestions greatly contributed to its improvement.

I appreciate the help of Ivan Rychetský and the discussions I had with him on various models of effective medium theory. I would like to thank Martin Kempa for the microwave measurements on pellets of NTO. I am also indebted to Dina Fattakhova-Rohlfing for providing these samples.

I would like to thank Petr Malý and Petr Němec for the preparation of the nanocrystalline CdS samples and for the discussions on the investigation of this material. I am grateful to Petr Formánek for the measurement of the transmission electron microscope image of nanocrystalline CdS films.

I would like to thank all members of the THz group for the helpful and friendly atmosphere.

Last but not least, I am grateful to my parents and to my friends for their emotional support.

This thesis was financially supported by the Czech Science Foundation (project 202/09/H041), Charles university in Prague (grant SVV-2010-261306) and the Ministry of Education of the Czech republic (project LC-512).

I declare that I carried out this doctoral thesis independently, and only with the cited sources, literature and other professional sources.

I understand that my work relates to the rights and obligations under the Act No. 121/2000 Coll., the Copyright Act, as amended, in particular the fact that the Charles University in Prague has the right to conclude a license agreement on the use of this work as a school work pursuant to Section 60 paragraph 1 of the Copyright Act.

Prague, 13 January 2012

Zoltán Mics

Contents

1	Preface	5
2	Charge transport and localization	9
2.1	Effective medium theory	12
2.1.1	Maxwell-Garnett theory	15
2.1.2	Bruggeman theory	18
2.2	Models of conductivity spectra	19
2.2.1	Drude model	19
2.2.2	Oscillator model	20
2.2.3	Debye model	21
2.2.4	Hopping	21
2.2.5	Generalized Drude models	22
2.2.6	Drude-Smith model	22
2.2.7	Monte-Carlo simulations of charge transport in semiconductor nanocrystals	25
3	Experimental methods and data analysis	33
3.1	Basics of THz spectroscopy	34
3.1.1	Generation of THz pulses	34
3.1.2	THz detection	36
3.2	Steady-state THz spectroscopy	37
3.2.1	Experimental setup	37
3.2.2	Data analysis	38
3.3	Optical pump–THz probe spectroscopy	40
3.3.1	Experimental setup	42
3.3.2	Data analysis	42
3.3.3	Quasi-steady state approximation	45
3.3.4	Analysis of ultrafast dynamics	47
3.4	Optical pump–optical probe spectroscopy	49
3.4.1	Experimental setup	49
3.4.2	Data analysis	50

4	Electron transport in niobium-doped titania nanoparticles	53
4.1	Sample preparation and properties	53
4.2	Measurement	54
4.3	Model of the effective permittivity	55
4.4	Effective medium theory	56
4.5	Results	60
4.6	Conclusion	62
5	Electron dynamics in water	65
5.1	Theoretical background	65
5.2	Specific experimental details	68
5.3	Experimental results and discussion	71
5.4	Conclusion	76
6	Electron transport in nanocrystalline and bulk ZnO	79
6.1	Recent THz studies of bulk and nanocrystalline ZnO	80
6.1.1	Bulk ZnO	80
6.1.2	Nanocrystalline ZnO	82
6.2	Electron mobility and dynamics in bulk ZnO	83
6.2.1	Conclusion	93
6.3	Electron mobility and dynamics in nanocrystalline ZnO	96
6.3.1	Conclusion	100
6.4	Challenges and outlook for the study of carrier transport in ZnO .	104
7	Electron transport in nanocrystalline CdS	105
7.1	Spectral response of carriers	107
7.2	Ultrafast electron dynamics	112
7.3	Electron mobility spectra for high excitation densities. Fermi-Dirac statistics.	121
7.4	Electron transport at low temperatures	127
7.5	Conclusion	128
8	Conclusion	131

Summary

Title: Dynamics of delocalized states in molecular systems studied by time-resolved THz spectroscopy

Author: Mgr. Zoltán Mics

Institute: Institute of Physics, Academy of Sciences of the Czech Republic

Supervisor: RNDr. Petr Kužel, PhD.

Supervisor's e-mail address: kuzelp@fzu.cz

Abstract: This thesis is devoted to a study of the conductivity of confined charge carriers in various nanocrystalline materials. The experimental method – THz spectroscopy – involves measurements of the conductivity of carriers generated by doping or by optical excitation. In the theoretical interpretation of measured data we address important aspects of carrier transport, connected to the microscopic inhomogeneity of samples and the nanoscale confinement of carriers. We focus on the study of nanocrystalline ZnO and CdS using simulations and experiments in a wide range of carrier densities and for several temperatures. In ZnO, the interplay of highly mobile electron-hole gas, dense electron-hole plasma and population of excitons was observed. In CdS the investigation reveals the importance of clusters of nanocrystals in the electron confinement. The dynamics of the electron mobility at different carrier densities show the role of the kinetic energy of electrons and its relaxation in the carrier transport in nanostructured systems. At temperatures 20 K and at low carrier densities a crossover between localized transport and Drude-like free electron behaviour was observed for the first time.

Keywords: THz time-resolved spectroscopy, carrier mobility and transport, effective medium theory, Monte Carlo method, nanocrystals

Název: Studium dynamiky delokalizovaných stavů v molekulových systémech pomocí časově rozlišené THz spektroskopie

Autor: Mgr. Zoltán Mics

Ústav: Fyzikální ústav Akademie věd České republiky

Školitel: RNDr. Petr Kužel, PhD.

E-mail adresa školitele: kuzelp@fzu.cz

Shrnutí: Tato práce je zaměřena na studium vodivosti lokalizovaných nositelů náboje v různých nanokrystalických materiálech. Použitá experimentální metoda – THz spektroskopie – umožňuje měření vodivosti nositelů generovaných

dotováním nebo optickou excitací. Při interpretaci naměřených dat bereme v úvahu důležité aspekty transportu náboje, související zejména s nehomogenitou vzorků na mikroskopické úrovni a s omezením pohybu nosičů v důsledku lokalizace. Těžiště práce tvoří studium nanokrystalického ZnO a CdS za použití experimentů a simulací v širokém rozsahu hustoty nosičů a teplot. V ZnO byla pozorována současně přítomnost nosičů s velikou pohyblivostí, hustého elektron-děrového plazmatu a excitonů. Ve vzorcích CdS naše studium odhaluje klíčovou roli klastrů nanokrystalů při lokalizaci náboje. Dynamika pohyblivosti elektronů poukazuje na význam kinetické energie elektronů a její relaxace pro transport náboje. Při teplotě 20 K a při nízké hustotě nosičů jsme poprvé pozorovali přechod mezi režimy lokalizovaných a zcela volných nositelů náboje. **Klíčová slova:** časově rozlišená THz spektroskopie, pohyblivost a transport náboje, efektivní prostředí, metoda Monte Carlo, nanokrystaly

Cím: Delokalizált elektronok dinamikájának vizsgálata molekuláris rendszerekben időfelbontott THz spektroszkópia segítségével

Szerző: Mgr. Mics Zoltán

Intézet: Fizikai Intézet, Cseh Tudományos Akadémia

Témavezető: RNDr. Petr Kužel, PhD.

A témavezető e-mail címe: kuzelp@fzu.cz

Összefoglaló: A jelen munka lokalizált töltések vezetőképességének a vizsgálatával foglalkozik különböző nanokristályos anyagokban. A felhasznált kísérleti módszer THz spektroszkópia, amely lehetővé teszi fény vagy adalékolás segítségével létrehozott töltéshordozók vezetőképességének a mérését. A kísérleti eredmények kiértékeléséhez és interpretációjához szükséges a nanokristályos anyagok egyedi tulajdonságainak a figyelembe vétele: a legfontosabb ezen anyagok inhomogenitása és a töltéshordozók lokalizációja. A munka fő témája nanokristályos CdS és ZnO vizsgálata mérések és szimulációk segítségével különböző hőmérsékleteken és a töltéshordozók sűrűségének széles skáláján. Cink-oxidban nagy mozgékonyaságú töltéshordozókat, elektron-lyuk plazmát és excitonokat figyeltünk meg. Kadmium-szulfidban eredményeink megmutatják a nanokristályok klasztereinek a jelentőségét a töltéshordozók lokalizációjában. Az elektronok mozgékonyaságának a dinamikája rávilágít az elektronok mozgási energiájának és annak relaxációjának a szerepére az elektromos töltés transzportjában. 20 K hőmérsékleten és alacsony elektron sűrűség mellett megfigyeltük, hogy az elektronok lokalizációja megszűnik és mozgékonyaságuk a Drude modellel írható le.

Kulcsszavak: időfelbontott THz spektroszkópia, elektromostöltés-transzport, effektív közeg, Monte Carlo módszer, nanokristály

Chapter 1

Preface

Electron transport plays a crucial role in every aspect of electronics. It is well understood in bulk materials and at their interfaces (PN junctions etc.). Recently, nanotechnology – the technology of fabrication of nanoobjects – emerged as a promising way to develop new types of electronic elements with improved parameters. The improvements often originate from the special features of nanodevices like reduced dimensionality, high surface/volume ratio etc. For example, dye-sensitized nanocrystals are used to improve the efficiency of Grätzel solar cells. Here the light from the Sun is absorbed in the dye layer which leads to electron injection into nanocrystals, thus generating electric current. Due to the high surface/volume ratio of nanocrystals the light harvesting is enhanced compared to dye-sensitized, bulk semiconductors. Owing to an efficient generation of conducting electrons, dye-sensitized nanocrystalline solar cells are a promising cheap alternative to conventional solar cells based on PN junctions. [2]

Grätzel cells are also an example of application of nanomaterials where the electron transport becomes essential. The electron localization in these cells can lead to a reduction of the conductivity in comparison with bulk materials. Consequently, the conversion of photon energy to the electric current may become less efficient. This example and a number of others which can be easily found in the literature show that it is important to understand the mechanisms of carrier transport in nanostructured materials. Still a large number of open questions exists in this topic and this thesis aims to contribute to the solution of a number of them, such as the role of depolarization fields and the impact of the carrier backscattering on grain boundaries. A review of the current state of understanding of the carrier transport in nanostructured systems is presented in Chapter 2.

In the applications, the most important quantity is usually the dc conductivity. Nevertheless, a study of the ac conductivity may provide essential information about the nature of electron transport on shorter length scales, and therefore it can finally lead to a better understanding of the dc transport and of the ways how to improve it. The frequency range 0.1-3 THz, commonly referred to as the THz

frequency range, has been shown to contain the pertinent information about the carrier transport on the nanoscale. [3–6] The diffusion length of charge carriers during the period of a THz electromagnetic wave is typically several or tens of nanometers in semiconductors. Consequently, determining the conductivity in the THz range can reveal characteristic fingerprints of carrier transport inside nanoobjects as well as between them. This is the reason why we have chosen THz spectroscopy to study the carrier transport in nanomaterials. To probe the sample in equilibrium, THz time-domain spectroscopy is used. This is useful for materials where the conducting carriers are generated by doping. The conductivity of a sample out of equilibrium (i.e. with photoinjected carriers) is studied by time-resolved THz spectroscopy. Both types of measurements are described in detail in Chapter 3.

We take the following advantages of THz spectroscopy:

- THz spectroscopy is phase-sensitive – from one measurement, the real and the imaginary parts of the conductivity can be obtained simultaneously for the entire THz frequency range.
- The conductivity is measured in a non-contact way, without the need of electrodes on the sample. Connecting an electrode to semiconductor nanocrystals with good conductive coupling is a difficult task.
- In THz spectroscopy, pulsed radiation is used. Consequently, it is straightforward to perform time-resolved THz measurements, i.e. to probe the THz conductivity of an optically excited sample. In this case the transport of photogenerated carriers is studied. By changing the excitation power, the number of photogenerated carriers can be controlled. This opens up a simple possibility to tune the contrast of the conductivity between the constituents of the (inhomogeneous) nanomaterials; for example, between semiconductor nanocrystals and the nonconducting matrix filling the voids among the nanocrystals. This way, the effect of the inhomogeneities on the conductivity of the nanomaterial can be explored. By changing the time delay between the optical excitation pulse and the THz probe pulse the decay of the conductivity of the carriers can be examined with subpicosecond time resolution.

In Chapter 4 equilibrium THz spectroscopy is used for the investigation of carrier transport in pellets of niobium-doped TiO₂ nanoparticles. This material has a potential in applications as a nanostructured transparent conductive oxide. To explain the THz response of the material a model of effective medium theory based on the Bergman theorem is developed, which accounts for both percolated and isolated nanocrystals. The effective medium theory in combination with carrier hopping gives a complete picture about the response of the nanocrystalline material for different preparation conditions.

In the rest of the thesis the transport of carriers generated by optical excitation is studied using time-resolved THz spectroscopy. The measurements are supplemented with classical Monte Carlo simulations of the carrier thermal motion. The simulations connect the carrier mobility with the fundamental parameters of carrier motion and localization, such as carrier scattering time, probability of backscattering from nanocrystal boundaries etc. It means that a comparison of simulated and measured carrier mobility can directly yield these parameters.

In Chapter 5 we are looking for delocalized electron states in water and aqueous solutions immediately after photoexcitation. The lack of signal from these electrons allows us to estimate the maximum possible degree of delocalization of these states. The expected mobility of electrons was obtained from Monte Carlo simulations. This study can serve also as an evaluation of the possibilities and limitations of THz spectroscopy in the study of mobile carrier states.

In Chapter 6 the carrier transport in bulk and nanocrystalline ZnO is studied. ZnO is an interesting material with high exciton binding energy which leads to a significant population of exciton states even at high temperatures. The study is carried out at different temperatures and in a wide range of carrier densities. In nanocrystalline ZnO, the mobility of carriers is modeled using Monte Carlo simulations.

In Chapter 7 the carrier transport is investigated in nanocrystalline CdS prepared by chemical bath deposition. This material is used in new generation Cu(In, Ga)Se₂ solar cells as a buffer layer. From the comparison of simulations and measurements it is revealed that electron localization occurs on two length scales corresponding to nanocrystals and their clusters. We show a direct connection between the structure of nanocrystalline CdS and its photoconductivity spectra. Moreover, a connection between the kinetic energy of carriers and their degree of localization is observed.

Chapter 2

Charge transport and localization

Electromagnetic radiation interacts with charged particles in the irradiated material. Under the effect of the electromagnetic field the charges move. This motion results in the generation of electric polarization for bound charges or in the transport of free charge carriers – electric current – and it is described by a dielectric response function. (In this thesis we focus on nonmagnetic materials, therefore only electric phenomena will be discussed.) For example in an isotropic linear material the generated time-dependent electric current originates from the time-dependent electric field as follows:

$$j(t) = \int_{-\infty}^t \Omega(t-t') E(t') dt' \quad (2.0.1)$$

where $j(t)$ is the generated current, $E(t)$ the local electric field and $\Omega(t)$ the response function of the system of free carriers. The electromagnetic field is more frequently represented by its spectrum, so it is useful to apply the Fourier transform to the equation 2.0.1:

$$j(\omega) = \sigma(\omega) E(\omega) \quad (2.0.2)$$

where $\omega = 2\pi f$ is the angular frequency of the electromagnetic radiation and $\sigma(\omega)$ is the conductivity of the system. For a system consisting of identical free carriers it is often convenient to normalize the conductivity by the charge density of the free carriers Ne_0 . In this case the mobility as a response function of a single unit charge is obtained:

$$\mu(\omega) = \frac{\sigma(\omega)}{Ne_0} \quad (2.0.3)$$

For bound charges, a similar equation as Eq. 2.0.2 can be derived between the induced polarization and the applied electromagnetic field :

$$P(\omega) = \varepsilon_0 \chi(\omega) E(\omega) \quad (2.0.4)$$

where $\chi(\omega)$ is the dielectric susceptibility of the system of bound charges. However, the dielectric permittivity $\varepsilon = 1 + \chi$ is used more frequently to describe the dielectric properties of a material with bound charges. It relates together the electric field and the electric displacement field in the material:

$$D(\omega) = \varepsilon_0 E(\omega) + P(\omega) = \varepsilon_0 E(\omega) (1 + \chi(\omega)) = \varepsilon_0 \varepsilon(\omega) E(\omega) \quad (2.0.5)$$

The two properties – conductivity and permittivity are introduced intuitively as convenient response functions for two qualitatively different simple systems, where the free and bound charges can be clearly distinguished. However, in nanoscaled systems the properties of charge localization or delocalization may depend on the length scale (related to the probing frequency), time scale and e.g. carrier energy. This smears the principal difference between localized and delocalized carriers: a carrier which appears as bound in one experiment may behave as free in another one. Therefore it is convenient to describe the free and bound charges on an equal footing by a generalized permittivity and conductivity, which become now equivalent and are related by the equation:

$$\varepsilon(\omega) = \frac{i\sigma(\omega)}{\omega\varepsilon_0} \quad (2.0.6)$$

Both these quantities describe equivalently the response of any dielectric and conducting system. As mentioned above, in some systems it cannot be definitely determined whether the probed charge carriers are free or bound. A good example is a system of conducting nanocrystals located in a nonconducting matrix, where the electrons can move inside the nanocrystals but cannot be transferred between nanocrystals. Then the DC conductivity ($\omega = 0$) is zero and the electrons can be considered as bound. However, at high frequencies, where the diffusion length during one period of the electromagnetic field is smaller than the size of the nanocrystals, the electrons appear to be free. In our experiments and further analysis these charge carriers are typically the objects to be examined and we will use the complex conductivity $\sigma_{carrier}$ or mobility to describe their dielectric response. The rest of the material response will be characterized by its background permittivity $\varepsilon_{background}$. The total permittivity of the material then reads:

$$\varepsilon_{NC}(\omega) = \varepsilon_{background}(\omega) + \frac{i\sigma_{carrier}(\omega)}{\omega\varepsilon_0} \quad (2.0.7)$$

When examining photoexcited nanocrystalline semiconductors, the background permittivity is simply the permittivity of the sample without photoexcitation and the conductivity of the photoexcited carriers is directly measured. In doped semiconductors we are interested in the conductivity/mobility of the charge carriers introduced by doping and of the intrinsic charge carriers.

From the shape of the spectra and from its dependence e.g. on the carrier concentration or on the temperature we attempt to deduce a quantitative model for the motion of charge carriers in nanocrystalline materials. The difficulty of this task in nanostructured materials lies in two important aspects: [6]

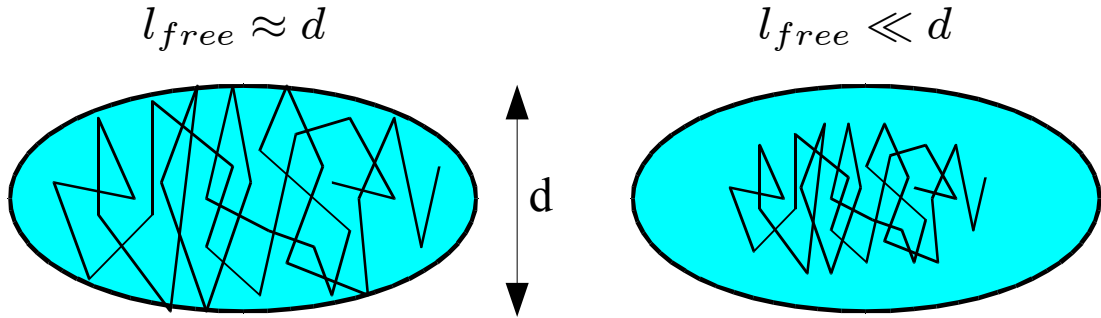


Figure 2.1: Illustration of the carrier movement in a nanoscopic object. If the mean free path of carriers is comparable with the size of the object, the scattering of carriers on the boundaries can significantly change their microscopic mobility. In a large object, i.e. when their size is much larger than the mean free length, the carriers' movement (and microscopic mobility) is similar to that in bulk materials.

- The movement of charge carriers is directly affected by the local electric field acting on them. However, nanocrystalline materials are inhomogeneous and the local field may differ from the electric field of an external electromagnetic wave probing the sample (macroscopic field). Therefore the **microscopic (or intrinsic) mobility** of carriers μ_{micro} (i.e. the carrier response to the local electric field) and the **macroscopic mobility** μ_{macro} (the carrier response to the externally applied electric field) can be substantially different. Let us consider again the system of conducting nanocrystals in an isolating matrix as an example. If the mean free path of the carriers moving in the nanocrystals is much shorter than the nanocrystal size, their microscopic conductivity is the same as it would be in a bulk semiconductor. However, if we examine the macroscopic dielectric response of the material (for example, by measuring its THz transmission or by applying a low frequency electric field), we come to the conclusion that its spectral shape cannot resemble that of the bulk crystal in some frequency range. [6, 7] In particular, the low frequency part of the spectra is more affected by this effect as it can be deduced from the simple fact that the macroscopic DC conductivity of the sample is zero, whereas the DC microscopic conductivity is non-zero. The relation between the microscopic and macroscopic conductivities is established by effective medium theory (see Section 2.1).
- The mechanisms of the microscopic conductivity, i.e. the nature of carrier motion in nanocrystalline materials can be complex. It depends both on the character of the motion in the bulk (e.g. band-like motion or hopping) and on the interaction of carriers with the nanocrystal boundaries (isotropic scattering, backscattering, energy barriers) (see Fig. 2.1). Depending on the morphology of the nanostructure several different transport mechanisms can occur on different time and length scales. A review of the models describing

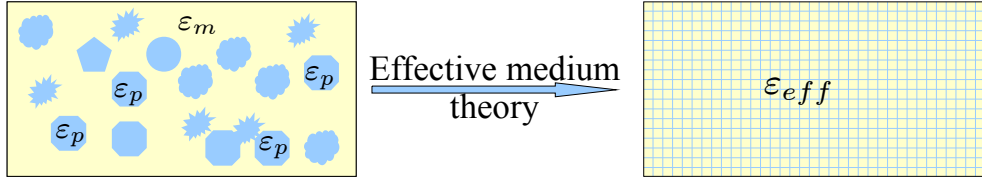


Figure 2.2: Illustration of the averaging procedure of effective medium theory.

the microscopic conductivity will be given in Section 2.2.

In this chapter we summarize the existing approaches for modelling these aspects.

2.1 Effective medium theory

The dielectric properties of a composite inhomogeneous system are characterized by its complex dielectric function, which is a function of position. If the inclusions are much smaller than the wavelength of the probing electromagnetic radiation, but large enough that they can be characterized by a dielectric function ($\geq 10 \text{ \AA}$), the material can be treated as dielectrically homogeneous with an effective dielectric function. The effective medium theory is used in the averaging process, i.e. in relating the geometrical arrangement and dielectric properties of components to the effective dielectric function (see Fig. 2.2):

$$\varepsilon_{eff} = EMT(s_1, \varepsilon_1, \dots, s_n, \varepsilon_n, \text{morphology}) \quad (2.1.1)$$

where n is the number of the components, s_j and ε_j are the volume fraction and the permittivity of the components, respectively. Clearly $\sum s_j = 1$ is valid. Based on equation 2.0.7 the dielectric permittivity of the components and the effective permittivity of the homogenized medium can be all decomposed into two contributions: a background permittivity and the conductive contribution of mobile charges. This decomposition allows us to write a relation between the effective (macroscopic) conductivity σ_{eff} and the (microscopic) conductivities $\sigma_1 \dots \sigma_n$ of the components:

$$\sigma_{eff} = -i\omega\varepsilon_0 \left[EMT\left(s_1, \varepsilon_1 + \frac{i\sigma_1}{\omega\varepsilon_0}, \dots, s_n, \varepsilon_n + \frac{i\sigma_n}{\omega\varepsilon_0}\right) - EMT(s_1, \varepsilon_1, \dots, s_n, \varepsilon_n) \right] \quad (2.1.2)$$

In order to get a useful connection between the macroscopic and microscopic response, the behaviour of the function EMT must be more specifically given. In this thesis we examine two-component systems, where generally one component forms inclusions in the other one considered as a matrix. For two-component systems, the Bergman theorem is the most concrete yet general representation of effective medium theory. [8] The theorem connects the effective dielectric function

of a two-phase composite with the morphology of the composite described by the spectral function $G(L)$ and with the dielectric functions of the components:

$$\varepsilon_{eff} = \varepsilon_2 \left(1 - s \int_0^1 \frac{G(L)}{\frac{\varepsilon_2}{\varepsilon_2 - \varepsilon_1} - L} dL \right) \quad (2.1.3)$$

where ε_1 and ε_2 are the permittivities of the components, s is the volume fraction of the first component (with permittivity ε_1). The spectral function $G(L)$ has the following interpretation:

- The percolated part of the component ε_1 contributes to $G(L)$ a Dirac delta function at $L = 0$: $G(L) = 2C_1 \delta(L)$. The integral in equation 2.1.3 then yields $sC_1 \frac{\varepsilon_1 - \varepsilon_2}{\varepsilon_2}$, where C_1 is called the strength of percolation of the component 1.
- For $L > 0$ the spectral function $G(L)$ represents the contribution from different shapes of inclusions in the system. L is called the depolarization factor of the inclusion. The depolarization factor L determines the depolarization field \mathbf{E}_d induced in the object placed into a uniform electric field:

$$\mathbf{E}_d = -L \frac{\mathbf{P}}{\varepsilon_0} \quad (2.1.4)$$

where \mathbf{P} is the electric polarization induced by the local electric field. The value of L depends on the geometrical shape of the inclusion and on its orientation with respect to the applied field. For example $L = 1/3$ for a spherical inclusion; for a needle $L = 0$ if the field is oriented along the needle and $L = 1/2$ if it is perpendicular; for a thin infinite plate $L = 1$ if the field is perpendicular to the disc and $L = 0$ for an in-plane field. $G(L)$ then represents the distribution of the contributions to the total dielectric function of shapes with the depolarization factor L . All such contributions are summed up in equation 2.1.3.

The spectral function has to fulfill the following normalization condition: [9]

$$\int_0^1 G(L) dL = 1 \quad (2.1.5)$$

And additionally for isotropic systems:

$$\int_0^1 L G(L) dL = \frac{1-s}{3} \quad (2.1.6)$$

We now use the Bergman theorem to study the properties of the effective medium theory on the system most extensively studied in this thesis: nanocrystalline semiconductor inclusions in a non-conducting matrix. By substituting 2.1.3 into 2.1.2 and assuming that the second component is an insulator (i.e. $\sigma_2 = 0$), we get an equation relating the microscopic conductivity of inclusions to the measured macroscopic conductivity:

$$\sigma_{eff} = s \varepsilon_2^2 \int_0^1 \frac{G(L)}{\varepsilon_2 - L(\varepsilon_2 - \varepsilon_1)} \frac{\sigma_1}{\varepsilon_2 - L(\varepsilon_2 - \varepsilon_1) + \frac{i\sigma_1 L}{\omega \varepsilon_0}} dL \quad (2.1.7)$$

From this equation the contribution of the percolated part of the material to the macroscopic conductivity can be evaluated. By substituting the percolated part of the spectral function $2C_1\delta$ into the equation one finds $\sigma_{percolated} = 2sC_1\sigma_1$. Therefore the percolated part of the nanocrystals contributes to the macroscopic conductivity with a term proportional to the microscopic conductivity. If the components of the spectral functions with $L \neq 0$ become dominant, the effective conductivity exhibits a saturation behaviour for an increasing microscopic conductivity σ_1 (i.e. for an increasing pump fluence). To make this analysis even more specific, we choose a commonly used model for the microscopic conductivity of nanocrystals; if the nanocrystals are much larger than the carrier mean free path in the material, the microscopic conductivity of the nanocrystals follows the Drude formula:

$$\sigma_1(\omega) = \frac{Nq^2\tau}{m} \frac{1}{1 - i\omega\tau} \quad (2.1.8)$$

where N is the carrier density, m is the effective mass, τ is their momentum scattering time and q the carrier charge. By substituting 2.1.8 into the equation 2.1.7, we obtain:

$$\sigma_{eff} = s \varepsilon_2^2 \frac{Nq^2}{m} \int_0^1 \frac{G(L)}{(\varepsilon_2 - L(\varepsilon_2 - \varepsilon_1))^2} \frac{-i\omega}{\omega_0(L)^2 - \omega^2 - \frac{i\omega}{\tau}} dL \quad (2.1.9)$$

Therefore the non-percolated parts with a specific depolarization coefficient contribute with an oscillator-like response to the macroscopic conductivity. The frequency of resonance depends on the plasma frequency and the depolarization coefficient:

$$\omega_0(L) = \sqrt{\frac{Nq^2}{\varepsilon_0 m} \frac{L}{\varepsilon_2 - L(\varepsilon_2 - \varepsilon_1)}} = \sqrt{\frac{L}{\varepsilon_2 - L(\varepsilon_2 - \varepsilon_1)}} \times \omega_p \quad (2.1.10)$$

In some cases the geometrical arrangement of nanocrystals is not complicated and it is possible to assume a simple model for the spectral function. The next subsections discuss some of these models. In other cases a special functional form is assumed, which is known to give good results for a large variety of systems with the correct parametrization. [9, 10]

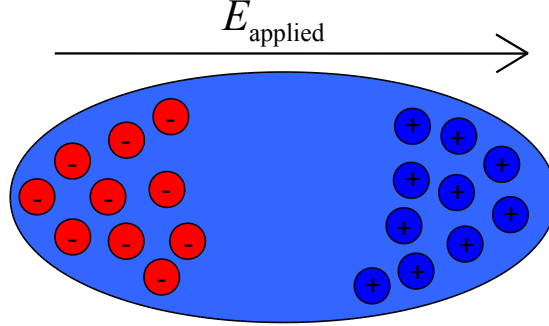


Figure 2.3: Illustration of charge separation in a conducting inclusion under the effect of external electric field. The electric field drives the charge carriers to the opposite sides of the inclusion. The attracting electric force between the carriers of opposite charge leads to their oscillation in an oscillating electric field.

2.1.1 Maxwell-Garnett theory

The Maxwell-Garnett theory is one of the simplest and most widely used effective medium theories. [11] It assumes that one component forms small ellipsoidal particles sparsely embedded in a matrix composed of another material – the second component. The distance of the particles is much larger than their size. In such a case, the effective permittivity of the material is related to the properties of the components by the following equation: [11]

$$\frac{\varepsilon - \varepsilon_m}{\varepsilon + K\varepsilon_m} = s \frac{\varepsilon_p - \varepsilon_m}{\varepsilon_p + K\varepsilon_m} \quad (2.1.11)$$

where ε is the effective permittivity of the composite material, ε_p is the permittivity of the particles, K is the shape factor of the particles (2 for spheres and 1 for cylinders perpendicular to the applied field or to the polarization of the probing radiation), ε_m is the permittivity of the matrix in which the particles are embedded.

To establish a relation between the conductivity of the effective medium and the conductivity of the components the equation 2.1.11 can be generalized in the same way as the equation 2.1.1:

$$\frac{\varepsilon + \frac{i\Delta\sigma}{\omega\varepsilon_0} - \left(\varepsilon_m + \frac{i\Delta\sigma_m}{\omega\varepsilon_0}\right)}{\varepsilon + \frac{i\Delta\sigma}{\omega\varepsilon_0} + K \left(\varepsilon_m + \frac{i\Delta\sigma_m}{\omega\varepsilon_0}\right)} = s \frac{\varepsilon_p + \frac{i\Delta\sigma_p}{\omega\varepsilon_0} - \left(\varepsilon_m + \frac{i\Delta\sigma_m}{\omega\varepsilon_0}\right)}{\varepsilon_p + \frac{i\Delta\sigma_p}{\omega\varepsilon_0} + K \left(\varepsilon_m + \frac{i\Delta\sigma_m}{\omega\varepsilon_0}\right)} \quad (2.1.12)$$

where $\Delta\sigma_p$, $\Delta\sigma_m$ and $\Delta\sigma$ are the conductivities of the particles, matrix and effective medium, respectively. When conductive particles are embedded in a

non-conducting matrix, $\Delta\sigma_m = 0$ and the equation 2.1.12 reduces to:

$$\Delta\sigma = \frac{s(K+1)^2 \varepsilon_m^2}{(\varepsilon_m(s+K) + \varepsilon_p(1-s))} \frac{\Delta\sigma_p}{\left(\varepsilon_m(s+K) + \varepsilon_p(1-s) + \frac{i\Delta\sigma_p}{\omega\varepsilon_0}(1-s)\right)} \quad (2.1.13)$$

Here we can see that the Maxwell-Garnett model is in fact a special case of the Bergman theorem with only one type of inclusions. The spectral function is therefore a delta-function:

$$G_{MG} = \delta\left(\frac{1-s}{K+1}\right) \quad (2.1.14)$$

Assuming again a Drude-like response of the carriers inside the inclusions, we obtain the effective mobility of charge carriers in the material by substituting 2.1.8 into 2.1.13 :

$$\mu_{eff} = \frac{s(K+1)^2 \varepsilon_m^2}{(\varepsilon_m(s+K) + \varepsilon_p(1-s))^2} \frac{q}{m} \frac{-i\omega}{\omega_0^2 - \omega^2 - \frac{i\omega}{\tau}} \quad (2.1.15)$$

If the permittivity of the particles and that of the matrix do not depend on the probing frequency ω , the effective mobility is characterized by a spectrum of damped harmonic oscillator (see section 2.2.2) with the resonance frequency:

$$\omega_0 = \sqrt{\frac{1-s}{\varepsilon_m(s+K) + \varepsilon_p(1-s)}} \omega_p \quad (2.1.16)$$

where $\omega_p = \sqrt{\frac{Nq^2}{\varepsilon_0 m}}$ is the plasma frequency of the charge carriers inside the nanocrystals. The conductivity of diluted non-percolated conductive nanocrystals shows a harmonic oscillator-like response; the resonance frequency depends directly on the plasma frequency of the carrier gas in the nanocrystal (see an illustration in Fig. 2.4). It means that the spectral shape of the effective response changes substantially with the density of carriers, i.e. with the magnitude of the intrinsic conductivity. This result of effective medium theory was observed in Si [12] and TiO₂ [7] nanocrystals and it was also interpreted as a direct consequence of the charge separation on the edges of the nanocrystals caused by the applied electric field. This charge separation results in an attracting electrostatic force between the positive and negative charges and causes transverse plasma oscillations (see Fig. 2.3 for illustration). [12, 13] This interpretation has a very similar background to that of the Maxwell-Garnett model. However, the important difference between the two approaches is that the Maxwell-Garnett model accounts for the effects of the depolarization fields on an electron from all the inclusions, not just from the inclusion containing the electron.

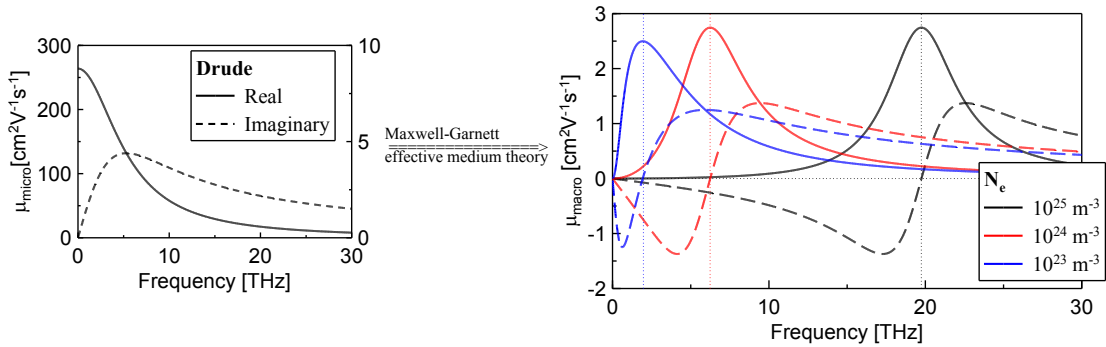


Figure 2.4: Illustration of the influence of the depolarization fields (within the Maxwell-Garnett effective medium theory) on the response of inclusions with Drude-like charge carrier mobility. With increasing carrier concentration the shape of the macroscopic carrier mobility substantially changes. The effective carrier mobility has an oscillator-like shape. The imaginary part of the mobility (dashed lines) becomes negative below the resonance frequency which depends on the carrier concentration inside the nanocrystals.

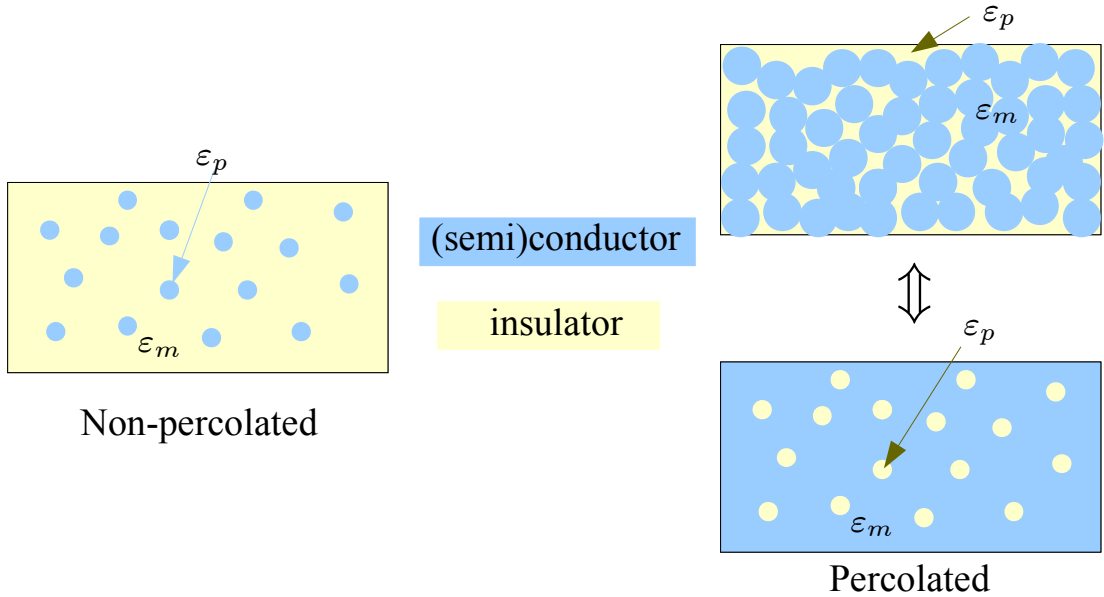


Figure 2.5: Illustration of the usage of the Maxwell-Garnett effective medium theory for nanocrystalline semiconductors. For non-percolated material (left panel), the nanocrystals are diluted in an isolating matrix. For percolated material (right panel), the nanocrystalline semiconductors form the matrix and the insulating voids are treated as particles.

“Inverted” Maxwell-Garnett model

The Maxwell-Garnett theory can be used also in strongly percolated systems, i.e. in samples where the nanocrystal particles touch each other. The percolated part can be then viewed as a conducting matrix ($\Delta\sigma_m \neq 0$) in Eq. 2.1.12 in which non-conducting voids (regarded as particles, $\Delta\sigma_p = 0$) are embedded. Additionally if $\varepsilon_p \ll \varepsilon_m$ (the nanocrystal has much higher permittivity than the nonconducting material), the equation 2.1.12 is reduced to: [6]

$$\Delta\sigma = \Delta\sigma_m \frac{K(1-s)}{K+s} \quad (2.1.17)$$

Consequently, the macroscopic mobility and the microscopic mobility of the matrix are proportional to each other:

$$\mu_{macro} = k_{EMA}\mu_{micro} \quad (2.1.18)$$

This effective medium theory was used to explain the electron transport in nanocrystalline ZnO [5] and nanocrystalline TiO₂ [14].

2.1.2 Bruggeman theory

In contrast with the Maxwell-Garnett model, the Bruggeman model treats the effective medium components symmetrically and it can be straightforwardly generalized for an arbitrary number of components. It assumes that if the structure is placed in a homogeneous electric field, the average electric field in the structure equals the electric field far from the sample. Thus the total contribution of the dipole moment of every inclusion to the far field is zero. Then the relation between the effective permittivity and the permittivity of the components consisting of spherical inclusions ($K = 2$) reads: [15]

$$\sum_i s_i \left(\frac{\varepsilon_i - \varepsilon_{eff}}{\varepsilon_i + 2\varepsilon_{eff}} \right) = 0 \quad (2.1.19)$$

For two-component systems the spectral function of the theory reads [16]:

$$G_{Brugg}(L) = \frac{3s-1}{2s} \delta(L) \Theta(3s-1) + \frac{3}{4\pi s L} \sqrt{(L-L^-)(L^+-L)} \Theta(L^+-L) \quad (2.1.20)$$

where Θ is the Heaviside step function and:

$$L^{+/-} = \frac{1}{3} \left(1 + s \pm 2\sqrt{2s - 2s^2} \right) \quad (2.1.21)$$

It can be immediately seen that the model predicts a percolated structure when $s > 1/3$. This effective medium theory together with the Drude model was used to model the response of nanocrystalline CdSe. [17]

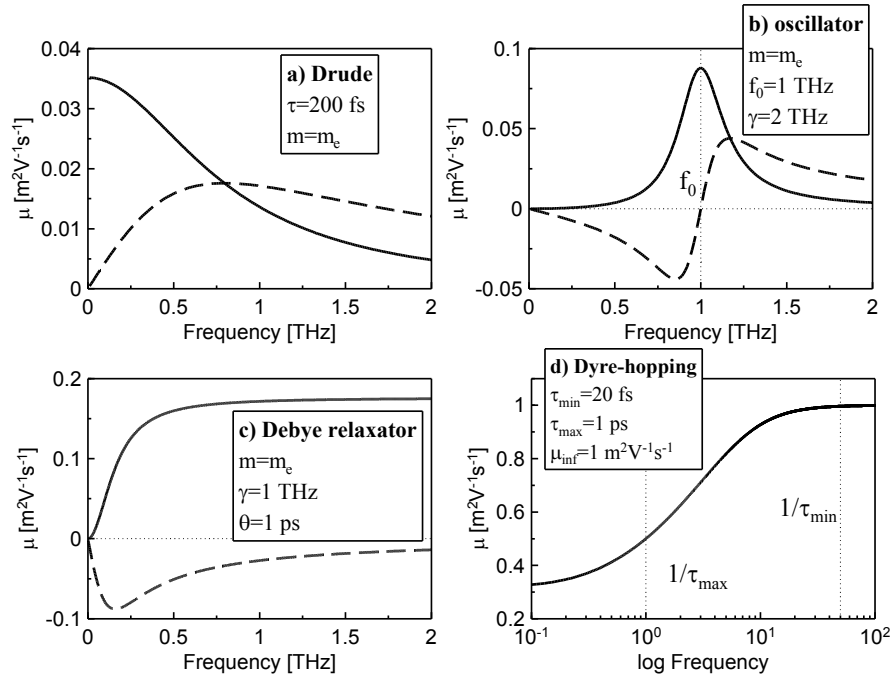


Figure 2.6: Spectrum of charge carrier mobility for several models of transport. The solid lines present the real part and the dashed lines show the imaginary part of the mobility

2.2 Models of conductivity spectra

In this section the most often used phenomenological charge carrier transport models will be introduced and summarized. In addition a Monte Carlo simulation based on classical equations of motion is presented, which was developed in our group. [5] This approach is able to model the charge carrier motion in more complicated structures than those assumed in the common phenomenological models.

2.2.1 Drude model

The Drude model is the most simple and widely used model of the conductivity. It describes the motion of free (conduction band) charge carriers in a bulk material. In this model the carriers do not experience any potential and their velocity changes randomly upon scattering on impurities, phonons etc. All the scattering events are elastic and isotropic with an average time interval τ . The scattering introduces a frictional force which is proportional to the velocity of the charge carriers:

$$\frac{d}{dt}\mathbf{p}(\mathbf{t}) = q\mathbf{E}(\mathbf{t}) - \frac{\mathbf{p}(\mathbf{t})}{\tau} \quad (2.2.1)$$

where $\mathbf{p}(\mathbf{t})$ is the momentum of a particle, $\mathbf{E}(\mathbf{t})$ is the local electric field and q is the charge. This equation yields the following spectrum of the charge mobility:

$$\mu(\omega) = \frac{q\tau}{m} \frac{1}{1 - i\omega\tau} \quad (2.2.2)$$

where m is the carrier effective mass. The complex mobility spectra of free charge carriers are characterized by decreasing real part with increasing frequency and a positive imaginary part, which displays a maximum at $\omega = 1/\tau$ (see Fig. 2.6 a). This behaviour is characteristic for an inductive response and describes charge carriers without any confinement. It is in striking contrast with the carrier response in systems where the charge carriers are confined. There the real part of the mobility increases with increasing frequency and the imaginary part is negative (capacitive response).

Despite this contrast between the Drude-like response and the response of localized carriers, the Drude model was successfully used for nanocrystalline systems in combination with effective medium theory (see section 2.1.1), for example, for nanocrystalline silicon [12] and TiO_2 [7].

2.2.2 Oscillator model

Long-range transport of charge carriers is suppressed if a restoring force exists driving them back into an equilibrium position. This is the situation for example for excitons and for charge carriers trapped at defect levels. In this case the equation of motion for a carrier reads:

$$m \frac{d^2x}{dt^2} + m\gamma \frac{dx}{dt} + m\omega_0^2 x = qE(t) \quad (2.2.3)$$

where x is the displacement of the carrier, γ the damping coefficient and ω_0 the resonant frequency. By solving the equation we obtain the complex mobility of carriers:

$$\mu(\omega) = \frac{q}{m} \frac{-i\omega}{\omega_0^2 - \omega^2 - i\gamma\omega} \quad (2.2.4)$$

Below the resonance frequency, the real part of the mobility is increasing from zero and it reaches its maximum at ω_0 ; the imaginary part is negative below ω_0 (see Fig. 2.6 b). Above ω_0 the conductivity qualitatively resembles that of the Drude model - the real part is decreasing with frequency and the imaginary part is positive. It follows that the particle experiences localization only at frequencies below ω_0 . The oscillator model has been used for the modeling of bound and free excitons in semiconductors, for example in bulk ZnO [18] and in GaAs quantum wells [19].

2.2.3 Debye model

For an overdamped oscillator ($\omega_0 \ll \gamma$) the behaviour (spectrum) of the mobility tends to the Debye model with a relaxation time $\theta = \gamma/\omega_0^2$:

$$\mu(\omega) = \frac{q}{m\gamma} \frac{i\omega\theta}{i\omega\theta - 1} \quad (2.2.5)$$

The real part of the mobility increases with frequency and the imaginary part of the mobility is negative (see Fig. 2.6 c). Therefore, the Debye model describes a localized response. However, this model can be used for low frequencies only; at high frequencies ($\omega \rightarrow \infty$) the real part of the mobility does not vanish, i.e. the model does not fulfill the sum rule.

The Debye relaxator model was found to be useful for describing the conductivity due to diffusive motion in a one-dimensional system of charge carriers with energy barriers (e.g. a polymer molecule). It was proven analytically [20], that if the energy barriers are perfectly reflecting, i.e. infinitely high, the mobility of such carriers is equal to a sum of relaxators with different relaxation times:

$$\mu(\omega) = 8D \frac{q}{k_B T} \sum_{k=0}^{\infty} \frac{c_k^{-2}}{\frac{D}{iL^2\omega} c_k^2 + 1} \quad (2.2.6)$$

where $c_k = 2\pi(k + 1/2)$, D is the diffusion constant in the system without the barriers, L is the distance between the barriers and T is the temperature of the system. The first term dominates. It has been shown that the sum of two relaxation terms is sufficient to characterize diffusive motion on 1D chains even with energy barriers of finite height. [21]

2.2.4 Hopping

The transport of charge carriers is possible not only by band conduction but also by hopping between localized states. There is a large number of models which describe the conductivity due to hopping motion. For example, the Dyre random free-energy model has been successfully used to describe electron hopping in microcrystalline silicon. [22] The model is based on the assumption that charge carriers can jump randomly over energy barriers with frequency between $1/\tau_{max}$ and $1/\tau_{min}$ [23]:

$$\mu(\omega) = i\omega\mu_{\infty} \left(1 - \frac{\ln(\tau_{min}/\tau_{max})}{\ln[(1 - i\omega\tau_{min}) / (1 - i\omega\tau_{max})]} \right) \frac{\ln(\tau_{max}/\tau_{min})}{1/\tau_{min} - 1/\tau_{max}} \quad (2.2.7)$$

The model predicts an increase of the real part of conductivity between frequencies $1/\tau_{max}$ and $1/\tau_{min}$ (see Fig. 2.6 d). These two frequencies delimit the range of conductivity dispersion within the model.

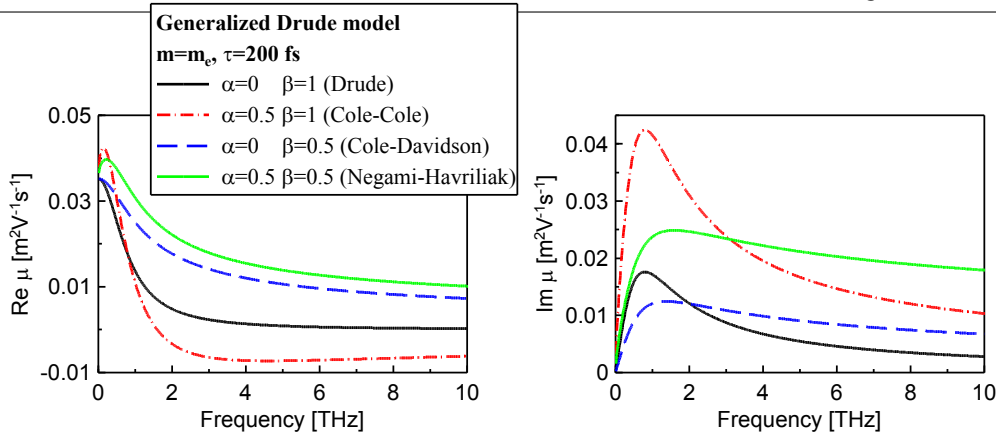


Figure 2.7: Shape of conductivity spectra described by the generalized Drude model for several parameters of α and β . The left panel shows the real part, the right panel displays the imaginary part of the carrier mobility.

2.2.5 Generalized Drude models

The Drude model is based on an assumption that the scattering in the system of carriers can be characterized by a single scattering time τ . However, sometimes it may not be valid – for example due to multiple-scattering mechanisms, non-elastic scattering, or non-equilibrium carrier distribution (for photoexcited systems). These complicated systems are modelled phenomenologically by introducing a parametrized distribution of scattering times. The most widely used models are the Cole-Cole and Cole-Davidson model. The combination of these two models gives a generalized Drude-model for the carrier mobility: [24]

$$\mu(\omega) = \frac{q\tau}{m} \frac{1}{(1 - (i\omega\tau)^{1-\alpha})^\beta} \quad (2.2.8)$$

where $0 \leq \alpha < 1$ accounts for the correction used in the Cole-Cole model and the exponent $0 \leq \beta < 1$ is used in the Cole-Davidson model (see Fig. 2.7 for the shape of the mobility spectra). [24] The real part of the mobility in the Cole-Cole model is negative for some frequency range (see Fig. 2.7). Nevertheless, these models were used for the characterization of the conductivity in doped silicon [25], GaAs [24] and ZnO [26].

2.2.6 Drude-Smith model

The Drude-Smith model [1] is a modification of the Drude model accounting for non-elastic and non-isotropic scattering of charge carriers. In the following reasoning we calculate the electric current induced by an electric delta-pulse. The Fourier transform of this time-dependent current (which equals to the response function) gives the conductivity of the system of carriers. The carriers experience scattering with an average time interval τ between scattering events as in the

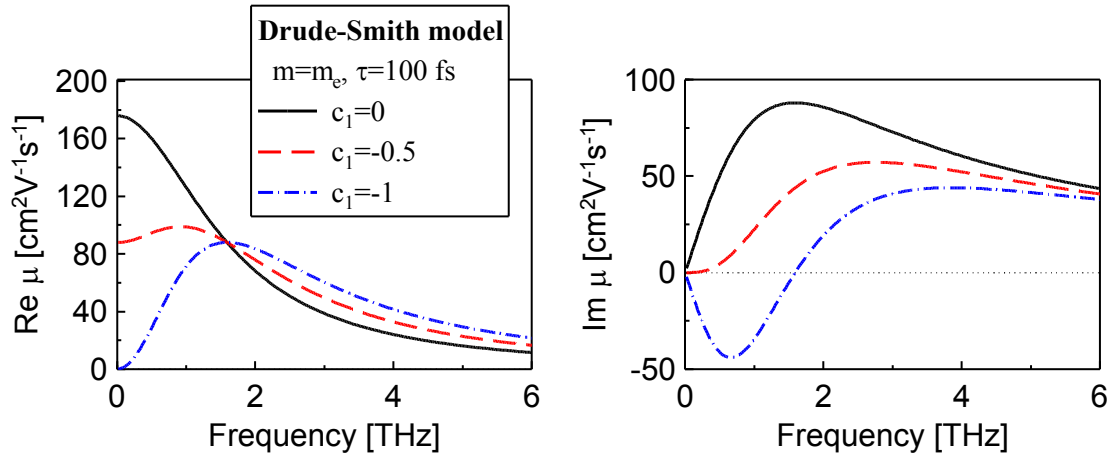


Figure 2.8: Illustration of the first-order Drude-Smith model for several parameters of backscattering (c). The left panel shows the real part, the right panel displays the imaginary part of the carrier mobility. For an increasing probability of backscattering the real part of the mobility is suppressed and the imaginary part becomes negative at low frequencies. This behaviour is typical for localized charge carriers.

Drude model. Therefore the density of occurrence of scattering events follows the Poisson distribution. The probability of n scattering events in a time interval $(0, t)$ then reads:

$$p_n(0, t) = \frac{1}{n!} \left(\frac{t}{\tau}\right)^n \exp\left(-\frac{t}{\tau}\right) \quad (2.2.9)$$

With every scattering event the carrier's contribution to the total electric current is reduced by a factor c_n for the n -th collision. Then the electric current reads:

$$j(t) = j(0) \exp\left(-\frac{t}{\tau}\right) \left[1 + \sum_{n=1}^{\infty} \frac{c_n}{n!} \left(\frac{t}{\tau}\right)^n\right] \quad (2.2.10)$$

In the Drude model due to the isotropic character of the scattering the carrier ceases to participate in the drift current already after the first collision event ($c_n = 0$ for $n \geq 1$). Therefore the zero-order contribution corresponds to the Drude current:

$$j(0) = \frac{Nq^2}{m} \quad (2.2.11)$$

The coefficient c_n has the meaning of the average value of the product $r_n \cos \varphi_n$ over an ensemble of collisions. Here φ_n is an angle between the direction of the original velocity (before the first collision) and after n collisions (see Fig. 2.9) and r denotes the relative change of the velocity magnitude with respect to the original velocity. If φ_n is smaller than $\pi/2$, c_n is in the interval $(0, 1)$. If φ_n is greater than $\pi/2$, c_n lies in the interval $(-1, 0)$ and the collision of the charge carriers occurs

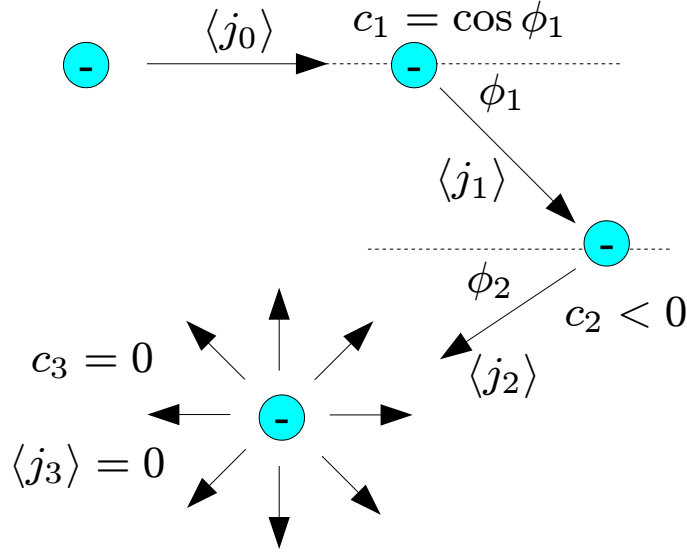


Figure 2.9: Illustration of the Drude-Smith model. The first scattering is elastic, therefore its contribution scales down by a factor equal to the cosine of the scattering angle. The second scattering event sends the particle to a direction opposite with the original direction, c_2 is then negative. The third scattering is isotropic, therefore the carrier does not contribute to the total current after the scattering event and $c_3 = 0$.

mainly in the backward direction with respect to the original velocity vector (for example the reflection of a carrier from nanocrystal boundaries). By applying Fourier transformation to equation 2.2.10 and substituting 2.2.11 one obtains for the average carrier mobility:

$$\mu_{DS}(\omega) = \frac{q\tau}{m} \frac{1}{1 - i\omega\tau} \left[1 + \sum_{n=1}^{\infty} \frac{c_n}{(1 - i\omega\tau)^n} \right] \quad (2.2.12)$$

Smith suggested that $c_n = 0$ for $n > 1$, i.e. only the first scattering event occurs into a preferred direction. Then the carrier mobility reads:

$$\mu_{DS}(\omega) = \frac{q\tau}{m} \frac{1}{1 - i\omega\tau} \left[1 + \frac{c_1}{1 - i\omega\tau} \right] \quad (2.2.13)$$

The influence of the parameter c_1 can be seen in Fig. 2.8. If c_1 is negative, the backscattering of charges decreases the current and leads to the suppression of the real part of the low-frequency mobility. The imaginary part of the low-frequency mobility decreases, too, and for $c_1 < -0.5$ it becomes negative. Therefore, for $c_1 < -0.5$ the Drude-Smith model can describe the localized response.

The Drude-Smith model has been successfully used to fit the conductivity spectra in various systems, for example poor metals [1], polymers [27], metallic thin films [28] and semiconductor nanostructures [29–33]. However, this model

has a serious shortcoming: it does not respect the homogeneity in time. [12] Indeed, if c_1 is the only nonzero coefficient, the first carrier collision is anisotropic with a preferential scattering direction: thus it is different from the other isotropic scattering events. This involves an unphysical ordering of the collisions. The only case when the reasoning above can be physically correct is when the collisions are identical and independent and therefore $c_n = c_1^n$. In this case the sum in the equation 2.2.12 can be carried out directly:

$$\mu_{DS}(\omega) = \frac{q\tau}{m} \frac{1}{1 - i\omega\tau} \left[1 + \sum_{n=1}^{\infty} \frac{c_1^n}{(1 - i\omega\tau)^n} \right] = \frac{q\tau}{m} \frac{1}{1 - i\omega\tau} \frac{1}{1 - \frac{c_1}{1 - i\omega\tau}} = \frac{q\tau_c}{m} \frac{1}{1 - i\omega\tau_c} \quad (2.2.14)$$

With identical collisions we get again a Drude-like carrier mobility with a reduced scattering time $\tau_c = \tau / (1 - c)$. [1]

2.2.7 Monte-Carlo simulations of charge transport in semiconductor nanocrystals

All the above mentioned models of charge transport can provide a phenomenological description of the microscopic conductivity in various systems. However, phenomenological coefficients obtained by fitting the experimental data often do not provide a deeper insight into the underlying microscopic processes. A quantitative microscopic model of charge transport in nanocrystalline semiconductors is required. Such a model should account for the following additional aspects of charge carrier motion:

- Charge carriers may interact with the boundaries. In this case, the Drude model cannot be considered as a correct description of the microscopic conductivity. The interaction with the boundaries can cause carrier scattering in a preferential direction (for example reflection from nanocrystal boundaries), which has to be accounted for.
- Transport of carriers among nanocrystals may occur. The probability of these transitions can influence the long-range conductivity substantially.

To address these problems, application of Monte-Carlo simulations was proposed by our group [5, 6, 34]. Within this approach, the motion of charge carriers inside nanocrystals is simulated as a free motion in the conduction band of a bulk semiconductor. Such motion is interrupted by scattering events either in the bulk (due to phonons, impurities etc.) or on the grain (nanocrystal) boundaries. Band-like motion of charge carriers is possible in nanoscopic systems, if the characteristic size of the confining nanoobjects is larger than the charge carrier Bohr radius in the material (weak localization). [35] This constitutes a limit of application of these simulations.

It is assumed that, upon interaction with nanocrystal boundaries, a carrier is either reflected back (backscattered) into the same nanocrystal (into a random direction within the half-sphere in the backward direction) or scattered into a completely random direction or transmitted to another nanocrystal without feeling the nanocrystal boundary at all. The interaction of charge carriers with nanocrystal boundaries is then entirely described by the probability values of these events. We can use two kinds of parameter sets for the quantitative representation of the interaction between the carriers and the grain boundaries:

- As an input into the simulation procedure we use the probability of backscattering p_r (carrier reflection into the same nanocrystal), scattering p_s (into random direction) and tunnelling p_t (the carrier does not change its velocity vector upon the interaction).
- For an intuitive picture about the carrier motion it is also appropriate to introduce the probability that, upon interaction with the grain boundaries, a carrier stays in the same nanocrystal p_B or transmits into another nanocrystal p_F .

There is a trivial connection between the two sets, because in case of the isotropic scattering on a grain boundary there is 50% probability that the carrier stays in the same nanocrystal. Therefore the connection is described by the equations:

$$p_B = p_r + \frac{1}{2}p_s \quad \text{and} \quad p_F = p_t + \frac{1}{2}p_s \quad (2.2.15)$$

It is also evident that the two parameter sets are not equivalent, because one pair of (p_B, p_F) may correspond to several triads of (p_r, p_s, p_t) . For example, $(p_B, p_F) = (0.8, 0.2)$ corresponds both to $(p_r, p_s, p_t) = (0.8, 0, 0.2)$ and to $(0.7, 0.2, 0.1)$. If the scattering time in the bulk semiconductor τ is smaller than the time of round-trip of a carrier inside a nanocrystal (i.e. $\tau \lesssim 2d/v$, where d is the nanocrystal size and v is the carrier velocity), the simulated spectra for these different sets are identical in shape and very similar in amplitude. The small difference in amplitude originates from the slightly different number of scattering events (for example, in a simulation with $(p_r, p_s, p_t) = (0.8, 0, 0.2)$ carriers are in average less often scattered than with $(0.7, 0.2, 0.1)$).

Upon every bulk scattering event the velocity of the carrier changes to a random direction. After every scattering event the absolute value of the velocity is chosen randomly within the Maxwell-Boltzmann or Fermi-Dirac distribution. The Maxwell-Boltzmann distribution is used for a system of carriers, where the Fermi-level is deeply below the conduction band edge – typically for $E_F < -k_B T$. In this case the mobility spectra are independent of the carrier density. However, for high carrier concentrations or low temperatures the Maxwell-Boltzmann statistics is not sufficient for characterizing the energy distribution of the carriers. In this case, the Fermi-Dirac distribution must be utilized. The carrier mobility may

then strongly depend on the concentration of carriers, which is connected with the Fermi-level through the equation (it is assumed that the conduction band of the semiconductor is parabolic):

$$N = 2 \left(\frac{2\pi m k_B T}{h^2} \right)^{\frac{3}{2}} F_{\frac{1}{2}} \left(\frac{E_F}{k_B T} \right) \quad (2.2.16)$$

where T is the temperature of the system of carriers, h is the Planck-constant, k_B is the Boltzmann-constant and F is the Fermi-integral:

$$F_j(x) = \frac{1}{\Gamma(j+1)} \int_0^{\infty} \frac{t^j dt}{1 + \exp(t-x)} \quad (2.2.17)$$

For example, when the system of carriers becomes degenerated, i.e. $E_F \gg 4k_B T$, only carriers close to the Fermi-level participate in the carrier transport. If the Fermi-level (and the carrier concentration) further increases, the velocity of carriers (which equals the Fermi-velocity) becomes higher and the carriers interact more often with the nanocrystal boundaries. Consequently, the shape of carrier mobility spectra changes substantially with the carrier concentration.

From the simulation the autocorrelation function of the carrier velocity is calculated and the carrier mobility is obtained using the Kubo formula [36], which for the Maxwell-Boltzmann distribution reads:

$$\mu_{ij}(\omega) = \frac{e}{k_B T} \int_0^{\infty} \langle v_i(0) v_j(t) \rangle \exp(i\omega t) dt \quad (2.2.18)$$

and for the Fermi-Dirac distribution [37]:

$$\mu_{ij}(\omega) = \frac{e}{k_B T} \frac{F_{-\frac{1}{2}} \left(\frac{E_F}{k_B T} \right)}{F_{\frac{1}{2}} \left(\frac{E_F}{k_B T} \right)} \int_0^{\infty} \langle v_i(0) v_j(t) \rangle \exp(i\omega t) dt \quad (2.2.19)$$

The brackets denote the averaging carried out over a canonical ensemble with temperature T .

To demonstrate the main features of our model, electron motion is simulated in a system of spherical nanocrystals with well-defined diameter d . In this case the electron mobility is isotropic, therefore the mobility obtained from the Kubo relation becomes a scalar.

The most important parameters of the carrier motion are:

- nanocrystal diameter d
- probabilities of distinct electron interactions with nanocrystal boundaries (p_r, p_s, p_t)

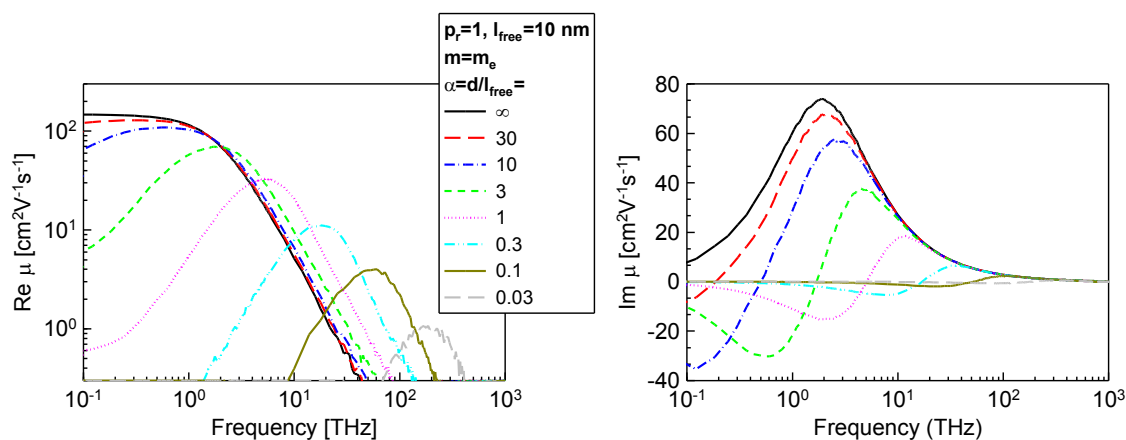


Figure 2.10: Carrier mobility in nanocrystalline systems with spherical nanocrystals calculated by Monte-Carlo simulations. The data are displayed for different ratios of nanocrystal diameter and mean free path. When the nanocrystal size is much larger than the mean free path, the carrier mobility follows the Drude model. If the nanocrystal size is comparable to or lower than the mean free path, the carriers interact often with the nanocrystal boundaries. Consequently, the real part of the mobility decreases at low frequencies and the imaginary part becomes negative. The image is taken from Ref. 5.

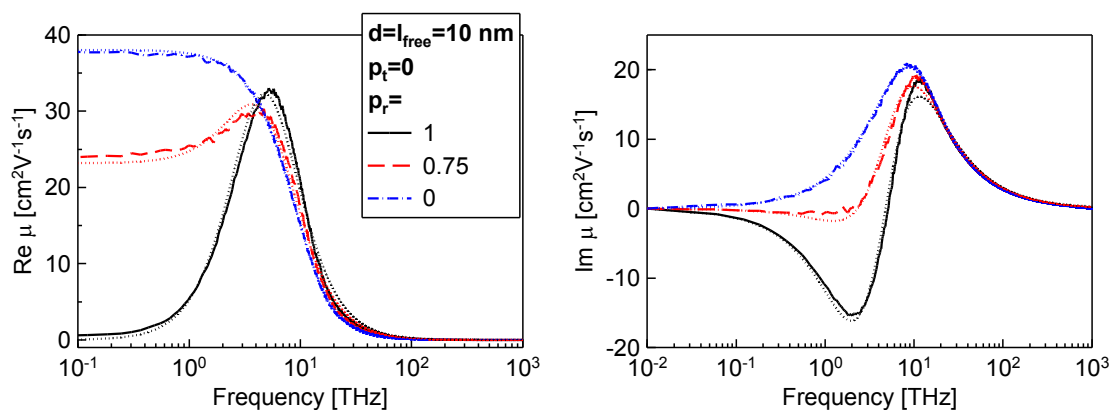


Figure 2.11: Carrier mobility in nanocrystalline systems with spherical nanocrystals calculated by Monte-Carlo simulations. The data are displayed for different probabilities of reflection on the grain boundaries. The dotted lines display the fit of the data by the Drude-Smith model. The image is taken from Ref. 5.

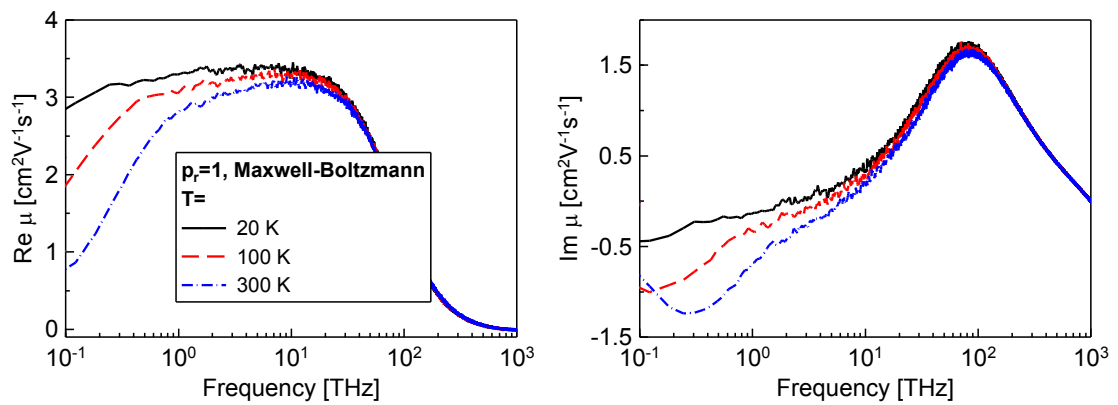


Figure 2.12: Carrier mobility in nanocrystalline systems with spherical nanocrystals calculated by Monte-Carlo simulations. The data are displayed for different temperatures and for low carrier densities (Boltzmann statistics).

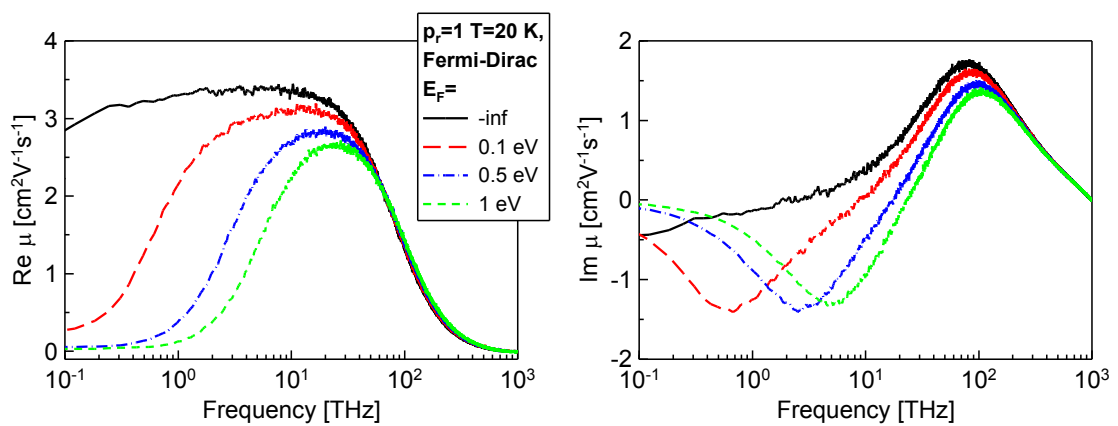


Figure 2.13: Carrier mobility in nanocrystalline systems with spherical nanocrystals calculated by Monte-Carlo simulations. The data are displayed for a degenerated system of carriers (Fermi-Dirac statistics) and for different Fermi-levels.

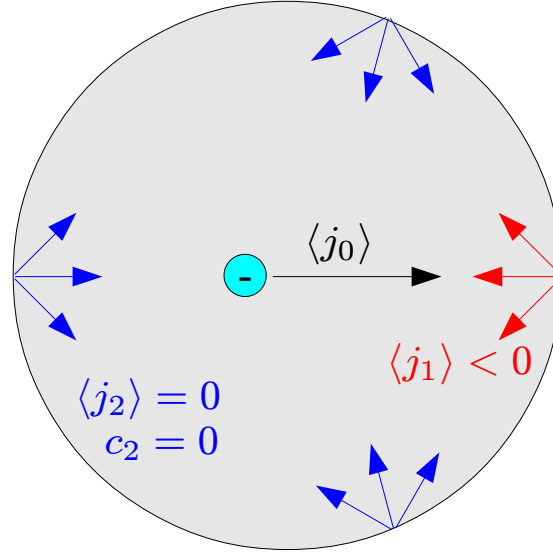


Figure 2.14: Comparison of the Monte-Carlo simulation of electron motion in a spherical nanocrystal and the Drude-Smith model. The first collision after the acceleration of the carriers by an electric delta-pulse involves a backscattering on the nanocrystal surface, therefore the direction of the averaged current after the collision is opposite to the direction of the current before the scattering event and $c_1 < 0$. The second collision can occur on the whole surface of the nanocrystal. Consequently, the average current after the second scattering event is zero and $c_2 = 0$.

- electron scattering time in the bulk τ or, equivalently, its mean free path l_{free}
- electron velocity (determined by the temperature T and the Fermi-level E_F)

In Fig. 2.10 the influence of the reflection probability and of the mean free path can be seen. If the nanocrystal size is large compared to l_{free} ($\alpha = d/l_{free} \gg 1$), the majority of the electron scattering events occur in the bulk and the interaction with the nanocrystal boundary is very rare. Consequently, the mobility of the carriers becomes Drude-like. This is also the case when the probability of reflection (p_r) at the nanocrystal boundary approaches zero (see Fig. 2.11).

With increasing carrier velocity the carriers interact more often with nanocrystal boundaries and therefore feel more localized. At low carrier densities the velocity is determined by the temperature T . With increasing temperature, the carrier mobility exhibits a higher degree of localization and the real part of the mobility decreases (see Fig. 2.12). At high carrier densities, when the Fermi-level is much higher than the thermal energy of carriers ($E_F \gg k_B T$), the carrier velocity is determined by the Fermi velocity ($v_F = \sqrt{2E_F/m}$). With increasing carrier density the Fermi velocity increases and therefore carriers exhibit a higher localization and the real part of their mobility decreases (see Fig. 2.13).

The simulated mobility can be fitted by the first-order Drude-Smith model (i.e. when only c_1 is nonzero). When $p_t = 0$, p_r is considerable and the size of the nanocrystal is smaller than the mean free path, $-c_1$ in the Drude-Smith model equals to the probability of reflection of carriers on the nanocrystal boundaries p_r . To explain the behaviour of the simulation spectra, let us follow the same reasoning as in the derivation of the Drude-Smith model. The carriers are placed in a spherical nanocrystal and accelerated by an electric delta-pulse. Let us examine the possibilities for the first scattering events. If the carrier scatters in the bulk, due to the isotropic nature of scattering the carrier ceases to contribute to the carrier transport. If the carrier reaches the nanocrystal boundary, a scattering event with preferential direction opposite to the original current j_0 occurs, therefore $\langle j_1 \rangle < 0$ and $c_1 < 0$. As the first (back)scattering event is equally probable in every direction back into the nanocrystal, the second one can occur on every point of the nanocrystal boundary. Consequently, the averaged current after the second collision $\langle j_2 \rangle$ becomes zero and $c_2 = 0$ (see Fig. 2.14).

It has been shown semi-empirically that fits by the Drude-Smith model in a limited spectral range give the parameters p_r and τ . A detailed discussion of the connection between the parameters of the simulation and the Drude-Smith model is presented in [5]. Although the simulated mobility spectra resemble those obtained from the Drude-Smith model, the simulation approach is superior to the Drude-Smith model due to the following reasons:

- The simulation parameters have a clear connection with the carrier motion, whereas the Drude-Smith model is purely phenomenological.
- Our model avoids any unphysical assumptions like ordering of collision events.
- The Monte Carlo simulation makes it possible to simulate the carrier mobility in any structure; the geometry of the structure is one of the input parameters of the simulation.

Chapter 3

Experimental methods and data analysis

The principal experimental method used in this thesis is THz time-domain spectroscopy, which provides the complex THz response (permittivity or conductivity) of a sample (photoexcited or in equilibrium). The following configurations need to be mentioned:

- The **transmission spectroscopy** is the most widely used method to characterize samples transparent in the THz frequency range. This method is used in this thesis to study thick pellets of nanocrystalline materials, therefore it is described more in detail in section 3.2.
- The **reflection spectroscopy** is applied to the characterization of materials which are not transparent in the THz frequency range. The dielectric function of the sample is calculated from its reflection function. [38]
- In **emission spectroscopy** the sample plays a role of the THz emitter. It is photoexcited by an ultrashort laser pulse and emits THz radiation. By measuring the time profile of the emitted THz pulse the carrier dynamics of the sample can be characterized. [39]
- In **optical pump–THz probe spectroscopy** the THz response of a sample, which is photoexcited by an ultrashort laser pulse, is measured. The method is used in this thesis to study the photoconductivity of nanocrystalline materials and it will be described more in detail in section 3.3.
- By an **imaging setup** the THz response of a sample is studied as a function of position on the sample's surface. By introducing near-field techniques the imaging of the THz response was enabled with spatial resolution of a fraction of the wavelength of THz radiation. [40, 41]

Optical pump–optical probe spectroscopy was used in this work as a complementary time-resolved technique to characterize the transient optical absorption of various materials. We describe this method in Section 3.4.

3.1 Basics of THz spectroscopy

Every THz setup used in this thesis is driven by ultrashort laser pulses. We use two kinds of laser sources:

- For steady-state THz spectroscopy we use laser pulses from a titan-sapphire oscillator with temporal length of ~ 80 fs, wavelength 810 nm, pulse energy 5 nJ and repetition rate 76 MHz. The power of these laser pulses is sufficient for generation and detection of THz pulses and the high repetition rate allows measurements with high sensitivity and high precision.
- For pump-probe experiments we use amplified laser pulses with temporal length of ~ 60 fs, wavelength 810 nm, pulse energy 1 mJ and repetition rate 1 kHz. This source enables not only generation and detection of THz pulses, but it also provides enough power for the photoexcitation of (and for inducing nonlinear phenomena in) a large variety of systems including semiconductors, liquids and gases.

In the next subsections we discuss the methods of THz generation and detection used in our experiments.

3.1.1 Generation of THz pulses

Photoconductive antennas

For steady-state THz spectroscopy we use a photoconductive antenna as the THz emitter. This is a well established method for generation of THz radiation using non-amplified laser pulses. The emitter consists of a semiconductor wafer with an applied bias voltage. Upon irradiation by the ultrashort laser pulses free charge carriers are generated in the semiconductor and accelerated by the applied electric bias. This results in an ultrashort current pulse. The decay time of the current is determined by carrier trapping which takes typically a few hundreds of femtoseconds. This current burst leads to an ultrafast change of the dipole moment and thus to the generation of a picosecond THz pulse (see Fig. 3.1 a). [43]

In our setup, we use an emitter with a specific interdigitated electrode structure. [42] The characteristics of the THz emission depend strongly on the geometry of the antenna. The structure of our emitter further increases the efficiency of the THz emitter. The electrodes on the semiconductor surface are prepared in a finger-like metal-semiconductor-metal structure (see Fig. 3.1 b), where the incident light is partially blocked to reach (and excite) the semiconductor only

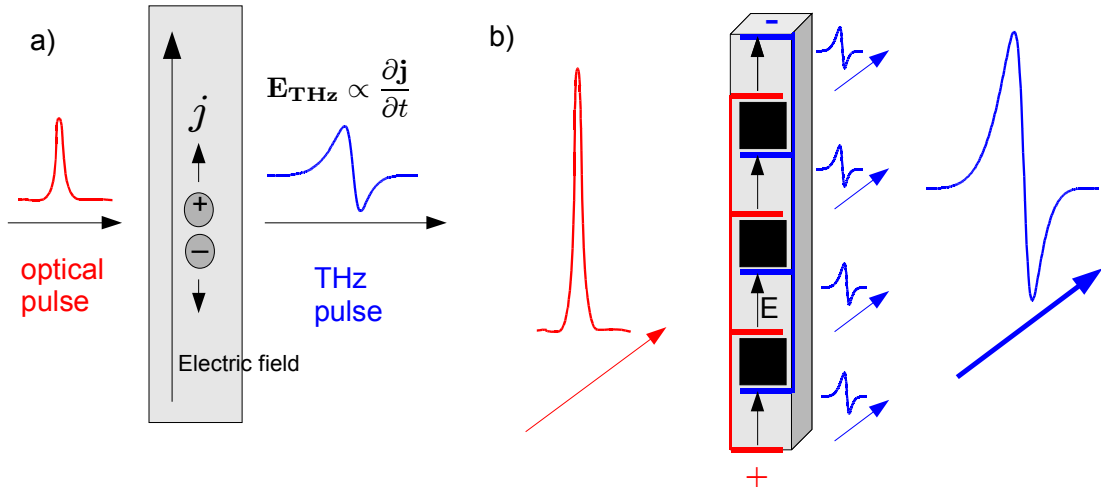


Figure 3.1: a) Principle of THz generation in a biased photoconductive antenna. The incident optical pulse generates free charge carriers in a semiconductor wafer, which are accelerated by externally applied bias. A short burst of current leads to the emission of a THz pulse. b) The electrodes are deposited on the semiconductor surface in a finger-like structure. Every second period of the structure is covered with a metal layer isolated from the electrodes (black), therefore the laser pulse irradiates only every second period. The emitter then consists of a series of small photoconductive antennas under strong bias. The constructive interference of the generated THz pulses leads to the emission of a THz pulse with strong electric field. [42]

at every second period. This is accomplished by a series of thin metallic layers deposited on the surface of the semiconductor and ensures that the bias on the irradiated part of the semiconductor has an identical polarity. This way, the structure consists of many small emitters with the emitted THz beams constructively interfering with each other in the far field (see Fig. 3.1 b). Consequently, the peak field of the THz pulse can reach several hundreds of V/cm. [42]

Optical rectification

For optical pump–THz probe experiments we use a THz emitter working on the principle of THz generation by optical rectification. Optical rectification is a three-wave mixing nonlinear optical effect. It leads to difference-frequency generation, i.e. the mixing of optical photons with frequencies ω_1 and ω_2 results in a photon with frequency $\Omega = |\omega_1 - \omega_2|$. When a femtosecond laser pulse propagates through the nonlinear medium, the mixing of spectral components of the laser pulse leads to an efficient generation of THz pulses. [44]

Our emitter consists of a (110)-oriented, 1 mm thick ZnTe crystal. We use ~ 0.3 mJ laser pulses to irradiate the ZnTe crystal and generate THz pulses

covering the frequency range 0.2 – 2.5 THz with 4 kV/cm peak electric field.

3.1.2 THz detection

The principle of the detection of THz pulses is based on the Pockels electrooptic effect. The Pockels effect is a three-wave nonlinear optical effect which involves a change in the refractive index of the nonlinear medium in response to an electric field. This change of the refractive index is linear with respect to the electric field and may be anisotropic. Consequently, during the presence of the electric field the polarization of the light transmitted through the nonlinear medium may be modified. In the electrooptic THz detection method, the THz pulse plays the role of the slowly varying electric field. Collinearly with the THz pulse an optical (sampling) pulse originating from the main laser source propagates through the nonlinear medium. The change of the polarization of the sampling pulse is monitored. As the optical pulse is typically much shorter than the THz pulse, the THz electric field is constant over the duration of the optical pulse. The polarization of the optical pulse is then affected only by the instantaneous electric field of the THz pulse. By varying the delay between the THz and optical pulses the time profile of the THz electric field can be measured.

The detection scheme used in our experiments is the following. As a sensor we use a 1 mm thick ZnTe electrooptic crystal. The crystal is oriented as shown in Fig. 3.2. The optical sampling beam has vertical polarization before reaching the ZnTe crystal. After passing through the sensor the optical beam transmits through a Babinet compensator and then it is divided into two linearly polarized beams by a Wollaston prism. The intensity of the two beams is measured by a pair of balanced photodiodes. Before starting the measurements (i.e. when the THz pulse is blocked before the sensor but the sampling beam is not), the Babinet compensator is set to a quarter waveplate position such that the difference between the intensities of the two beams at the output of the Wollaston prism (corresponding to the horizontally and vertically polarized part of the sampling beam) is zero. Consequently, any disruption of the balance of intensity between the two beams during the measurements is linearly proportional to the electric field of the THz pulse:

$$E_{THz} \propto |I_{\parallel} - I_{\perp}| \quad (3.1.1)$$

The temporal delay between the THz and sampling pulses is controlled by a delay line. By varying the delay between the optical gating pulse and the THz pulse the whole time profile of the THz pulse can be measured. A more detailed discussion of the method is presented in [45] and [46].

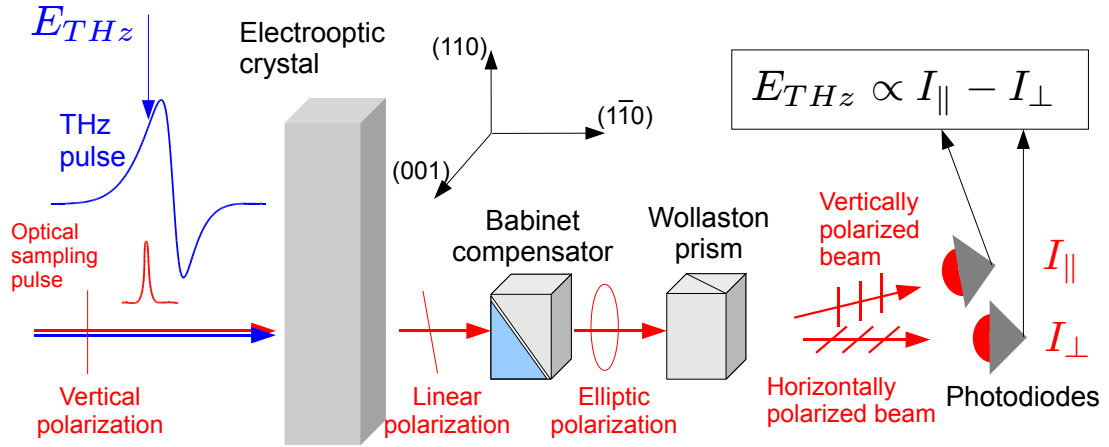


Figure 3.2: Principle of electrooptic THz detection. The THz pulse and a vertically polarized optical sampling pulse pass through an electrooptic crystal collinearly.

3.2 Steady-state THz spectroscopy

3.2.1 Experimental setup

The scheme of the experimental setup is displayed in Fig. 3.3. The optical laser beam is divided into two parts: a small part of the laser power is used for the electrooptic sampling (sampling branch), the other for the generation of THz radiation in the THz branch. The delay between the two pulses is controlled by a delay line. The THz branch consists of the emitter, the sample, the sensor and two ellipsoidal mirrors. The first mirror focuses the emitted beam on to the sample and the second one directs the THz beam transmitted through the sample to the detector. The sample may be placed in a cryostat allowing measurements at temperatures between 20 K and 300 K. In our setup it is also possible to study liquids in the form of jets [47] or in cuvettes. The whole THz branch is enclosed into a box which is evacuated or filled with an inert gas during the experiment. This eliminates the unwanted water vapor absorption of the THz wave, which is strong at several frequencies in the THz range.

The signal to noise ratio of the measurement is increased by utilizing synchronous detection using a lockin amplifier and by modulating the electric bias on the THz emitter. The lockin amplifier processes the input signal using Fourier transformation. Every component of the signal is filtered out, except for the one at the frequency equal to the modulation frequency of the signal.

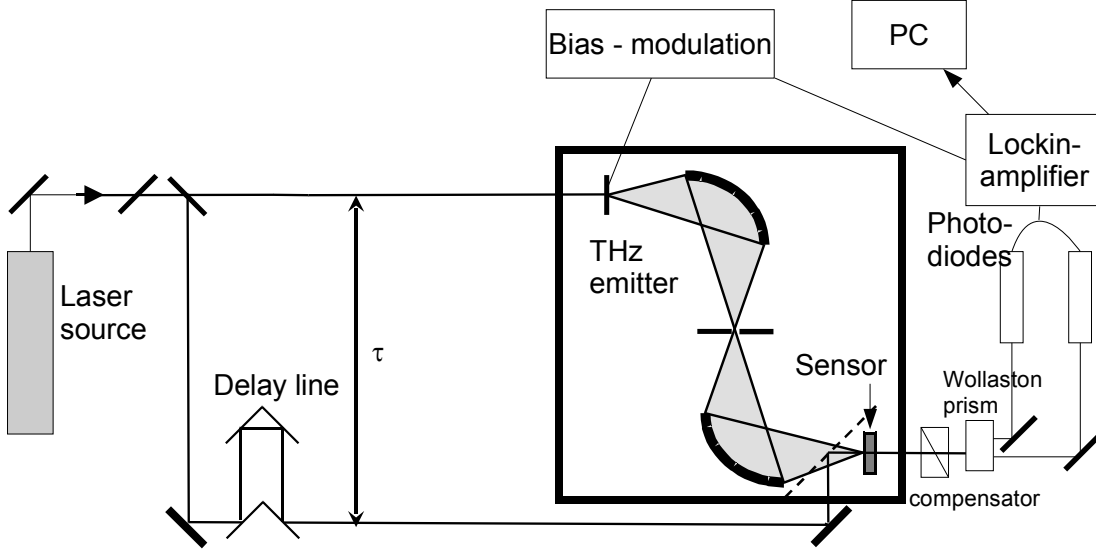


Figure 3.3: A common setup for THz transmission time-domain spectroscopy, used in our group.

3.2.2 Data analysis

When using the above described experimental setup, the measured time profile of the THz electromagnetic pulse (referred to as “THz waveform” in the following discussion) is influenced apart from the response of the sample also by the response of the emitter, sensor and the propagation between them. This can be expressed by the equation:

$$E_{meas}(t) = E_0 * P_{before} * t_{sample} * P_{after} * R_{sensor} \quad (3.2.1)$$

where E_{meas} is the measured signal, E_0 the generated THz waveform, P_{before} and P_{after} accounts for the propagation before and after the sample, R_{sensor} is the response function of the sensor and t is the complex transmittance of the sample. As the main aim is to measure the response of the sample, and the other response functions are generally not known, they must be eliminated by a reference measurement. In a reference measurement the THz wave is transmitted through a sample with known properties – often a vacuum slice of the same thickness as the original sample in a transmission setup obtained by removing the sample from the beam path. The measured reference waveform then reads:

$$E_{ref}(t) = E_0 * P_{before} * t_{vacuum} * P_{after} * R_{sensor} \quad (3.2.2)$$

By applying Fourier transformation to the equations 3.2.1 and 3.2.2 and calculating their ratio, all the instrumental functions are eliminated, and the complex transmission function can be evaluated:

$$T(f) = \frac{t_{sample}(f)}{t_{vacuum}(f)} = \frac{E_{meas}(f)}{E_{ref}(f)} \quad (3.2.3)$$

The fact that THz spectroscopy provides the time profile of the electric field of the signal, means that we are able to evaluate directly complex spectra: the complex transmission function and consequently the complex permittivity. The real and the imaginary part of the permittivity are extracted independently from the measurements, i.e. without the use of Kramers-Krönig relations. The retrieval of material properties (complex refractive index, conductivity or dielectric function) depends on the sample geometry.

Slab

In the simplest case the sample is a homogeneous plane-parallel slab irradiated by the THz wave under normal incidence (see Fig. 3.4 b). Approximating the THz radiation as a plane wave and assuming a non-magnetic sample, the transmission function reads:

$$T_{slab}(f) = \sum_{j=0}^{\infty} T_j(f) = \frac{4N}{(N+1)^2} \cdot \frac{\exp(2\pi i f d (N-1)/c)}{1 - \left(\frac{1-N}{1+N} \cdot \exp(2\pi i f d N/c)\right)^2} \quad (3.2.4)$$

where $N = n + i\kappa$ is the complex refractive index, d is the sample thickness, c is the velocity of light in vacuum. The radiation coming from internal reflections of various orders appear as a series of pulses separated in time by $2\bar{n}d$, where \bar{n} is the average real part of the THz refractive index of the sample. A temporal windowing can be applied to such a signal composed of well separated echoes (see Fig. 3.4). Each echo corresponds to a single term T_j and the complex refractive index can be retrieved from this part of the data. [48] For the contributions of the separate echoes to the transmission function we obtain:

$$T_j(f) = \frac{4N}{(N+1)^2} \exp(2\pi i f d (N-1)/c) \left(\frac{1-N}{1+N} \cdot \exp(2\pi i f d N/c) \right)^{2j} \quad (3.2.5)$$

This procedure is simpler than extracting the refractive index from the total transmission function T and it is also less sensitive to errors in the measurement. Moreover, by processing several echoes comparatively, the thickness d of the sample can be calculated together with the refractive index. [48, 49]

If the sample is optically thin, the refractive index must be evaluated from the equation 3.2.4. Both in case of optically thin or thick sample the equations have to be solved numerically. [50] Due to the periodicity of the exponential function with imaginary arguments, the equations have multiple solutions. If the selection of the correct solution is not obvious from a single measurement, it can be unambiguously found by doing measurements using two samples with different thicknesses [51] or by applying the Kramers-Krönig relations. [52]

Thin film

Another common sample configuration is a thin film deposited on a thick substrate (see Fig. 3.4 c). The sample then consists of two layers of different materials

and there are internal reflections in both of them. We assume that the film is optically thin, i.e. we cannot resolve the internal reflections in the film. On the other hand, the substrate is optically thick, which means that the transmitted THz wave is composed of pulses well separated in time, as in the case of optically thick slab. The time delay between the echoes is determined by the thickness of the substrate; note that the j -th echo (where $j = 0, 1, 2, \dots$) is composed of infinite number of components originating from internal reflections in the film. In the experiments discussed in this thesis we examine only the direct pass in the substrate ($j = 0$).

In order to obtain the (zero-order) complex transmittance of the sample, we need to calculate the complex transmittance of the film first. This problem is identical to the calculation of the transmittance of the Fabry-Pérot resonator, therefore we obtain:

$$t_f(f) = \frac{4N_f \exp(2\pi i f N_f d_f / c)}{(1 + N_f)(N_f + N_s) - (N_f - N_s)(N_f - 1) \exp(4\pi i f N_f d_f / c)} \quad (3.2.6)$$

where d_f is the thickness of the film and N_s, N_f is the complex refractive index of the substrate and the film, respectively. The zero-order echo involves only a direct pass through the substrate and transmission through the interface between the substrate and vacuum. Consequently, the zero-order complex transmittance of the sample (substrate+film) reads:

$$t_{FS}^{(0)}(f, N_f, d_f, N_s, d_s) = \frac{\frac{8N_f N_s}{1+N_s} \exp\left(2\pi i f \frac{N_f d_f + N_s d_s}{c}\right)}{(1 + N_f)(N_f + N_s) - (N_f - N_s)(N_f - 1) \exp(4\pi i f N_f d_f / c)} \quad (3.2.7)$$

where d_s is the thickness of the substrate. In the case of thin films the reference measurement typically involves the measurement of the THz waveform transmitted through a planparallel slab with properties identical to the substrate. Then the complex transmission function is obtained as the ratio of Eq. 3.2.7 and the zero-order complex transmittance of the substrate:

$$T^{(0)}(f, N_f, d_f, N_s, d_s) = \frac{4N_f N_s \exp\left(2\pi i f \frac{(N_f - 1)d_f}{c}\right)}{(1 + N_f)(N_f + N_s) - (N_f - N_s)(N_f - 1) \exp(4\pi i f N_f d_f / c)} \quad (3.2.8)$$

3.3 Optical pump–THz probe spectroscopy

Generally, in THz spectroscopy the probing pulses are generated by the interaction of ultrashort laser pulses with the emitter. The THz probing pulses are therefore perfectly synchronized with the pulse train from the laser source used for the THz generation. Consequently, it is possible to add an optical pump

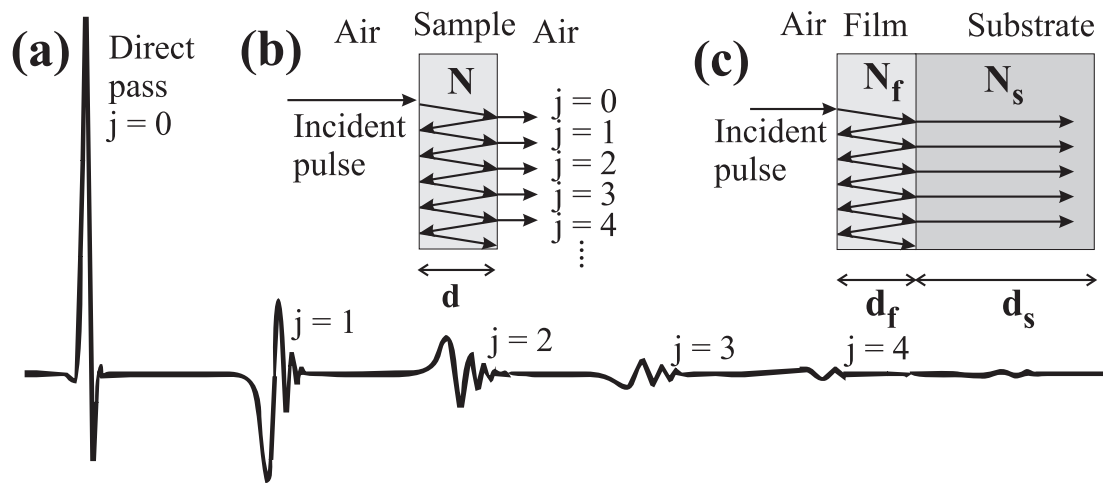


Figure 3.4: a,b) If the sample is optically thick, the internal reflections of the THz pulse can be separated in time. c) Internal reflections in a thin film on a substrate. Although we discuss the transmission of THz radiation through the sample under normal incidence, in the picture the internal reflections are shown under a different angle to make the illustration more perceivable.

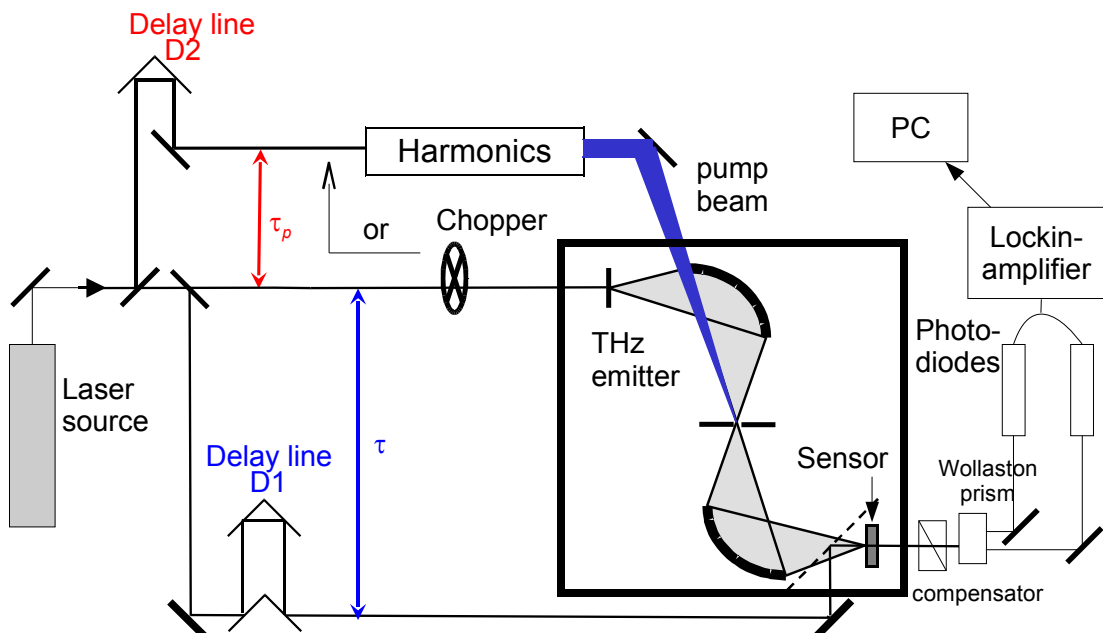


Figure 3.5: Experimental setup used for time-resolved THz spectroscopy.

branch to the measurement setup; a part of the power of the main laser source may be used to bring the sample out of equilibrium. The photoconductivity of the sample and its dynamics may be studied.

3.3.1 Experimental setup

Our setup used for time-resolved THz spectroscopy (see Fig. 3.5) is very similar to the one used for steady-state measurements, with the following differences:

- A multi-pass laser amplifier is used as the main laser source.
- ~ 0.3 mJ laser pulses are used to generation and detection of THz pulses. The remaining part is utilized for the photoexcitation of the sample. The pump-probe delay is controlled by a delay line.
- A nonlinear crystal (ZnTe) is used as THz emitter instead of the photoconductive antenna used in steady-state experiments.
- The modulation of signal for synchronous detection is accomplished by inserting an optical chopper into the beam path.

The pump beam irradiates the sample under an angle of ~ 10 degrees. Its wavelength can be changed using nonlinear optical elements. In our lab we use several arrangements to control the wavelength of the pump beam:

- The pump beam may be used without any modifications for photoexcitation on the basic wavelength 810 nm.
- By using second harmonic generation in a nonlinear crystal (beta-barium borate BBO or lithium triborate LBO) photoexcitation on 405 nm can be realized.
- By third harmonic generation using a pair of BBO nonlinear crystals an excitation beam with mean wavelength 270 nm can be obtained.
- The travelling-wave optical parametric amplifier of superfluorescence (TOPAS) used in our lab delivers wavelengths tunable in the range 300 – 1400 nm. However, due to its complexity and worse stability of its output, we prefer to use excitation by harmonic wavelengths wherever possible.

3.3.2 Data analysis

By the above described setup we measure the electric field profile of THz pulses transmitted through the sample. We can measure two kind of data:

- The profile of the THz pulse (waveform) transmitted through the sample $E(\tau, \tau_p)$ may be measured by modulating the THz signal (i.e. putting the optical chopper into the path of the optical beam which is used for THz generation).
- The difference in the transmitted signal induced by the optical excitation $\Delta E(\tau, \tau_p)$ can be directly measured, when the pump beam is modulated (i.e. the optical chopper is put in the path of the excitation beam).

Let us examine the transmission of the THz pulse in a material brought out of equilibrium by photoexcitation. The electric field of the optical excitation pulse changes the THz conductivity of the system via nonlinear phenomena. This nonlinear interaction involves mixing of the electric field of the optical pump pulse E_{opt} and that of the THz pulse E_{THz} and the nonlinear change in the conductivity is measured at THz frequencies. Consequently, this interaction must be caused by at least a third order nonlinear effect. For our discussion we consider only the third-order nonlinear polarization contributing to the transmitted THz radiation: [53]

$$\Delta P_{THz}^{(3)}(t) = \varepsilon_0 \int_0^\infty \int_0^\infty \int_0^\infty \tilde{\chi}^{(3)}(t', t'', t''') E_{opt}(t - t''') E_{opt}(t - t'') E_{THz}(t - t') dt' dt'' dt''' \quad (3.3.1)$$

where $\tilde{\chi}^{(3)}$ is the third-order susceptibility of the material, E_{THz} is the incident THz radiation and E_{opt} is the electric field of the photoexciting laser pulse. As the excitation pulse is much shorter than the THz radiation, we can approximate it as a delta-pulse with the time of incidence t_e :

$$E_{opt}(t) = \sqrt{I_{opt}} \delta(t - t_e) \quad (3.3.2)$$

After using this approximation in Eq. 3.3.1 and introducing the substitution $I_{opt} \tilde{\chi}^{(3)}(t, t', t') = \Delta \tilde{\chi}^{(3)}(t, t')$ we obtain:

$$\Delta P_{THz}^{(3)}(t, t - t_e) = \varepsilon_0 \int_{-\infty}^t E_{THz}(t') \Delta \tilde{\chi}^{(3)}(t - t', t - t_e) dt' \quad (3.3.3)$$

Up to now we considered the time of arrival of the excitation pulse t_e fixed. However, in our experiments this variable is not fixed. This is why we explicitly write the dependence of ΔP_{THz} on the second time variable $t - t_e$. The effective susceptibility $\Delta \tilde{\chi}^{(3)}(t_1, t_2)$ is the measure of influence of the THz pulse at time $t - t_1$ (i.e. at moment t_1 before the measurement) and of the excitation pulse at time $t - t_2$ on the "measured" nonlinear polarization. It is connected directly with the photoconductivity of the sample [54]:

$$\Delta \sigma(\omega, t_2) = \frac{\Delta \tilde{\chi}^{(3)}(\omega, t_2)}{i\omega \varepsilon_0} \quad (3.3.4)$$

where ω is the counterpart of the variable t in the Fourier space and $\Delta\sigma(\omega, t_2)$ is the photoconductivity of the sample at the moment t_2 after the photoexcitation of the material. The main aim of the measurements and the following data analysis is the complete retrieval of this function from the measured data.

Let the time of the arrival of the THz pulse be t_p . It is convenient to set this time as the time origin of the nonlinear polarization response. The nonlinear polarization then reads:

$$\Delta P_{THz}^{(3)}(t - t_p, t - t_e) = \varepsilon_0 \int_{-\infty}^{t-t_p} E_{THz}(t') \Delta\tilde{\chi}^{(3)}(t - t_p - t', t - t_e) dt' \quad (3.3.5)$$

Let us discuss the meaning of variables t, t_p, t_e in connection with optical pump–THz probe experiments. The variable t is connected with the time of measurement of the transient electric field, i.e. with the arrival of the sampling pulse. In our experiments we control the delay between the optical pump and THz probe pulses $\tau_p = t_p - t_e$ (using the delay line D2 – see Fig. 3.5). By delay line D1 we vary the time delay between the probe and sampling pulses $\tau = t - t_p$. The delay between the sampling and excitation pulse is $\tau_e = t - t_e$. By replacing the absolute times t_i by τ_i (variables controlled in the experiment) we obtain:

$$\Delta P_{THz}^{(3)}(\tau, \tau_e) = \varepsilon_0 \int_{-\infty}^{\tau} E_{THz}(t') \Delta\tilde{\chi}^{(3)}(\tau - t', \tau_e) dt' \quad (3.3.6)$$

This equation is already expressed using the variables which we control in our measurements. However, in our setup we measure directly the change of the transmitted THz field depending of the time delays τ and τ_p . The equation 3.3.6 has to be modified accordingly. This is accomplished by introducing the transformation between the time variables accounting for the probe-sampling and pump-sampling delays:

$$\Delta P_{THz}^{(3)}(\tau, \tau_e) \longrightarrow \Delta P_{THz}^{(meas)}(\tau, \tau_p = \tau_e - \tau) \quad (3.3.7)$$

and similarly for the nonlinear susceptibility:

$$\Delta\tilde{\chi}^{(3)}(\tau, \tau_e) \longrightarrow \Delta\tilde{\chi}^{(meas)}(\tau, \tau_p = \tau_e - \tau) \quad (3.3.8)$$

The nonlinear polarization expressed using the variables directly connected with the measurement then reads:

$$\Delta P_{THz}^{(meas)}(\tau, \tau_p) = \varepsilon_0 \int_{-\infty}^{\tau} E_{THz}(t') \Delta\tilde{\chi}^{(meas)}(\tau - t', \tau_p + t') dt' \quad (3.3.9)$$

The variable of integration t' is now present in both arguments of the effective nonlinear susceptibility. It is connected with the fact that a THz waveform transmitted through the sample measured by scanning τ and with fixed τ_p does not

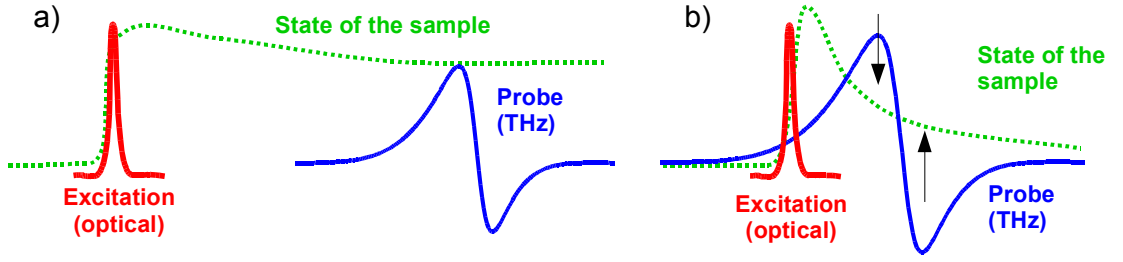


Figure 3.6: a) The state of the sample does not change on a time scale comparable with the temporal length of the probing THz pulse – steady-state analysis is sufficient. b) The state of the sample changes faster than the length of the probing pulse.

experience the same state of the sample (see Fig. 3.6 b). In other words, the THz pulse leading edge experiences a different response (nonlinear susceptibility) than its trailing edge. This complication in the experiment makes the extraction of the nonlinear susceptibility more difficult. In the general case, it is not possible to make the retrieval by means of a one-dimensional Fourier transformation as it was the case in steady-state experiments. [53, 55–57] The methods of data analysis are discussed in the next two subsections.

3.3.3 Quasi-steady state approximation

The above described analysis may be greatly simplified if the sample dynamics is slow and its state does not change on a time scale comparable with the temporal length of the THz pulse (see Fig. 3.6 a). Then the following approximation may be used:

$$\Delta\tilde{\chi}^{(meas)}(\tau - t', \tau_p + t') \approx \Delta\tilde{\chi}^{(meas)}(\tau - t', \tau_p) \quad (3.3.10)$$

And the equation 3.3.9 is reduced to a simple convolution:

$$\Delta P_{THz}^{(meas)}(\tau, \tau_p) = \varepsilon_0 \int_{-\infty}^{\tau} E_{THz}(t') \Delta\tilde{\chi}^{(meas)}(\tau - t', \tau_p) dt' \quad (3.3.11)$$

Let us define the response function of the photoexcited sample $T'(t, t') = T(t) + \Delta T(t, t')$. $T(t)$ is the response function of the sample in equilibrium, $\Delta T(t, t')$ represents the change induced by the pump beam. Within the steady-state approximation the transmitted waveform $E_T(\tau, \tau_p)$ can be described (similarly as in Eq. 3.3.11) by the equation:

$$E_T(\tau, \tau_p) = \int_{-\infty}^{\tau} E_{THz}(t') T'(\tau - t', \tau_p) dt' \quad (3.3.12)$$

where E_{THz} is the field incident on the sample. In our experiment the THz field induced by the photoexcitation is measured:

$$\Delta E(\tau, \tau_p) = \int_{-\infty}^{\tau} E_{THz}(t') \Delta T(\tau - t', \tau_p) dt' \quad (3.3.13)$$

This expression is a convolution of the incident THz wave and the response function of the sample. Therefore by applying Fourier transformation, the nonequilibrium response function in the frequency space, i.e. the transient transmission function can be evaluated:

$$\frac{\Delta T(\omega, \tau_p)}{T(\omega)} = \frac{\Delta E(\omega, \tau_p)}{E_{ref}(\omega)} \quad (3.3.14)$$

where E_{ref} is the reference waveform, which is measured with the sample without photoexcitation. The instrumental functions due to the propagation of the THz pulse and the response function of the detector are cancelled out identically as with measurements in steady-state THz spectroscopy (see on page 38).

From the transient transmission function the conductivity spectrum of the sample can be calculated based on the geometry of the sample. In this thesis the samples probed by time-resolved THz spectroscopy consist of a thin film deposited on an optically thick substrate. The complex transmittance for this sample geometry is calculated in section 3.2. We assume that only the film interacts with the photoexcitation pulse, the refractive index of the substrate does not change. Upon photoexcitation mobile charge carriers are generated in the film and the film's conductivity changes. The photoconductivity is $\Delta\sigma(\omega, \tau_p)$ at pump-probe delay τ_p . The refractive index then changes from its equilibrium value N_f according to the equation:

$$N_f^{(exc)}(\tau_p) = \sqrt{N_f^2 + \frac{i\Delta\sigma(\omega, \tau_p)}{\omega\epsilon_0}} \quad (3.3.15)$$

After the substitution of the formulas 3.2.7 and 3.3.15 into 3.3.14 we obtain an equation for the transient conductivity of the sample:

$$\frac{\Delta E(\omega, \tau_p)}{E_{ref}(\omega)} = 1 - \frac{t_f\left(\omega, \sqrt{N_f^2 + \frac{i\Delta\sigma(\omega, \tau_p)}{\omega\epsilon_0}}\right)}{t_f(\omega, N_f)} \quad (3.3.16)$$

where t_f is the complex transmittance of the film described by Eq. 3.2.6. Using equation 3.3.16, from a measured reference and a transient waveform at the pump-probe delay τ_p we obtain the photoconductivity $\Delta\sigma(\omega, \tau_p)$. In the quasi-steady state approximation, to reconstruct the complete dynamics of the photoconductivity (i.e. find the photoconductivity spectra for every τ_p) one should measure the transient THz spectra at a series of values of $\tau_{p,j}$ where the time difference

between the adjacent values of $\tau_{p,j}$ is about the temporal length of the THz pulse (i.e. $\tau_{p,j+1} - \tau_{p,j} \approx t_{THz}$). Fortunately, often a smaller number of measurements is sufficient.

We use the following procedure. We measure the dependence of the maximum of the transient THz waveform on the pump-probe delay $\Delta E(\tau_{max}, \tau_p)$, i.e. τ is fixed in the maximum of the waveform and the signal ΔE is recorded while the pump-probe delay is scanned through the range of interest. Subsequently, a series of transient THz spectra $\Delta E(\tau, \tau_{p,i})$ is measured in the same experimental conditions. The values of pump-probe delays $\tau_{p,i}$ are chosen such that the shape of the waveform $\Delta E(\tau, \tau_{p,i})$ does not change significantly between $\tau_{p,i}$ and $\tau_{p,i+1}$. By using a linear combination of the transient signals $\Delta E(\tau, \tau_{p,j})$ and $\Delta E(\tau, \tau_{p,j+1})$ with the weights defined by the measured $\Delta E(\tau_{max}, \tau_p)$, an approximation of the transient spectra $\Delta E(\tau, \tau_p)$ for each τ_p can be obtained, and hence the kinetics $\Delta\sigma(\omega, \tau_p)$ is calculated.

To examine the characteristics of carrier transport, one should calculate the carrier mobility by normalizing the transient conductivity according to the equation 2.0.3. However, the carrier concentration N is not directly accessible as the quantum yield of the excitation process is usually unknown. However, we can measure the incident pump pulse fluence and calculate the number of excitation events N_{phot} per laser pulse and per unit volume. Consequently, we normalize the transient conductivity by the density of photoexcitation N_{phot} instead of the carrier concentration. In this way we obtain the product of the carrier mobility and the quantum yield of the excitation:

$$\xi(\tau_p) \mu(\omega, \tau_p) = \frac{\sigma(\omega, \tau_p)}{N_{phot} e_0} \quad (3.3.17)$$

This quantity is experimentally accessible and gives a good picture of the carrier transport; namely if the measured kinetics at different conditions (excitation density etc.) are compared. One can often guess the quantum yield a posteriori by comparing the measured yield-mobility spectra with an appropriate model of the carrier transport.

3.3.4 Analysis of ultrafast dynamics

If the dynamics of the sample is ultrafast, i.e. its state significantly changes over a time range of ~ 1 ps, the approximation given by the equation 3.3.10 is not valid; the expression 3.3.9 cannot be replaced by a simple convolution. There are two basic existing approaches to connect the measured data with the underlying conductivity mechanisms in the sample:

- The propagation of the THz pulse may be simulated in the photoexcited medium using finite-difference time-domain simulations. [53] In this case a concrete model has to be assumed for the transient conductivity. By

comparing the simulated and measured data the parameters of the model can be determined. The main disadvantage of this approach is that for the analysis a specific analytic model has to be assumed.

- In the approximation of small signal, where $\Delta E \ll E$, the data analysis is carried out by applying 2D Fourier transformation to the measured transient THz data $\Delta E(\tau, \tau_p)$. As a result, the 2D Fourier transform of the response function $\sigma(\omega, \omega_p)$ is directly determined: [55] where ω is the counterpart of τ in the Fourier space and ω_p corresponds to τ_p

$$\frac{\Delta E(\omega, \omega_p)}{E_{ref}(\omega)} = \frac{\Delta \sigma(\omega, \omega_p) \Xi(\omega, \omega - \omega_p)}{i\omega \epsilon_0 T^{sam}(\omega)} \frac{E_0(\omega - \omega_p)}{E_0(\omega)} \quad (3.3.18)$$

where ω is the counterpart of τ in the Fourier space and ω_p corresponds to τ_p , $T^{sam}(\omega)$ is the transmission function of the sample in equilibrium and Ξ is the transfer function specific to the geometry of the sample. The transfer function Ξ for a variety of sample geometries were derived in Ref. 54. A demonstration of the retrieval procedure is provided in [56, 57]. The retrieval procedure was tested on well-known model systems [56, 57] and applied e. g. to the investigation of electron transport in microcrystalline silicon [22] and polymer acceptor blends. [21]

The characterization of a sample exhibiting ultrafast dynamics imposes increased demands on the experiment:

- The probing THz beam and the optical excitation beam must be collinear and perpendicular to the surface of the sample. If, for example, the excitation beam is incident on the sample under an angle ϕ , the excitation events on the sample surface occur within a time interval $d \cos \phi$ depending on the place of the sample (here d is the diameter of the excitation beam). The THz beam coming under normal incidence probes different parts of the sample with a different time delay. The time-dependent response of the sample is smeared and the time resolution of the experiment becomes limited.
- A dense 2D grid of the transient waveform $\Delta E(\tau_i, \tau_{p,j})$ has to be measured, which imposes high demands on the stability of the main laser source.
- In addition to a reference waveform, the time profile of the THz pulse incident on the sample $E_0(t)$ has to be determined. [57]

In the measurements performed in this thesis the dynamics of the studied samples is sufficiently characterized using the steady-state approach. Consequently, we do not use these advanced methods for the analysis of the measured data.

3.4 Optical pump–optical probe spectroscopy

In addition to optical pump–THz probe measurements, we performed time-resolved experiments at optical frequencies, i.e. optical pump–optical probe measurements. In these measurements the dynamics of the optical absorption of an optically excited sample is explored.

3.4.1 Experimental setup

The main laser source is identical to that used in time-resolved THz spectroscopic measurements. Both transmission and reflection setups were used. The output of the main laser source is divided into a pump and a probe branch. The wavelength of both the pump and probe beams can be changed using nonlinear crystals or an optical parametric amplifier:

- The probe beam is either used at its basic wavelength of 810 nm (i.e. without the use of any nonlinear optics) or its wavelength is changed by a parametric amplifier (accessible wavelengths 300 – 1400 nm).
- The photoexcitation of the sample can be realized at 810 nm (basic wavelength), 405 nm (using second-harmonic generation in a BBO crystal) or 270 nm (using the third harmonic generated in a pair of BBO crystals).

In the transmission setup, the probe beam irradiates the sample almost under normal incidence. In the reflection geometry the angle of incidence and the angle of reflection of the probe beam are close to zero. The pump-probe delay is controlled by a delay-line. As the output of the TOPAS parametric amplifier seeded by the multipass amplifier is noisy, we introduced several improvements into the setup to enhance the signal to noise ratio (see image 3.7):

- A synchronous detection method is used by modulating the pump or the probe beam by an optical chopper.
- A part of the probe beam is separated from the main beam path and measured by a photodiode. During the measurements, the measured reflection/transmission signal is normalized by the time-integrated signal from this diode. This way, the effect of slow power fluctuations of the main laser source on the measured data is eliminated.
- Another part of the probe beam is separated from the beam path and its arrival on the sample is advanced by several hundreds of picoseconds compared to the probe beam. This auxiliary beam interacts with the sample similarly to the probe beam (i.e. it passes the sample or it is reflected from the sample). Due to its negative time delay, the auxiliary optical pulse irradiates the sample always in its equilibrium state. Before starting any

measurement the pump beam is blocked and the intensity of the transmitted/reflected probe and auxiliary beams are measured by a pair of balanced photodiodes. The power of the auxiliary beam is tuned by a pair of gradient filters before reaching the photodiode to match that of the probe beam. This way, the effect of shot-to-shot power fluctuations (which have identical effect on the probe and auxiliary beams) on the signal is reduced.

3.4.2 Data analysis

To measure the dynamics of the reflectivity/transmittance of the sample, we perform two measurements:

- A reference measurement is performed by placing the chopper in the path of the probe beam. The intensity of the probe beam is influenced by all the optical elements in the setup, therefore the reference intensity takes the form:

$$I_{ref}(\lambda) = I_0(\lambda) T_{before}(\lambda) A(\lambda) T_{after}(\lambda) D(\lambda) \quad (3.4.1)$$

where $I_0(\lambda)$ is the intensity of the generated probe beam (after the laser source at 810 nm or after the parametric amplifier), $T_{before}(\lambda)$ the transmittance of the setup between the source and the sample, $A(\lambda)$ the reflectivity/transmittance of the sample, $T_{after}(\lambda)$ the transmittance of the setup between the sample and the detector, and $D(\lambda)$ accounts for the response of the detector.

- The optical chopper is placed in the path of the pump beam and the variation of the probe beam intensity induced by photoexcitation is measured. The measured signal again depends on the instrumental functions of the experimental setup and the change of the optical properties of the sample:

$$\Delta I(\lambda, \tau_p) = I_0(\lambda) T_{before}(\lambda) \Delta A(\lambda, \tau_p) T_{after}(\lambda) D(\lambda) \quad (3.4.2)$$

The ratio of the $\Delta I(\lambda, \tau_p)$ and $I_{ref}(\lambda)$ then yields the ratio of the transient transmittance/reflectivity and the transmittance/reflectivity in equilibrium $\Delta A(\lambda, \tau_p) / A(\lambda)$.

The dynamics of sample reflectivity/transmittance are measured only at selected wavelengths, therefore the Kramers-Krönig relations cannot be used to obtain both the real and imaginary parts of the refractive index. Often it is assumed that the change of only one of them occurs due to the photoexcitation or only one of them has the dominating effect on the change of the optical properties of the sample. Here we calculate the connection between the change of the reflectivity/transmittance and the change of the complex refractive index.

We assume that the probe beam irradiates the sample under normal incidence and the photoinduced change in the reflection/transmission is much lower than

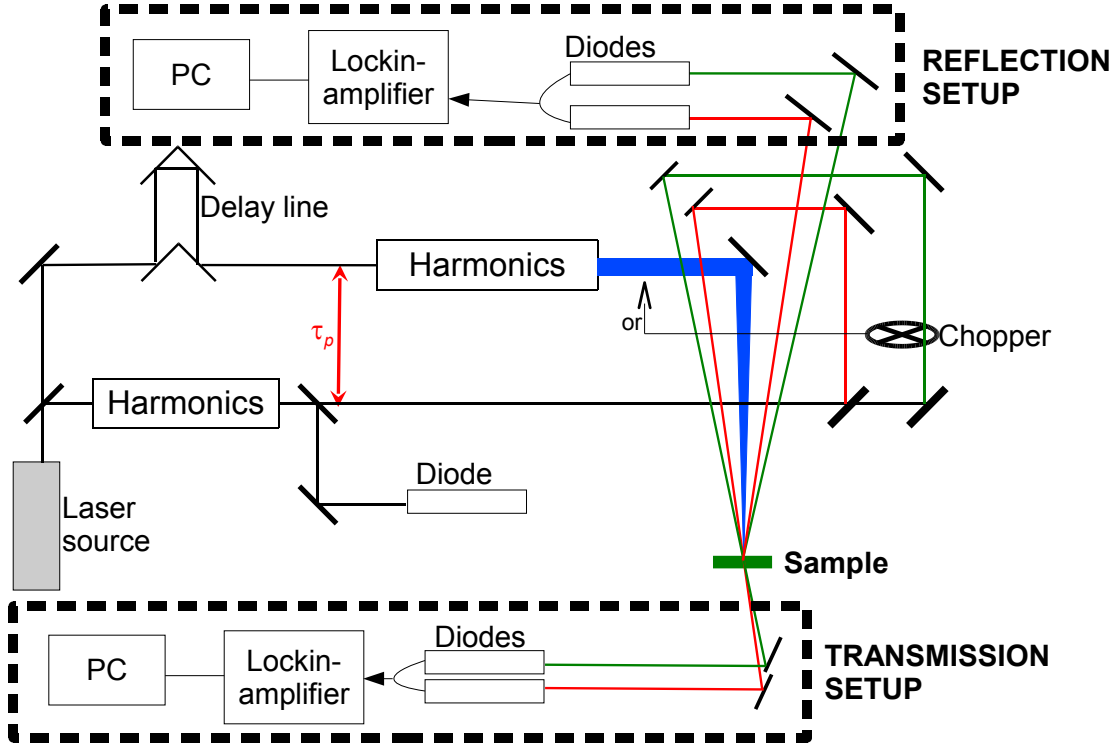


Figure 3.7: The optical pump–optical probe setup used in our lab. Both the transmission setup (box in the bottom) and the reflection arrangement (box on the top) is depicted. The probe beam is shown by the green line, the auxiliary by the red one and the pump beam is shown in blue.

the reflectance/transmittance of the sample in equilibrium. Therefore we obtain for the change of reflectance/transmittance induced by photoexcitation:

$$\Delta A = \frac{\partial A}{\partial n} \Delta n + \frac{\partial A}{\partial \kappa} \Delta \kappa \quad (3.4.3)$$

where n is the real part, κ is the imaginary part of the refractive index of the sample and Δn and $\Delta \kappa$ denotes the change in the refractive index induced by photoexcitation.

In the reflection geometry we use the Fresnel equation to calculate the reflectance of the sample:

$$R = \frac{(n - 1)^2 + \kappa^2}{(n + 1)^2 + \kappa^2} \quad (3.4.4)$$

By substituting the reflectance into the equation 3.4.3 we obtain:

$$\frac{\Delta R}{R} = \frac{4(n^2 - \kappa^2 - 1) \Delta n + 8n\kappa \Delta \kappa}{((n + 1)^2 + \kappa^2) ((n - 1)^2 + \kappa^2)} \quad (3.4.5)$$

In the transmission setup we assume that the sample is a planparallel slab and upon photoexcitation the change of the refractive index is homogeneous in the

whole sample. If the internal reflections in the sample can be neglected, the transmittance reads:

$$T = \frac{16n^2}{((n+1)^2 + \kappa^2)^2} e^{-2d\kappa} \quad (3.4.6)$$

By substituting the transmittance into the equation 3.4.3 we obtain:

$$\frac{\Delta T}{T} = \frac{2}{(n+1)^2 + \kappa^2} \left[\frac{\kappa^2 + 1 - n^2}{n} \Delta n + (2\kappa - d((n+1)^2 + \kappa^2)) \Delta \kappa \right] \quad (3.4.7)$$

Chapter 4

Electron transport in niobium-doped titania nanoparticles

Transparent conductive oxides (TCOs) have found to be useful in a number of optoelectronic devices including photovoltaics or flat panel displays. The standard material used as TCO in existing applications is tin-doped indium oxide (ITO). However, indium is rare and expensive, therefore there is an extensive research to find suitable replacements. [58] The possibility of preparing TCOs in a nanocrystalline form is of great interest, as it could significantly enhance the field of applications of these materials. [59] It has been shown that Nb-doped anatase titania (NTO) films may become a cheap alternative of ITO as they have high optical transmittance for the visible light and exhibit a dc conductivity as high as $10^3 - 10^4 \text{ S.cm}^{-1}$. [60] Moreover, the preparation of NTO in the form of nanoparticles and mesoporous films was recently demonstrated. [61] The conductivity of the prepared nanocrystalline NTO films was found by several orders smaller than that of an epitaxial film: at most 0.25 S.cm^{-1} . Characterization of the charge transport in this material by time-domain THz spectroscopy is useful for the optimization of the conductivity and understanding of charge transport mechanisms.

4.1 Sample preparation and properties

Nb-doped nanoparticles were prepared by our collaborators at the Department of Chemistry and Center for NanoScience, University of Munich. For their preparation titanium tetrachloride and niobium (V) ethoxide were dissolved in tert-butyl alcohol. The nanoparticles were grown at temperatures 60, 100 and 150 °C with Nb molar content of 0%, 10% and 20%. The nanoparticles were pressed under a pressure of 10 MPa in a sample holder with diameter 13 mm. The thickness of

the resulting pellets ranged from 0.55 to 1.28 mm. These samples were studied both as-prepared and after annealing at 600 °C in nitrogen atmosphere to prevent oxidation and water vapour absorption. [61]

It has been found that both the doping level and the growth temperature play an important role in the features of the nanoparticles. The particles obtained with the growth temperature of 60 °C are completely amorphous, those prepared at 100 °C are completely crystalline with a structure similar to anatase. Further increase of the growth temperature while keeping constant the growth duration leads to an increase of the particle size. Nb-doping has been found to suppress the crystallization of the nanoparticles and enhance their conductivity. The dc conductivity of pellets prepared from nanoparticles grown at temperature 100 °C is 1×10^{-6} S.cm⁻¹ for the undoped and 1×10^{-5} S.cm⁻¹ for the 20% doped particles. The annealing of the pellets increases their conductivity up to 0.25 S.cm⁻¹. [61]

To evaluate the role of the crystallinity of the particles in the mechanisms of charge transport we selected a set of samples grown at temperatures 60, 100 and 150 °C with Nb-doping level 20% (samples denoted as NTO_20%@60 °C, NTO_20%@100 °C and NTO_20%@150 °C). [14] To study the influence of the doping level a set of samples grown at 100 °C with doping levels 0%, 10% and 20% was chosen (samples NTO_0%@100 °C, NTO_10%@100 °C and NTO_20%@100 °C). We studied both as-prepared and annealed samples (we denote the annealed sample with N₂, i.e. NTO_20%@100 °C N₂ is NTO_20%@100 °C annealed in nitrogen atmosphere). The duration of growth of these samples was set such that the size of the nanoparticles was around 4 nm.

4.2 Measurement

We measured the ac permittivity of the samples in the THz frequency range using steady-state time-domain THz spectroscopy. Additionally, the permittivity at microwave frequencies (20 MHz – 10 GHz) was measured using an Agilent 85070E dielectric probe with an Agilent E8364B network analyzer by Martin Kempa in the Department of Dielectrics of the Institute of Physics. The measured permittivity data are displayed in Fig. 4.1. Although bulk anatase is dispersionless at frequencies below 1 THz [62], the values of the permittivity obtained by the two techniques do not correspond to each other – the permittivity measured at microwave frequencies is for the majority of measurements lower than that in the THz frequency range. Measurements at microwave frequencies were carried out using the coaxial dielectric probe attached to the sample. The accuracy of these measurements then depends on the quality of the electric contact between the probe and the sample. Our samples are rigid with a rough surface and the electric contact could not be made perfectly. Consequently, the permittivity spectra measured using the dielectric probe give a good insight into the trends

of the permittivity spectra at microwave frequencies but the absolute value of the permittivity can be erroneous. It follows that the microwave spectra cannot be used for a common fitting with the spectra measured using time-domain THz spectroscopy.

4.3 Model of the effective permittivity

The permittivity of bulk anatase is dominated by phonon modes; all of the phonon frequencies lie above 7 THz. [62] The observed decrease of the permittivity with increasing frequency in the microwave frequency range therefore cannot be explained solely by the response of bulk anatase. The microwave permittivity exhibits a relaxation-like response. We attribute this response to the hopping of charge carriers. [63] The model of intrinsic permittivity that we use to describe the response of our samples therefore consists of two parts:

- **Permittivity of anatase.** This model is based on the measurement of the permittivity of anatase in Ref. 62. As bulk anatase is anisotropic, we approximate its permittivity by the average of the diagonal elements of the permittivity tensor. The permittivity is then calculated as $\varepsilon_{\text{anatase}} = (2\varepsilon_a/3) + (\varepsilon_c/3)$, where ε_c is the component describing the response along the tetragonal c -axis, ε_a the component in the plane perpendicular to c . The average permittivity spectra of bulk anatase are displayed in Fig. 4.2. In nanocrystalline anatase one can expect enhanced dielectric losses (i.e. increased $\text{Im } \varepsilon$) in comparison with bulk anatase due to extrinsic losses, which are caused by the presence of lattice defects. The behaviour of these low-frequency extrinsic losses is often similar to the intrinsic ones caused by multiphonon effects: one usually observes a linear increase with the frequency, $\text{Im } \varepsilon \propto \omega$. [64] Consequently, we represent the increased imaginary part of the permittivity by a single loss enhancement factor Q , by which we multiply the imaginary permittivity of bulk anatase. This factor may be different for samples with different preparation parameters (growth temperature, doping etc.).
- **Carrier hopping conductivity.** We describe the carrier hopping in the pellets by the Dyre random free energy model presented in subsection 2.2.4 by the equation 2.2.7. The parameters of this model are the hopping times $\tau_{\text{min}}, \tau_{\text{max}}$ and the saturated conductivity σ_∞ , which depends on the density of mobile carriers and is therefore different for each sample. We fix the hopping times to the same value for every sample; $\tau_{\text{min}} = 20$ fs, which corresponds to the phonon frequency [63]. We assume that electron hopping occurs in the whole frequency range of our measurements, therefore fix τ_{max} to the value of 100 ns corresponding to a hopping frequency below the microwave range.

Our model of microscopic permittivity therefore reads:

$$\varepsilon_{micro} = \text{Re } \varepsilon_{anatase} + Q \text{Im } \varepsilon_{anatase} + \frac{i\sigma_{hopping}}{2\pi f \varepsilon_0} \quad (4.3.1)$$

4.4 Effective medium theory

Although all the samples are made of the same materials with similar fabrication process and the mass densities of all the pellets are comparable to each other, the observed permittivity values in the THz range are quite different when comparing different samples. For example, $\varepsilon \approx 7$ is measured for NTO_0%@100 °C and $\varepsilon \approx 28$ for the annealed NTO_20%@150 °C N₂. These large differences must then originate from a different degree of percolation of the conductive anatase grains in the samples. We attempt to describe the relation between the microscopic and the effective permittivity using a parametrized Bergman spectral function, which is able to account for media with different percolation strengths. It is assumed that the composite consists of a percolated component and a non-percolated one characterized by a single value of depolarization factor L_A . Then the Bergman spectral function consists of two δ -functions:

$$G(L) = C_{perc} \delta(L) + C_{nonp} \delta(L - L_A) \quad (4.4.1)$$

where the δ -function around zero represents the percolated component with a weight C_{perc} and the δ -function at L_A stands for the non-percolated component with a weight C_{nonp} . By using the normalization conditions for an isotropic sample (equations 2.1.5 and 2.1.6) we obtain two additional relations between the parameters of the model:

$$C_{perc} + C_{nonp} = 1 \quad \text{and} \quad L_A = \frac{1 - s}{3C_{nonp}} \quad (4.4.2)$$

After substituting these relations into 4.4.1 we obtain:

$$G(L) = C_{perc} \delta(L) + (1 - C_{perc}) \delta\left(L - \frac{1 - s}{3(1 - C_{perc})}\right) \quad (4.4.3)$$

The effective permittivity ε_{eff} is obtained by substituting the equation 4.4.3 into the basic formula of the Bergman theory 2.1.3. The relation between the microscopic and effective permittivity then reads:

$$\varepsilon_{eff} = 1 + sC_{perc} (\varepsilon_{micro} - 1) + s \frac{1 - C_{perc}}{\frac{1}{\varepsilon_{micro} - 1} + \frac{1 - s}{3(1 - C_{perc})}} \quad (4.4.4)$$

The titania nanoparticles are assumed to form closely packed spheres, therefore their volume fraction is set to $s = 0.65$.

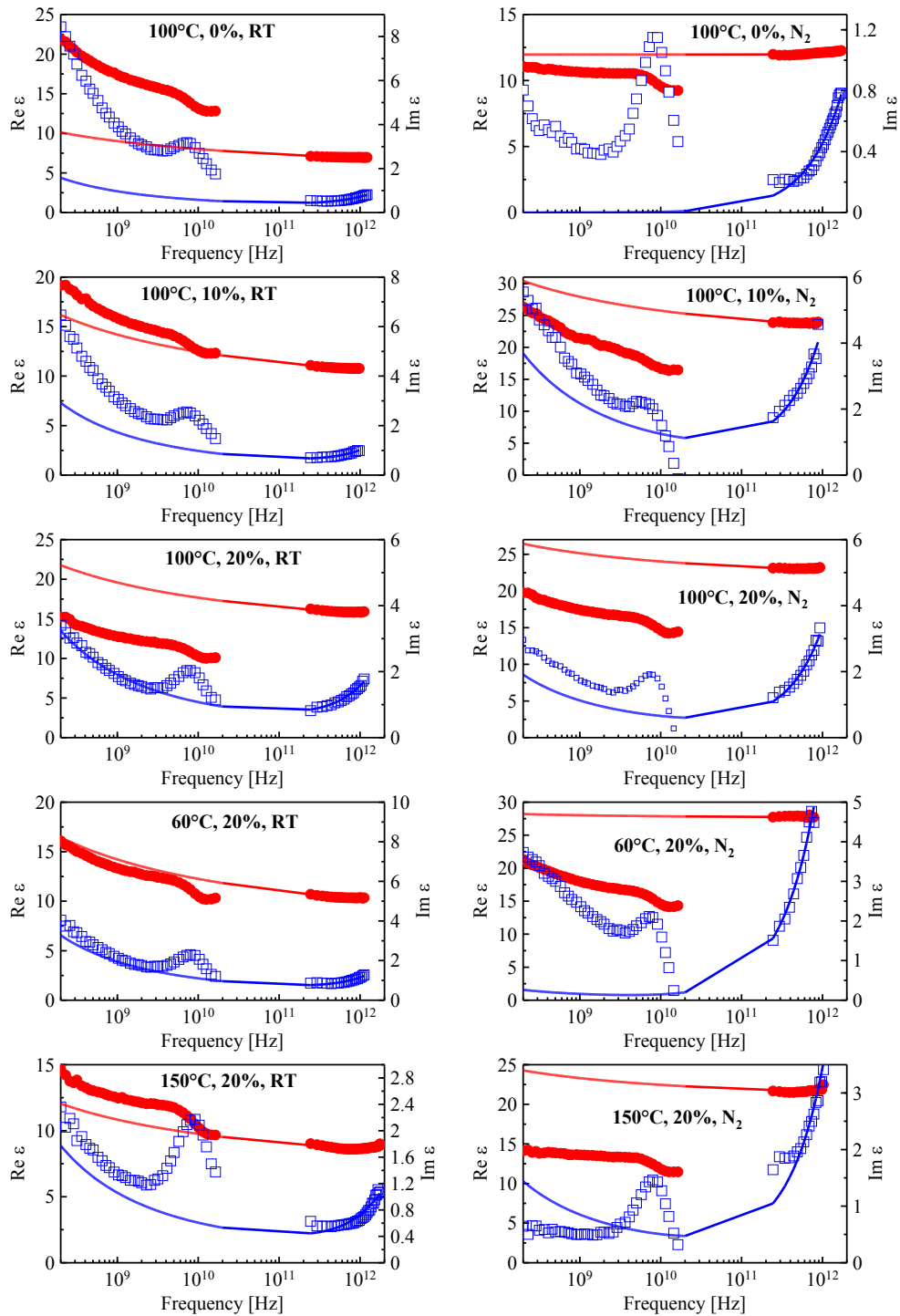


Figure 4.1: Measured permittivity spectra of the NTO pellets both in the microwave and THz frequency range. The symbols represent the measured data (\bullet the real part, \square the imaginary part of the permittivity), the solid lines the fit of the THz spectra extrapolated to microwave frequencies.

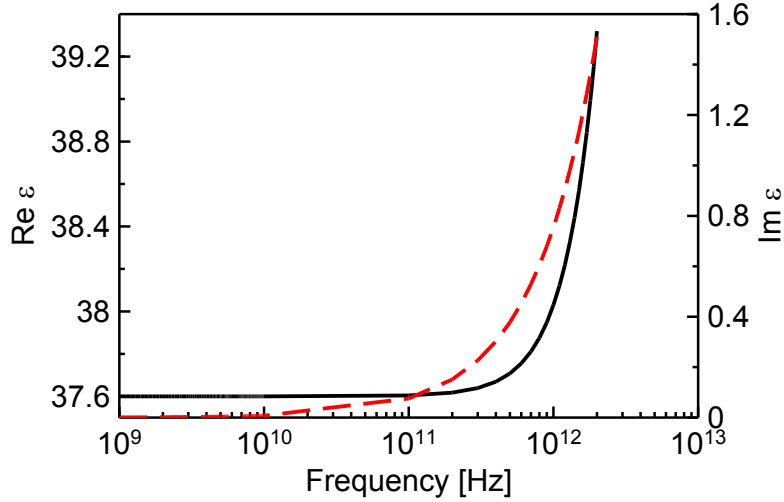


Figure 4.2: Average permittivity spectra of bulk anatase calculated based on Ref. 62. The solid black line shows the real part, the dashed red line displays the imaginary part of the permittivity.

Obviously, the above described model may be valid only if the depolarization factor of the non-percolated component is lower than unity, i.e. $L_A \leq 1$. If the parameters obtained by the fitting procedure do not fulfill this condition, C_{perc} is close to unity and we may assume that the sample is percolated. In this case we use the inverted Maxwell-Garnett model described in subsection 2.1.1 as an appropriate effective medium approximation. The relation between the intrinsic permittivity of NTO and the effective permittivity is then obtained by substituting $\varepsilon_m = \varepsilon_{micro}$, $\varepsilon_p = 1$, $K = 2$ into and replacing s by $1 - s$ in the equation 2.1.11:

$$\varepsilon_{eff} = \varepsilon_{micro} \frac{3 - 2s + 2s \varepsilon_{micro}}{s + (3 - s) \varepsilon_{micro}} \quad (4.4.5)$$

When using this model the volume fraction of the particles s is not fixed; it is among the fitting parameters of the model.

A study of the permittivity of niobium doped titania nanoparticles based on the same measured data as in this section is published in Ref. 65. The effective medium theory used in that publication is different from the model developed in this work. In Ref. 65 the material is considered as consisting of percolated and nonpercolated parts and the effective permittivity is expressed as a linear combination of the two components:

- The permittivity of the percolated component equals the permittivity of anatase nanoparticles ε_{micro} .
- The permittivity of the nonpercolated part is obtained from the Maxwell-Garnett model assuming tightly packed anatase nanoparticles.

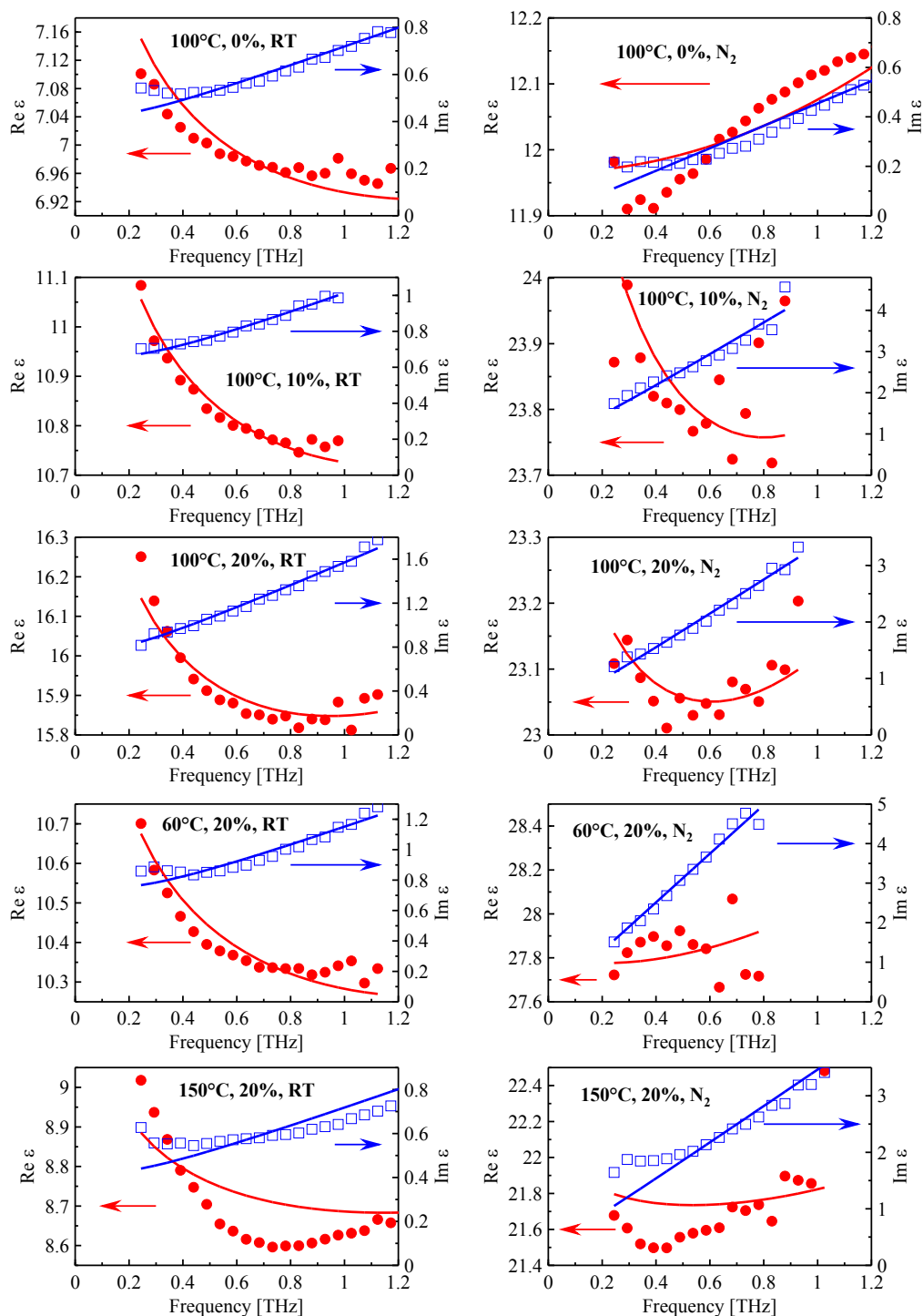


Figure 4.3: Measured THz permittivity spectra of the NTO pellets. The symbols represent the measured data (\bullet the real part, \square the imaginary part of the permittivity), the solid lines the fit of the spectra

It follows that the volume fraction of the nonpercolated part in the material tunes both its NTO content and its degree of percolation. In contrast, our current model has one parameter corresponding to the degree of percolation C_{perc} and an independent parameter s corresponding to the NTO content. That is why we consider the model of effective medium presented in this section more correct than that shown in Ref. 65.

4.5 Results

The carrier hopping model together with the simplified Bergman model fits well the THz spectra of the as-prepared and undoped samples. For the annealed samples, with the exception of the undoped one, the value of C_{perc} (i.e. the weight of the percolated part in the Bergman model) is close to unity; in this case one finds $L_A > 1$ and, consequently, the parametrized Bergman model cannot be applied to describe the permittivity spectra. For these samples we use the inverted Maxwell-Garnett theory described by the equation 4.4.5. The high degree of percolation of nanoparticles is described by setting $C_{perc} = 1$ in Fig. 4.4. From the fitting procedure we have found that the volume fraction of the nanoparticles in the percolated pellets is very close to 0.65, i.e. the same as the volume fraction assumed for the as-prepared samples. This justifies our choice of treating the pellets as closely packed spheres in the parametrized Bergman model. For the as-prepared or undoped samples a significant part of the material is non-percolated. The weight of the percolated part C_{perc} in the pellets increases upon annealing of the sample. This indicates sintering of the nanocrystals or further crystallization and growth of the grains. The parameter C_{perc} increases also with doping for both annealed and as-prepared samples. Nb doping therefore has a positive effect on nanoparticle sintering.

The dielectric losses have to be enhanced in all samples in order to successfully model the permittivity spectra. (see Fig. 4.4). The coefficient of enhancement Q is the highest (~ 11) for the undoped as-prepared sample and it drops to 2.7 upon annealing. It may be due to the improved crystallinity of the annealed anatase grains. The loss enhancement factor for the doped sample is in the range 5–9 and it increases with annealing. This suggests that introducing of Nb atoms leads to lattice deformation in the grains, therefore to higher extrinsic losses. The character of defects then probably changes upon annealing leading to a higher phonon decay at low frequencies.

In Fig. 4.1 the fitting model extrapolated to microwave frequencies is compared with the permittivity spectra measured at the microwave and THz frequency range. Although in most cases the absolute values of the measured and calculated permittivities do not correspond to each other, the trends in the dielectric spectra are similar. The reason of the discrepancy lies in the above explained systematic error in the measurements with the dielectric probe and also in the

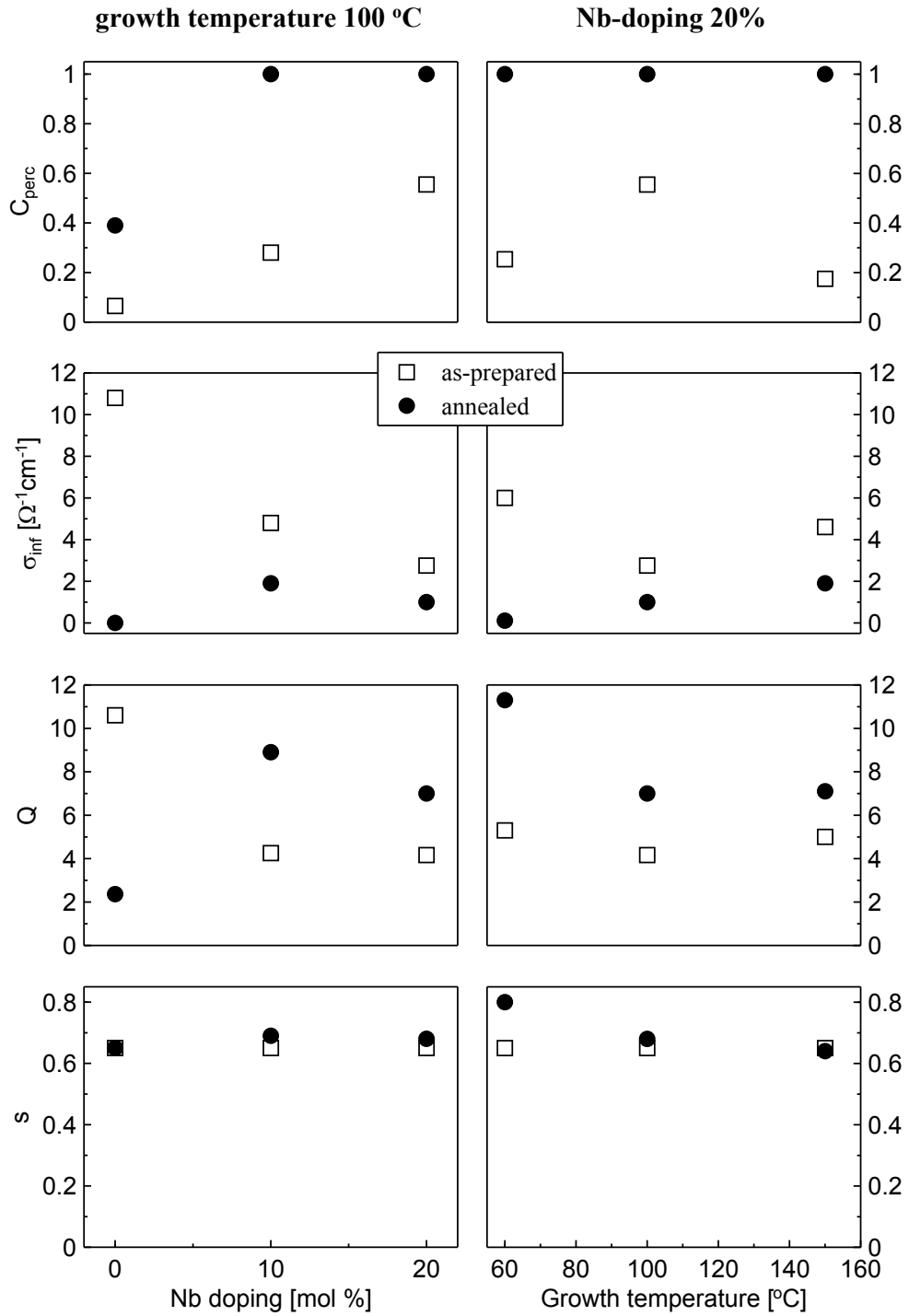


Figure 4.4: Results of fits of the THz permittivity for the pellets pressed from nanoparticles with varying doping levels synthesized at 100 °C (left column), and nanoparticles with 20% doping level synthesized at several temperatures (right column). (\square) As-prepared samples, (\bullet) annealed samples.

fact that the carrier hopping was obtained entirely from the measured relatively narrow-band THz spectra. Dyre's model assumes carrier hopping over energy barriers in a system where the energy barriers are in the range $(\Delta E_{min}, \Delta E_{max})$, and their distribution is uniform. [23] However, electromagnetic radiation at microwave and THz frequencies induce carrier hopping over a different set of barriers due to the large difference between the two frequency ranges. Consequently, it is possible that the parameters of the hopping model extracted from the THz spectra can not be applied without a small modification to model simultaneously the microwave spectra.

The saturated hopping conductivity σ_{∞} decreases significantly with annealing and it vanishes for the annealed undoped sample. For doped as-prepared samples the saturated conductivity is smaller than that of the undoped one and it further decreases with annealing, but does not vanish. This trend is the opposite to the one observed for the dc conductivity of the nanoparticles, where the dc conductivity increases with both annealing and doping. [61] This indicates that the carrier conductivity is dominated by hopping between defect states in the pellets. With annealing the intrinsic localized states not related to the doping disappear and the hopping conductivity is reduced. The only remaining hopping conductivity is connected with the localized states introduced by Nb doping. The dc conductivity is much lower than the Nb-induced hopping conductivity and it is strongly dependent on the doping density. This dependence can be explained through the variation of τ_{max} in the Dyre conductivity 2.2.7. With increasing doping density the hopping distance decreases, the longest hopping time thus shortens and the dc conductivity is enhanced.

In comparison with the conclusions of Ref. 65 we find that the volume fraction of NTO in the pellets is identical for almost all the samples. The hopping conductivity was found to be twice smaller in our study and the enhancement of losses very similar. The change of these two quantities with the doping, growth temperature and annealing are very similar to the findings in Ref. 65.

4.6 Conclusion

We studied the dielectric and conduction properties of TiO_2 mesoporous pellets undoped and doped by Nb using time-domain THz spectroscopy and microwave impedance spectroscopy. A model was developed explaining the relation between the microscopic and the macroscopic permittivity of the pellets appropriate for different degrees of percolation. The microscopic permittivity spectra are explained by enhancing the dielectric losses of bulk anatase due to extrinsic losses and by an additional hopping conductivity of charge carriers. From the analysis of the parameters of the model a picture of the conduction mechanism consistent with previous studies was developed:

- The dominating conduction mechanism in all the samples is carrier hopping

between localized states. The localized states not related to Nb doping are removed upon annealing, while hopping conductivity between localized states introduced by doping remains. Increased level of doping leads to smaller distance between localized states and thus higher dc conductivity.

- The crystallinity of the pellets improves with annealing for the undoped samples. However, Nb doping increases the extrinsic dielectric losses.
- The percolation of the grains in the pellets is significantly increased upon annealing.

Chapter 5

Electron dynamics in water

In nature, chemical reactions often occur in aqueous solutions. These reactions involve transport of charge between the reagents in the form of ions or electrons. The motion and the state of the solvated charged particles (ions or electrons) may affect crucially the products of the reaction. [66,67]

In this chapter, we study the dynamics of electrons in water generated by photoexcitation. On the one hand, investigation of the dynamics of an excess electron serves as a simple prototype for studying charge transport in liquids because electron lacks internal degrees of freedom (such as the electronic states of ions). On the other hand, the photogenerated electron itself plays an important role in a number of processes; for example, ionization of water with high-energy photons leads to corrosion in nuclear reactors [66], and high energy electrons in water damage important biomolecules like DNA. [67] Despite its importance, the generation mechanism of excess electrons and their subsequent localization process is not fully characterized yet and it is studied widely both theoretically by quantum mechanical simulations [68,69] and experimentally by optical pump–optical probe methods and pulse radiolysis. [70] During these experiments water or solvated ions are ionized and subsequently the optical spectra of the products are probed. Probing the optical spectra is ideal for the identification of solvated electrons. The ionization pathway may be completely different with different parameters of ionizing radiation (excitation energy, intensity) and under strong excitation the electron can become delocalized for a short time (tens or hundreds of femtoseconds). [71] To reveal the existence of the transient delocalized state we apply optical pump–THz probe spectroscopy to measure the photoconductivity spectra of neat water and of aqueous solutions of several salts.

5.1 Theoretical background

The electronic spectrum of water differs crucially from that of a bulk semiconductor:

- The structure of water is amorphous and therefore there are no bands corresponding to the individual states of excess electrons. Nevertheless, it is often possible to define a conduction band as a range of energies, for which charge carriers may be delocalized. A scheme of the energy spectrum of water is displayed in Fig. 5.1 a).
- Unlike in solid materials, the molecules in liquids are mobile. Consequently, these molecules may reorient themselves around a “foreign“ particle. This makes electronic transitions more complex than similar processes in solids. For example, photoionization of liquid water first involves the generation of an excess electron in a non-equilibrium state. This intermediate state can be a short-lived delocalized electron. Immediately after the ionization process the water molecules around the parent ion are oriented identically as they were before the photoexcitation. It means that this state (excess electron+parent ion+surrounding molecules) has a higher energy than the conduction band edge (see Fig. 5.1 b). Consequently, the bottom of the conduction band cannot be reached by a vertical ionization process. Subsequent fast relaxation involves reorientation of water molecules and a related decrease of free electron excess energy.

The product of the ionization of water and aqueous solutions is the **hydrated electron**. The hydrated (or solvated) electron is the ground state of the excess electron completely solvated in water. Its wavefunction is substantially influenced by the surrounding water molecules, which rapidly fluctuate in time. Consequently, its geometrical configuration is not constant in time and is difficult to describe. On average, it is surrounded by ~ 6 water molecules; the molecules point with one of their hydrogen atom in the direction of the solvated electron (see Fig. 5.2 a). The optical absorption spectra of the solvated electron consist of a broad peak centered at 720 nm (see Fig. 5.2 b) [73], which corresponds to the electronic transition from the ground (s-)state to a triplet p-state.

Due to the strong broadband absorption of the hydrated electron in the visible and near-infrared range, optical pump–optical probe spectroscopy is a tool frequently used to study its dynamics. The solvated electron is formed very quickly after photoexcitation, typically within less than 1 ps [71]. Once the solvation process completed, the absorption spectra of the solvated electron do not change any more during its lifetime ($\sim \mu\text{s} - \text{ms}$), and therefore probing at a single wavelength close to the absorption peak is sufficient to monitor the evolution of the solvated electron density. If there are no electron scavengers in the solution, the concentration of solvated electrons decays via geminate recombination (attachment to its parent ion or radical). From the decay of solvated electron concentration it is possible to calculate the average ejection length of the electron, i.e. the distance between the parent ion and the solvated electron immediately after its formation. It provides an indication about the ionization process itself; one can expect that different ionization pathways lead to different spatial and energetic electron dis-

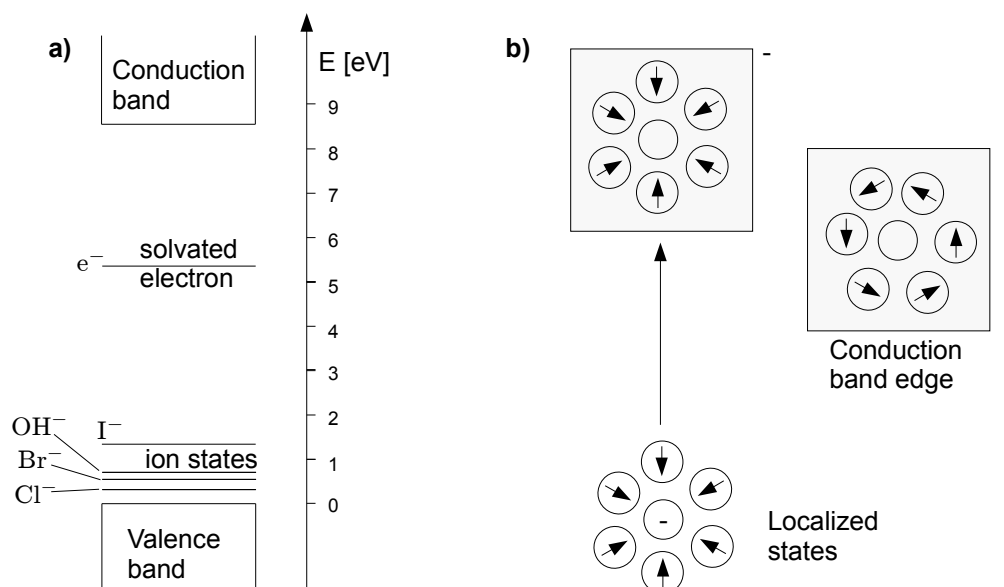


Figure 5.1: a) The energy spectrum of water, after [72]. The energy of the conduction band edge is only schematically shown. b) Simple illustration of the possible generation of a conduction band electron from a localized state (for example, a negative anion). The arrows indicate the dipole moment of H_2O molecules. The vertical ionization may bring the electron into a delocalized state with the orientation of the surrounding molecules identical to that of the ground state. This state has a higher energy than states at the conduction band edge because of a high electrostatic energy associated with this particular dipolar order. Reorientation of dipoles leads to an energy relaxation. [72]

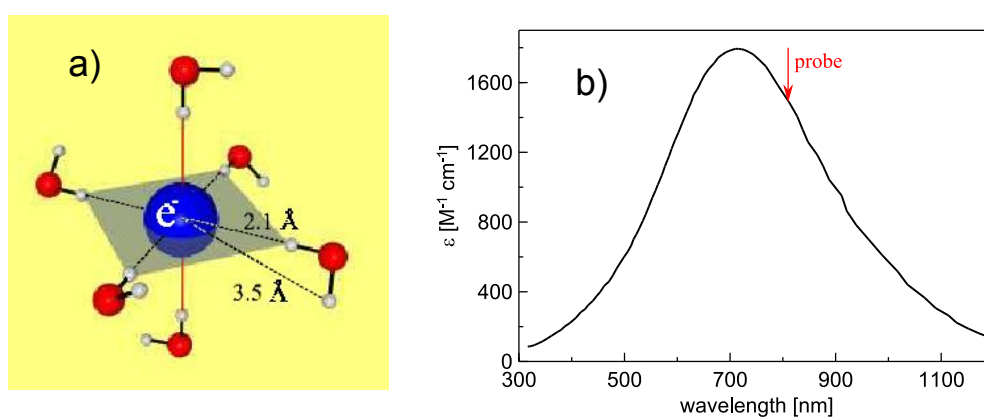


Figure 5.2: a) The approximate alignment of the solvated electron and the surrounding water molecules (from Ref. [74]). b) Spectrum of molar absorption coefficient of the solvated electron [75]

tributions and an electron ejected to the conduction band of water may escape far away – into a distance of several nanometers – from the parent ion. [76]

It has been shown that the ejection distance of an electron depends both on the conditions of photoexcitation and on the parent ion/molecule. [71] Based on the previous optical pump–optical probe studies and our experimental capabilities we generate excess electrons by photoexcitation at wavelengths 270 nm and 405 nm. We photoexcite both neat water and aqueous solutions of salts:

- The ionization energy of water is between 8 and 12.4 eV, therefore one can expect generation of delocalized electrons only by multiphoton excitation. However, the generation pathway of the solvated electron may involve also only excited states of the water molecule or excited state of the solvated electron (for example p-states) without any electron delocalization. [71]
- By the photoexcitation of aqueous solutions of salts, solvated electron can be generated also from the solvated anions of these salts. In this case the energy required for ionization is smaller than that for neat water (see Fig. 5.1 a). For low excitation intensities the electron-ion system is brought into a high energy state called charge transfer to solvent state (CTTS). The solvated electron is formed by the dissociation of this state. This process does not lead to the formation of conduction band electrons and the ejection distance of electrons is small (for example, for iodide anions less than 1 nm). However, for high excitation energies, which may be reached by multiphoton excitation, the electrons may be ejected into the conduction band. This was observed through the increase of the electron ejection length (~ 4 nm for iodide anions) [70].

5.2 Specific experimental details

In our experiments we used high pump intensities to induce multiphoton ionization processes. If the sample is poured in a cuvette, the strong excitation beam may induce nonlinear effects in the walls of the cuvette leading to parasite signals. Moreover at high salt concentrations the salt may be deposited on the walls, thus degrading the experiment. Consequently, in our experiments the use of cuvettes was omitted and the liquids were studied in the form of a thin free flowing gravity-driven liquid film. [47] The liquid flowed through a stainless steel nozzle and at its output it was guided by a piece of thin wire bent to a U-shape and attached to the nozzle at its ends. The liquid after flowing through the film (between the two branches of the U-shape) was collected in a reservoir and pumped back to the upper reservoir feeding the film. The schematic of the construction is shown in Fig. 5.2. [47] The thickness of the jet was ~ 100 μm ; it was measured by THz time-domain spectroscopy based on the knowledge of the THz refractive index of water ($n = 2.1 + i0.5$ [77]). The sample was probed in the transmission geometry

using the setups described in sections 3.3 and 3.4. Neat water and solutions of KI, NaCl, KBr were studied.

Optical pump–optical probe setup Optical pump–optical probe spectroscopy was applied for the study of solvated electron generation and in order to estimate the density of the generated solvated electrons. The wavelength of the pump beam was 270 nm and 405 nm. A probe beam with a wavelength of 810 nm was used to directly monitor the concentration of solvated electrons. The pump beam intensity was set to the highest value that could photoexcite the sample without disturbing the flow of the liquid in the jet ($\sim 2 \times 10^{21}$ photon.cm $^{-2}$ for 270 nm and $\sim 1 \times 10^{22}$ photon.cm $^{-2}$ for 405 nm excitation).

The change in the transmission of the optical probing pulse occurs due to the absorption of the solvated electrons. We assume that the excess electron generation occurs homogeneously in the sample. Consequently, the change of transient transmission can be expressed by the Beer-Lambert law:

$$\frac{\Delta T}{T} = 10^{-Lc_e\varepsilon_e} \quad (5.2.1)$$

where c_e is the molar concentration of the solvated electrons, ε_e the molar absorptivity of the electrons (see Fig. 5.2 b), L the thickness of the jet. From this equation the concentration of the generated solvated electrons was calculated.

Optical pump–THz probe setup Optical pump–THz probe spectroscopy was applied to reveal the presence of delocalized electron states within ~ 2 ps after the photoexcitation. The parameters of the pump branch were identical to that used in the optical pump–optical probe setup. The properties of the THz probe beam brought the following complications to the experiment:

- The width of the focused THz beam was 4 mm [49]. The width of the transmitted THz beam was defined by a metallic aperture behind the sample (3 mm). However, the pump beam needed to be focused on to the liquid jet to a spot with a waist of tens of microns in order to achieve a significant multiphoton absorption. Therefore the condition of homogeneous excitation over the cross section of the probe beam could not be fulfilled. Nevertheless it had been shown previously that it is possible to carry out a quantitative study of photogenerated free carriers in a photoionized gas under these conditions. [13]
- The THz box had to be hermetically closed and filled with helium during the experiments, because a strong transient THz absorption of photogenerated electrons in air, oxygen or nitrogen would make it impossible to detect delocalized electrons in the liquid jet. [13, 78] During the evacuation and refilling of the box the input tubes must have been clamped and the lower reservoir had to be empty in order to prevent evaporation of the sample into vacuum.

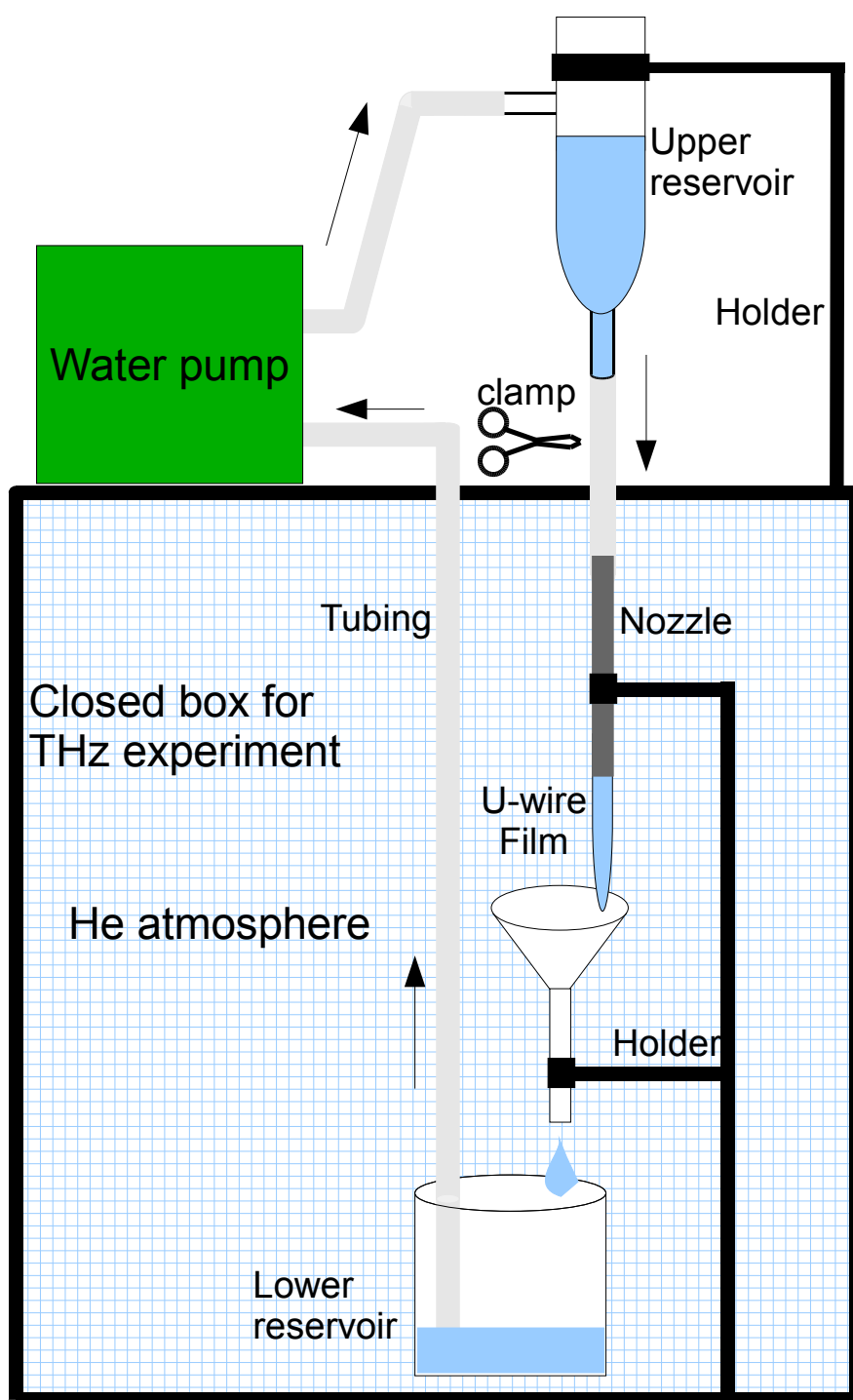


Figure 5.3: Illustration of the thin film flow system. The pump and probe pulses arrive to the sample from the front. The optical elements are not displayed in the figure for the simplicity.

	Ion concentration	Pump: 270 nm		Pump: 405 nm	
	c [mol.dm ⁻³]	$\Delta T/T$	N [cm ⁻³]	$\Delta T/T$	N [cm ⁻³]
water	—	0.12	2.2×10^{17}	0.10	1.8×10^{17}
NaCl	1	—	—	0.14	2.6×10^{17}
KBr	1	—	—	0.32	6.7×10^{17}
K₃Fe(CN)₆	1	0.16	3.0×10^{17}	—	—
KI	0.2	—	—	0.40	8.9×10^{17}
KI	1	0.16	3.0×10^{17}	—	—

Table 5.1: Summary of the measured OPOP signal amplitude and concentration of solvated electrons after photoionization.

5.3 Experimental results and discussion

In all cases the dynamics of the measured transient optical absorption signal (see Fig. 5.4) shows a behaviour similar to the ones observed in previous published studies [71] – the solvated electrons are formed very quickly, and their lifetime is much longer than 100 ps. The concentrations of solvated electrons for different ionization conditions are shown in Tab. 5.1. The highest excess electron density is observed in the solution of KI with a concentration of 0.2 mol/dm³ (0.2 M) photoexcited by 400 nm pump pulses. Moreover, in the behaviour of the solvated electron dynamics no decay is observed during the first 10 picoseconds. It implies that the electrons are ejected far from their parent ions, through the conduction band. Therefore we can assume that the highest concentration of delocalized electrons is generated by photoexcitation with 400 nm pulses in 0.2 M KI.

We have not observed any change in the THz transmission spectra of any of the liquids due to their photoionization. Based on the knowledge of the density of the generated electrons and on the assumption that all the electrons are formed through the same ionization mechanism we attempt to make a semi-quantitative conclusion about the possible delocalization of the intermediate electron states formed during the photoionization of water.

The lack of THz signal means that the change in the THz transmission was lower than the sensitivity of our THz setup. By a measurement of the noise level with the water jet and without pump we determined the lowest measurable transient THz signal. We set up a model of the electron conductivity in the conduction band of water which depends essentially on the extent of the electron delocalization. Based on this model we calculated transient THz waveforms which represent the signal we should have experimentally obtained for the given delocalization extent. By comparing the simulation results with the noise level we obtain a rough estimation of the upper limit of the degree of electron localization.

We use a model for the motion of conduction band electrons based on Monte-Carlo simulations discussed in subsection 2.2.7. A conduction band electron is assumed to move in a cavity with perfectly reflecting walls, i.e. the electron is

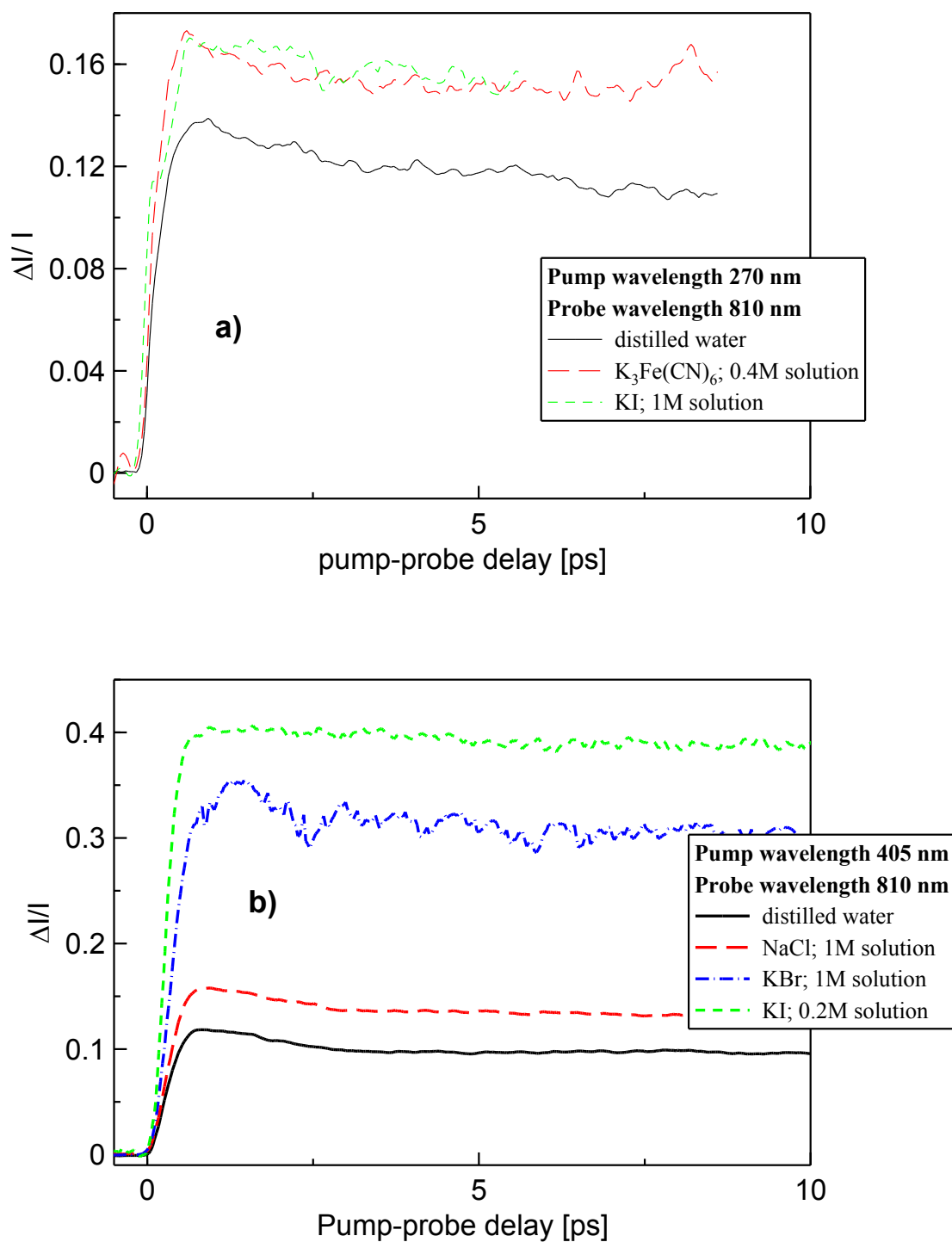


Figure 5.4: Transient optical absorption of solvated electrons in various solutions photoexcited by: a) 270 nm, b) 405 nm laser pulses.

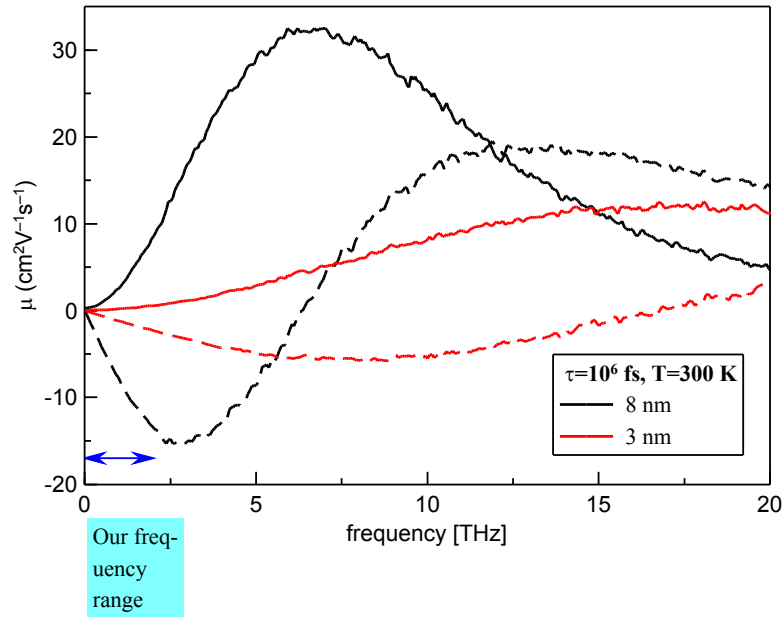


Figure 5.5: Mobility spectra of conduction band electrons calculated for two delocalization length scales. The solid lines show the real part, the dashed lines display the imaginary part of the mobility.

always reflected back upon interaction with the boundary of the cavity ($p_r = 1$ if we use the notation introduced in subsection 2.2.7). As the electron is expected to thermalize in the conduction band, its temperature is set to 300 K. We assume that the electron moves without scattering with water molecules and the scattering time is set to a large number ($\tau = 1000$ ps). The size of the cavity characterizes the extent of delocalization of the electron. From the simulation the electron mobility is obtained (several examples are shown in Fig. 5.5). The shape of the mobility spectra is very similar of that discussed in subsection 2.2.7. From the mobility we can easily calculate the transient conductivity of the photoexcited part of the sample (by using the electron densities summarized in Table 5.1) and subsequently the transient transmission function.

Here we have to address the problem of inhomogeneous photoexcitation of the water film, i.e. that the width of the excitation beam is smaller than that of the THz probe beam. It has been shown that such a configuration may result in a change of the shape of the transient transmission spectra due to separation of negatively and positively charged particles leading to transverse oscillations of the free carrier plasma. [13] In the current study we wished to estimate merely the amplitude of the transient transmitted THz waveform. For this estimation we did not need to consider a particular measured shape of the THz waveforms. In our evaluations of the transient transmission function we simply scaled the amplitude of the reference THz pulse by the ratio of the pump and probe beam spot sizes. The spot size of the pump beam was measured by a CCD camera at

the place of the sample. The size of the probe beam was defined by the aperture placed behind the jet.

From the transient transmission function and from the measured reference THz waveform the expected transient THz waveform can be evaluated. The results of the simulations are displayed for neat water and KI (the aqueous salt solution where the conduction band electron generation is the most apparent) in Fig. 5.6. One can see that for conduction band electrons with lifetime much longer than 1 ps the length scale of delocalization of the electrons must be at least 2-3 nm in order to be detected in our experiments. However, it has been shown that such states should have a lifetime $\lesssim 0.4$ ps. [71] We use the following procedure to account for the finite lifetime of delocalized electrons in our estimations. The simulated electron mobility spectra can be formally approximated by the Drude-Smith model (see Sec. 2.2.7 for detailed discussion). As the electron lifetime is shorter than the THz pulse length, the evolution of the transmitted transient THz spectra within 1 ps after photoexcitation is non-trivial – its spectral shape changes. Consequently, a careful analysis must involve the calculation of 2D transient data as described e.g. in [55,56]; the two dimensions are represented here by the detection (sampling) time and by the pump-probe delay. For a system exhibiting a response corresponding to the Drude-Smith model, the transient transmitted THz waveform reads:

$$\Delta E(\tau, \tau_p) \propto \exp\left(-\frac{\tau + \tau_p}{\tau_c}\right) Y(\tau + \tau_p) \int_0^{\tau + \tau_p} dt' E_0(\tau - t') \exp\left(-\frac{t'}{\tau_{DS}}\right) \left(1 + c_1 \frac{t'}{\tau_{DS}}\right) \quad (5.3.1)$$

where c_1 and τ_{DS} are the parameters of the Drude-Smith model, $Y(t)$ is the Heaviside step function and τ , τ_p have the same meaning as in the Section 3.3. The equation was derived based on Eq. 38 in Ref. 56. An example of a 2D map for delocalization length 12 nm and lifetime $\tau_c = 0.3$ ps is displayed in Fig. 5.7. After the calculation of such a 2D map we consider a THz waveform $\Delta E(\tau, \tau_p)$ for τ_p fixed at a value shortly after photoexcitation (0.1-0.3 ps) along our experimental conditions. This waveform is convoluted with the response function of the detector [57] and finally compared with the noise level of our system.

We have compared the detection capabilities of our setup with simulations of the transmitted transient THz signal for lifetimes $\tau_c = 0.1$ and 0.3 ps. The data are displayed in Fig. 5.8 for neat water and in Fig. 5.9 for the solution of KI. From the comparison it is clear that for neat water the largest possible delocalization length of electron states generated in our experiments is 12 – 20 nm, whereas for the solution of KI it is 5 nm.

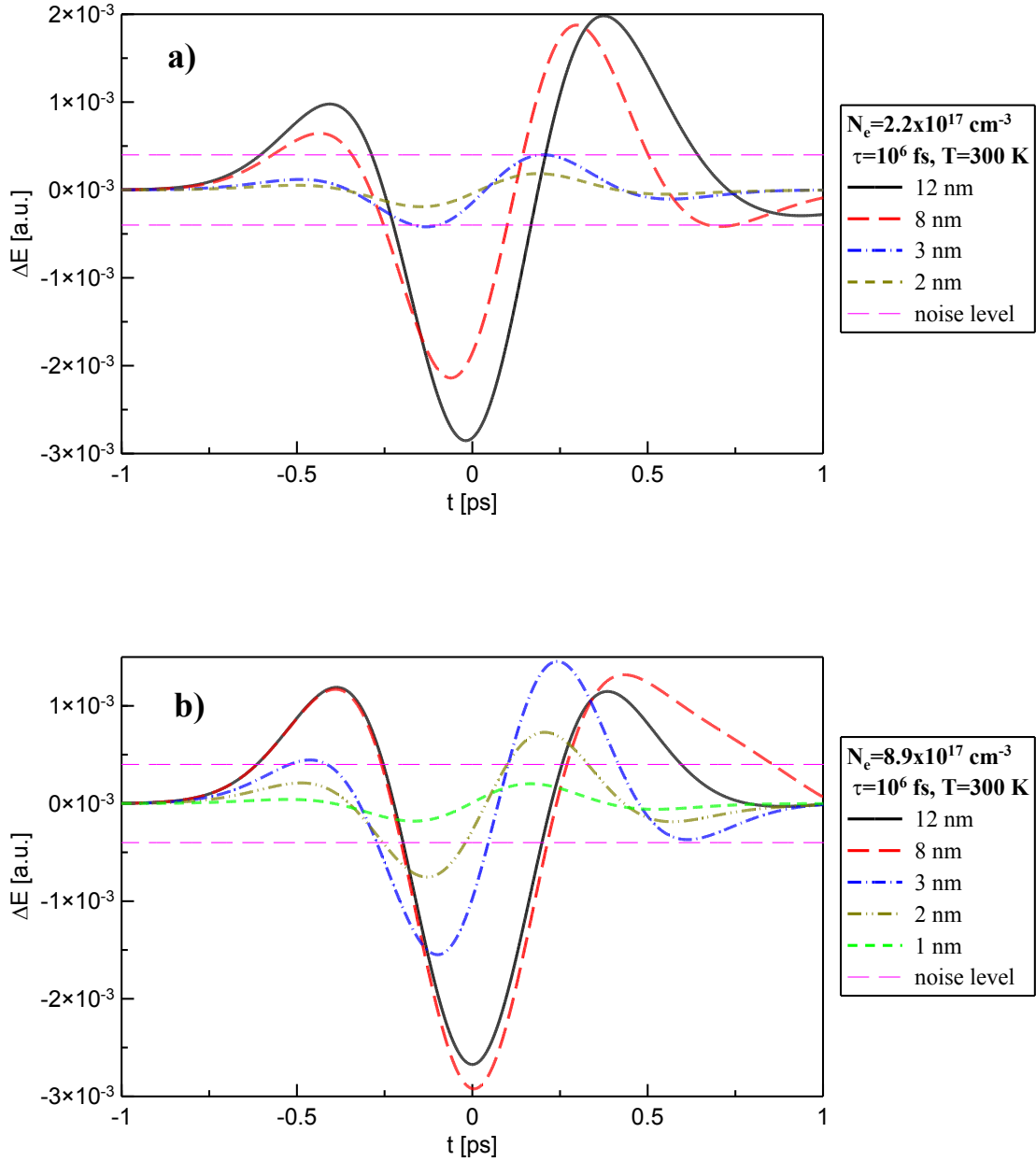


Figure 5.6: Transient THz signal evaluated by means of the simulations of the motion of conduction band electrons. The signal magnitude is compared with the noise level of our experiments. a) Simulation with electron concentration measured in neat water. b) Simulation with electron concentration measured in solution of KI. Electron lifetime $\gg 1$ ps.

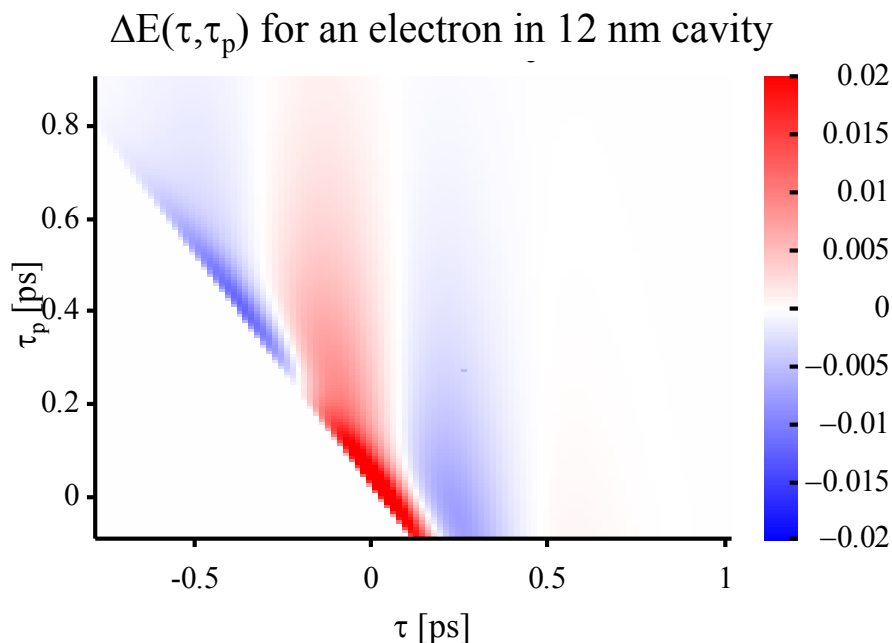


Figure 5.7: Two dimensional map of the transmitted transient waveform calculated for mobile electrons with a lifetime 0.3 ps in a cavity with diameter 12 nm.

5.4 Conclusion

We have applied optical pump–THz probe spectroscopy for probing delocalized electron states generated by multiphoton ionization in neat water and aqueous solutions of KI, KBr, NaCl and $\text{K}_3\text{Fe}(\text{CN})_6$. It was found that in our frequency range the delocalized electrons cannot be detected. By performing complementary optical pump–optical probe experiments we estimated the initial density of photogenerated electrons. We also have set up a classical model of the mobility of partially localized electrons by using Monte-Carlo simulations. A combination of the two approaches revealed that the intermediate electron states generated due to photoionization do not stay mobile on a length scale of ~ 5 nm longer than 100 fs.

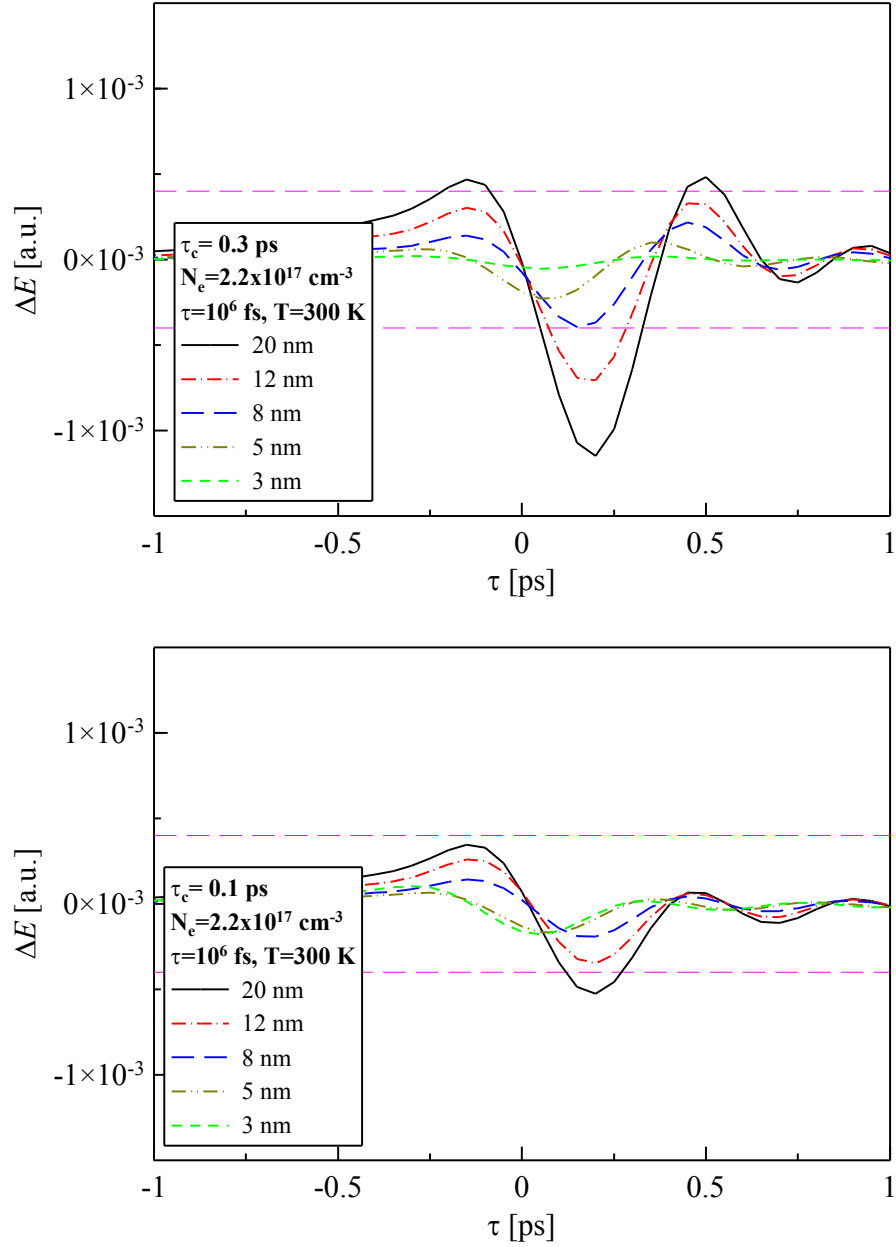


Figure 5.8: Transient THz signal evaluated by means of the simulations of the motion of conduction band electrons in photoexcited neat water. It is assumed that the electrons have a short lifetime. The signal magnitude is compared with the noise level of our experiments. a) The electron lifetime is $\tau_c = 0.3$ ps. b) The electron lifetime is $\tau_c = 0.1$ ps.

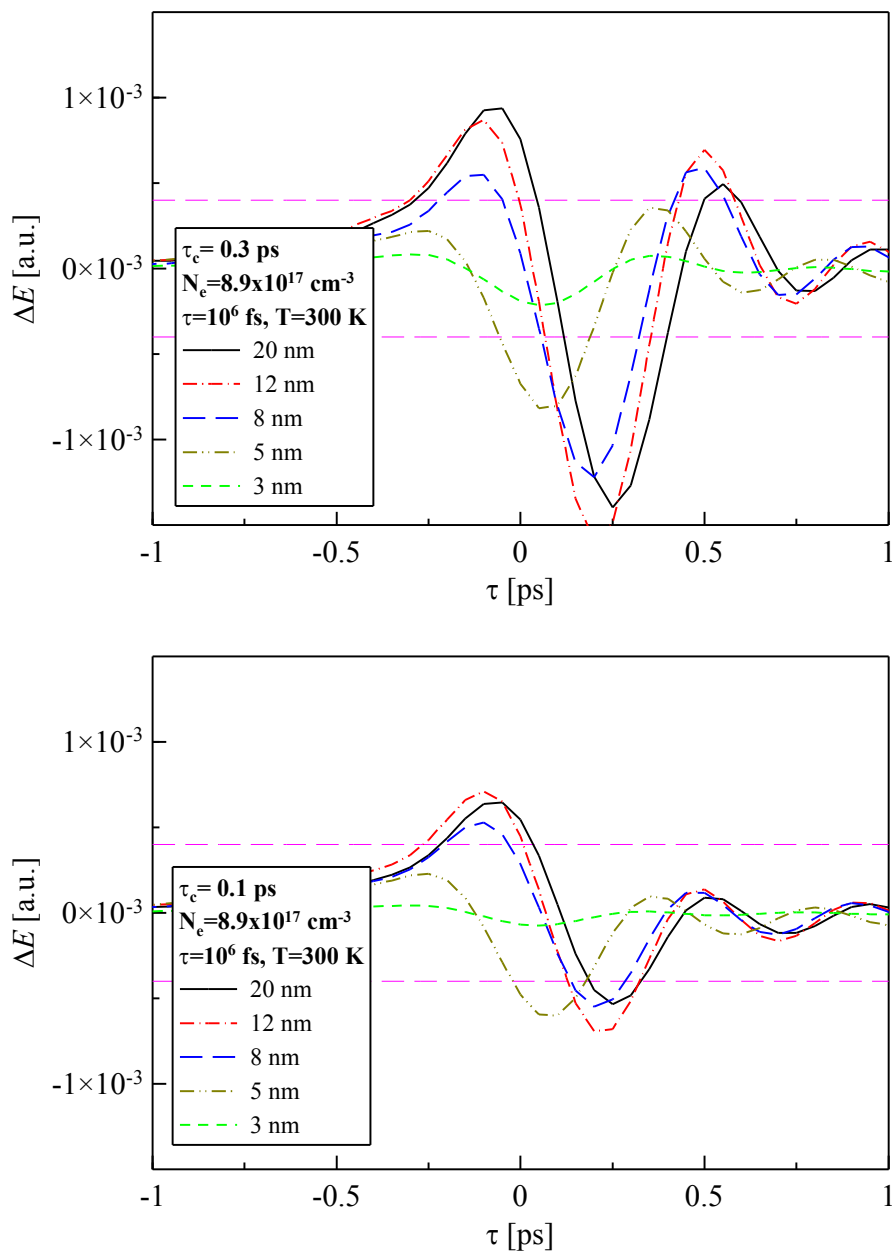


Figure 5.9: Transient THz signal evaluated by means of the simulations of the motion of conduction band electrons in aqueous solution of KI. It is assumed that the electrons have a short lifetime. The signal magnitude is compared with the noise level of our experiments. a) The electron lifetime is $\tau_c = 0.3 \text{ ps}$. b) The electron lifetime is $\tau_c = 0.1 \text{ ps}$.

Chapter 6

Electron transport in nanocrystalline and bulk ZnO

ZnO is a II-VI semiconductor with direct bandgap. Its fundamental properties are summarized in Tab. 6.1. One of the peculiar features is the relatively high exciton binding energy (~ 60 meV), which enables population of exciton levels at room temperature. As a result, ZnO is a promising material to be used as an active medium in a polariton laser, where the (stimulated) emission occurs through the radiative recombination of excitons. [79, 80] Furthermore, thin ZnO films find applications as transparent conductive electrodes [58], in transparent thin-film transistors [81] and in dye-sensitized nanostructured solar cells [82–84]. It has been shown that ZnO has a strong tendency for self-organized growth and it is a suitable material for growing nanostructures of various geometries, for example nanocrystals, nanorods, tetrapods, tubes etc. [85] We investigate the carrier transport in ZnO nanocrystals prepared by the sol-gel technique. [86] For this study we use optical pump–THz probe spectroscopy. The results are complemented by the study of carrier transport in bulk ZnO under the same experimental conditions.

Crystal structure	hexagonal-wurzite
Bandgap (300 K)	3.44 eV
Exciton binding energy	~ 60 meV
Bohr radius of exciton	~ 2 nm
electron effective mass	$0.28 m_e$
light hole eff. mass	$0.31 m_e$
heavy hole eff. mass	$0.55 - 0.59 m_e$
Mott density	$3 \times 10^{17} - 2 \times 10^{18} \text{ cm}^{-3}$
THz refraction index	2.8
refraction index at 266 nm	$2.1 + i0.6$

Table 6.1: Some important properties of bulk ZnO [80, 85]

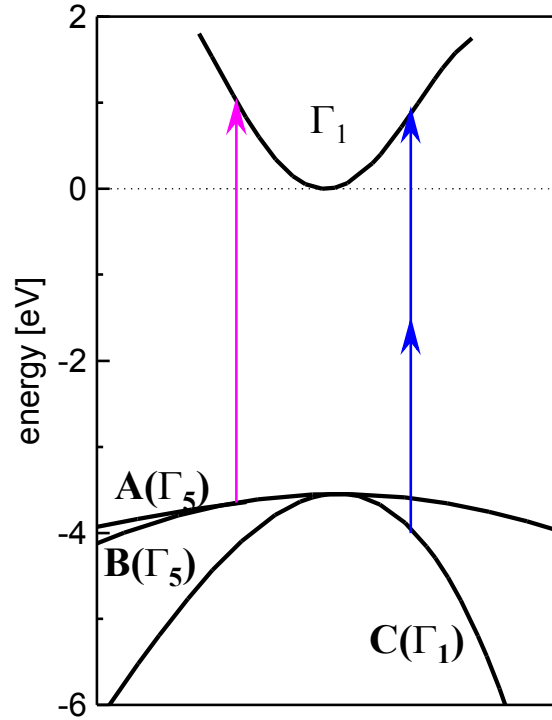


Figure 6.1: Band structure of ZnO. The arrows indicate the allowed electron-hole pair generation pathways for one-photon and two-photon absorption in the case of $\mathbf{E} \perp \mathbf{c}$. The valence band consists of three bands: a pair of heavy-hole bands split by the spin-orbital interaction (**A**,**B**) and the band of light holes (**C**)

6.1 Recent THz studies of bulk and nanocrystalline ZnO

6.1.1 Bulk ZnO

For the investigation of the photoconductivity of ZnO, we should consider the following properties:

- As ZnO crystallizes in the hexagonal wurtzite structure, the orientation of the polar hexagonal (\mathbf{c}) axis of the crystal cell with respect to the optical excitation field may have a crucial effect on the properties of the generated charges. For example, due to symmetry reasons, different selection rules apply for exciton absorption with an optical field parallel or perpendicular to the \mathbf{c} -axis. Excitons with A- and B-holes absorb radiation with electric field perpendicular to \mathbf{c} , C-excitons absorb photons with polarization parallel to \mathbf{c} (see Fig. 6.1). [85]
- The excitation density essentially determines the nature of photoconductivity in bulk ZnO. For low excitation densities a considerable fraction of

charge carriers form excitons. On the other hand, at high excitation densities, above the Mott density the electron-hole interaction becomes screened and the excitons disappear. For ZnO the Mott transition is expected to occur in the carrier density range of $3 \times 10^{17} - 2 \times 10^{18} \text{ cm}^{-3}$ [85, 87].

- Several methods exist for the growth of ZnO crystals. The parameters and method of growth may determine the density of defects in the crystal and affect both its photoconductivity and carrier dynamics.

Baxter et al. studied a ZnO crystal in the (0001) orientation (i.e. the **c**-axis perpendicular to the crystal surface) grown by the sublimation technique. The sample was photoexcited at the wavelength of 387 and 400 nm, which generated electrons through two-photon absorption. This way the whole volume of the sample was photoexcited, and the conductivity of carriers at relatively low concentration (down to 10^{14} cm^{-3}) could be measured. The study was carried out at temperatures of 10, 40 and 80 K. It was found that for all temperatures and for all excitation densities used the photoconductivity was dominated by a Drude-like behaviour, with scattering times 250-500 fs. The dynamics of the THz signal was governed by the decay of the carrier concentration and by the decrease of the carrier scattering time (or equivalently of the mobility) with increasing pump-probe delay. The Drude-like behaviour was attributed to the response of photogenerated electrons and holes; in this experimental configuration (i.e. two-photon absorption with the polarization of the optical electric field perpendicular to the **c**-axis) only light holes and electrons are initially generated due to the selection rules. The decrease of the scattering time was then attributed to the relaxation of the light holes into heavy hole states. No oscillatory response originating from excitons was detected. [88]

Hendry et al. studied ZnO crystals grown by the hydrothermal method which is supposed to produce crystals with low density of defects. Crystals with orientations (0001) and (10 $\bar{1}$ 0) were studied. The photoconductivity of ZnO was found to be independent of the orientation of the crystal, and it was studied for both low (carrier density under the Mott transition limit) and high (above the Mott density) excitation densities [18, 89]:

- Using pump pulses with wavelength 400 nm a low uniform photocarrier density of up to $2 \times 10^{16} \text{ cm}^{-3}$ was generated in the entire volume of the sample. It has been found that immediately after photoexcitation the photoconductivity followed the Drude-like behaviour with the scattering time ~ 80 fs. In the following 100 picoseconds a part of the initial free electrons and holes recombined into excitons and eventually formed a stable system of excitons and free carriers in thermal equilibrium with each other; measurements at temperatures between 20 K and 140 K showed that the free-carrier fraction in this quasi-equilibrium state follows an Arrhenius like behaviour with temperature. The activation energy of this temperature dependence was found to be close to the binding energy of excitons 60 meV.

The excitons were distinguished from the free carriers owing to the different shape of their complex conductivity spectra: the response of the free carriers is Drude-like (Eq. 2.2.2) while the contribution of the excitons follows the harmonic oscillator model (Eq. 2.2.4). The oscillator circular frequency of the exciton was found to be $\omega_0 = 50 \text{ rad.ps}^{-1}$ and the damping frequency was $\gamma = 6 \text{ ps}^{-1}$.

- Using pump pulses with a wavelength of 270 nm high excitation densities (initial carrier density up to 10^{20} cm^{-3}) were achieved. The photoconductivity was found to be constant in the whole THz frequency range with a positive real part and negligible imaginary part. It corresponds to a Drude-like response of a dense electron-hole plasma with very short scattering time. The density of carriers was found to decay rapidly but after approximately 100 ps the decay slows down considerably: they observe an electron-hole plasma with a constant density $\sim 2 \times 10^{18} \text{ cm}^{-3}$. This plasma does not decay for at least one nanosecond and its density is independent of temperature and initial excitation density. The decay of the carrier density is independent of temperature and its time constant decreases with increasing excitation density. The carrier decay was attributed to the Auger recombination process, although no quantitative analysis was carried out.

From this summary one can see that a wide variety of electron and hole states can be generated by photoexcitation in bulk ZnO. In an attempt to further increase the level of understanding of the mechanisms of photoconductivity in ZnO for high density of photocarriers, we carried out time-resolved THz studies of bulk ZnO at photocarrier densities near and above the Mott transition.

6.1.2 Nanocrystalline ZnO

The most complete study of the mobility of nanostructures of ZnO was presented by *Baxter et al.* They studied both the intrinsic conductivity and the photoconductivity of thin films of ZnO, ZnO nanowires and mesoporous nanoparticle films of ZnO. The measured photoconductivity spectra were described by the Drude-Smith model. [31] However, the parameters in the Drude-Smith model are phenomenological and provide only an intuitive picture of the carrier localization in nanostructures (see Subsection 2.2.6).

We study the photoconductivity of nanocrystalline ZnO using the combination of time-resolved THz spectroscopy and Monte-Carlo simulations. The parameters of these simulations have a direct microscopic physical meaning. Such a study also provides a good opportunity to test our model for different temperatures and carrier densities.

Němec et al. investigated the dynamics of photoconductivity in dye sensitized ZnO nanocrystals. By using two different pump wavelengths Němec could distinguish the electrons injected from the photoexcited dye and those photogenerated

directly by an interband transition in the semiconductor. The mobility of the injected electrons was found to be substantially lower due to their electrostatic interaction with the dye cations. [34]

For our studies we used the same samples as the ones investigated in that paper. However, here we focused on the transport of the directly generated charges: the pump wavelength was chosen such that no photoinjection from the dye occurred. The electron mobility of photocarriers generated in ZnO is then more thoroughly investigated than in Ref. 34; it is measured for several selected temperatures between 293 and 20 K and for a wide range of electron concentrations ($1 \times 10^{17} - 3 \times 10^{19} \text{ cm}^{-3}$).

6.2 Electron mobility and dynamics in bulk ZnO

We measured the photoconductivity of a (0001)-oriented ZnO crystal prepared by the company MTI using the hydrothermal method. Excitation wavelength of 270 nm was used at pump fluences of $1 \times 10^{12} - 2 \times 10^{14} \text{ photon.cm}^{-2}$. This excitation wavelength corresponds to the photon energy of 4.5 eV, which exceeds that of the ZnO bandgap; therefore the electron-hole pairs are generated by one-photon absorption. The skin depth of the pump beam in ZnO is $\sim 35 \text{ nm}$; the density of excitations per pulse in the thin photoexcited layer of ZnO is thus in the range $3 \times 10^{17} - 7 \times 10^{19} \text{ cm}^{-3}$. The measurements were carried out at temperatures 20, 80, 120, 293 K. It has been found that the dynamics of the photoconductivity of the ZnO crystal changes slowly compared to the temporal length of the probing THz pulse, therefore the measured data can be analyzed using the quasi-steady state approximation described in Subsection 3.3.3. Here we present the evolution of the absolute value of the carrier yield-mobility product at a selected frequency (1 THz) and the measured mobility spectra at selected pump-probe delay times.

The measured dynamics of the yield-mobility product at 20 K are displayed in Fig. 6.2. It can be seen that the evolution of the curves with increasing pump fluence is non-trivial; namely, for some excitation densities a non-monotonic decay is observed. For high excitation densities the yield-mobility product builds up slowly with a flat maximum lasting for several picoseconds, while at excitation densities lower than $3 \times 10^{19} \text{ photon.cm}^{-3}$ the signal reaches its maximum in less than 1 ps after photoexcitation. In the high-excitation regime the time constant of the decay does not vary much with the excitation density. For lower excitation densities (lower than $3 \times 10^{19} \text{ photon.cm}^{-3}$) the decay becomes faster. At excitation densities $1.7 \times 10^{18} - 1.7 \times 10^{19} \text{ photon.cm}^{-3}$ the dynamics is non-monotonic and starts to increase about 40 ps after photoexcitation. This second increase of the signal lasts approximately for 50 picoseconds.

To reveal the mechanism behind this complicated and strongly nonlinear dynamics we examined the THz yield-mobility spectra at several time delays se-

ZnO: 20 K

$N_{\text{exc}} = 6.4 \times 10^{19} \text{ photon.cm}^{-3}$				
delay [ps]	A [$\text{cm}^2\text{V}^{-1}\text{s}^{-1}$]	ξ_A	τ_A [fs]	B [$\text{cm}^2\text{V}^{-1}\text{s}^{-1}$]
10	93	0.53	28	–
40	30	0.01	470	40
120	51	0.02	470	10
200	32	0.01	470	6

$N_{\text{exc}} = 3.8 \times 10^{19} \text{ photon.cm}^{-3}$				
delay [ps]	A [$\text{cm}^2\text{V}^{-1}\text{s}^{-1}$]	ξ_A	τ_A [fs]	B [$\text{cm}^2\text{V}^{-1}\text{s}^{-1}$]
10	100	0.79	21	–
40	34	0.01	460	44
120	69	0.02	460	13
200	41	0.01	460	9

$N_{\text{exc}} = 1.7 \times 10^{19} \text{ photon.cm}^{-3}$				
delay [ps]	A [$\text{cm}^2\text{V}^{-1}\text{s}^{-1}$]	ξ_A	τ_A [fs]	B [$\text{cm}^2\text{V}^{-1}\text{s}^{-1}$]
10	95	1.26	12	–
40	45	0.01	500	32
90	110	0.04	500	19
120	100	0.03	500	17
200	65	0.02	500	15

$N_{\text{exc}} = 1.7 \times 10^{18} \text{ photon.cm}^{-3}$				
delay [ps]	A [$\text{cm}^2\text{V}^{-1}\text{s}^{-1}$]	ξ_A	τ_A [fs]	B [$\text{cm}^2\text{V}^{-1}\text{s}^{-1}$]
6	120	0.08	250	47
10	68	0.03	400	44
23	67	0.03	400	31
86	90	0.04	400	29
200	60	0.02	400	29

Table 6.2: Fit parameters for the yield-mobility spectra of the ZnO crystal measured at 20 K.

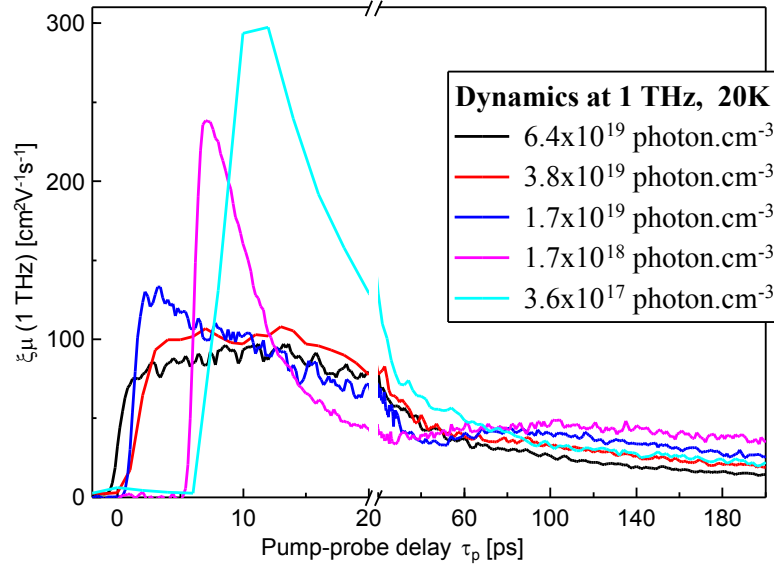


Figure 6.2: Dynamics of the carrier yield-mobility product at 1 THz, temperature 20 K. For clarity the time origin of the curves is shifted.

lected in a way to cover all the important phases of the dynamical behaviour of the sample.

We detected three different components in the yield-mobility spectra:

- A Drude-like contribution with scattering time of 10 – 500 fs. We refer to this component as component **A**. Its mobility is described with the expression:

$$\xi_A \mu_A = \frac{A}{1 - i\omega\tau_A} \quad (6.2.1)$$

The yield of this Drude term can be calculated by comparing the Eq. 6.2.1 with Eq. 2.2.2. One obtains:

$$\xi_A = \frac{Am}{q\tau_A} \quad (6.2.2)$$

where m is the effective mass of the particles, q is their charge and τ_A their momentum scattering time.

- A Drude-like contribution with scattering time less than 10 fs. We refer to this component as component **B**. Its mobility is approximately constant in our frequency range and the imaginary part of the mobility is close to zero. As a result, the precise value of the scattering time cannot be determined from the measured spectra, we can only set its upper limit $\tau_B \leq 10$ fs. We describe the contribution of this component to the mobility as B , a real constant. For this component the yield cannot be determined due to the unknown scattering time.

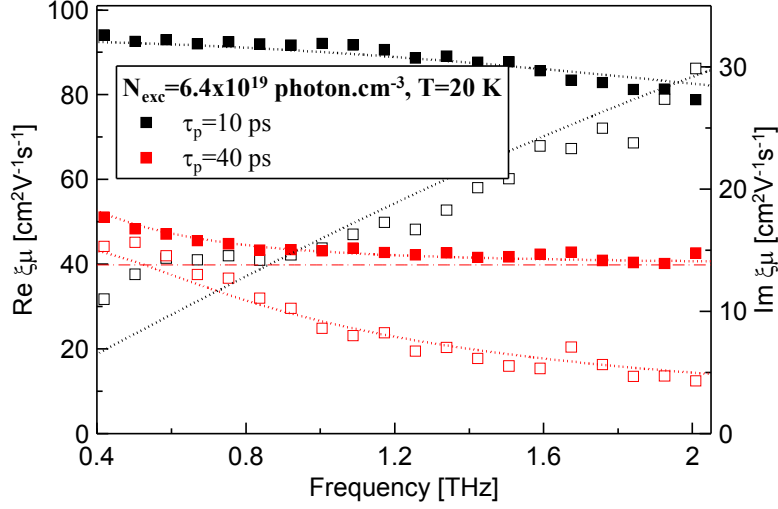


Figure 6.3: Spectra of the yield-mobility product measured at 20 K with excitation density 6.4×10^{19} photon.cm $^{-3}$, pump-probe delays 10 and 40 ps. The symbols indicate the experimental data. Closed symbols show the real part of the yield-mobility product (left axis), open symbols display the imaginary part (right axis). The lines show the fits of the data. A two-component Drude model is used for $\tau_p = 40$ ps (here the dash-dotted line indicates the contribution of the Drude term with very short scattering time to the real part of $\xi\mu$).

- At temperatures ≥ 80 K we detect also components with a small real mobility and a negative imaginary mobility which is decreasing with frequency. This type of response is well described by the oscillator model (Eq. 2.2.4) and is attributed to excitons. The value of the damping and oscillation frequency is taken from Ref. 18:

$$\omega_0 = 50 \text{ rad.ps}^{-1} \quad \text{and} \quad \gamma = 6 \text{ ps}^{-1}$$

These values were found to characterize well the oscillatory spectra of the excitons detected in our measurements. We refer to this component as to the component **C**. The yield of excitons can be calculated by comparing the amplitude of the component with Eq. 2.2.4:

$$\xi_C = \frac{C m_{red}}{q} \quad (6.2.3)$$

where m_{red} is the reduced mass of the exciton:

$$m_{red} = \frac{m_{elec} m_{hole}}{m_{elec} + m_{hole}} \quad (6.2.4)$$

Its value is approximately $0.2m_e$ for excitons composed from electrons (m_{elec}) and heavy holes (m_{hole}).

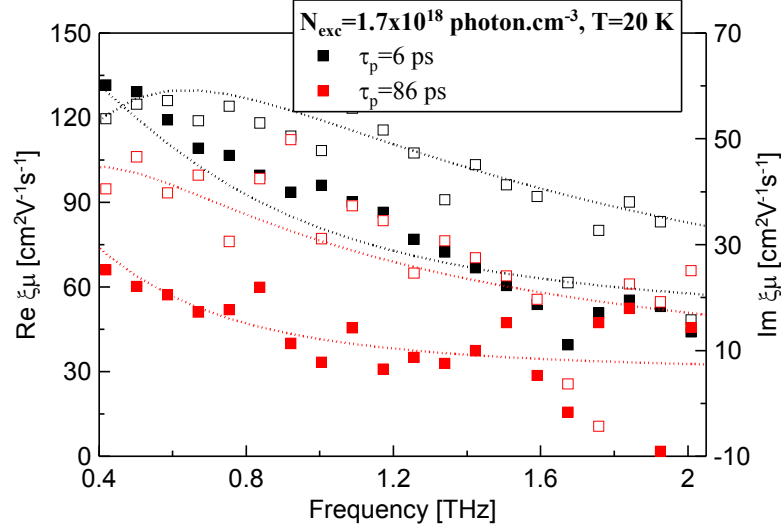


Figure 6.4: Spectra of the yield-mobility product measured at 20 K with excitation density 1.7×10^{18} photon.cm $^{-3}$, pump-probe delays 6 and 86 ps. The symbols indicate the experimental data. Closed symbols show the real part of the yield-mobility product (left axis), the open symbols display the imaginary part (right axis). The lines show the fits of the data (two-component Drude model).

To map completely the behaviour of the photoexcited carriers we use a model of mobility described by a sum of a Drude-term, a constant and an oscillatory term corresponding to the excitons:

$$\xi\mu = \frac{A}{1 - i\omega\tau_A} + B - \frac{C i\omega}{\omega_0^2 - \omega^2 - i\omega\gamma} \quad (6.2.5)$$

At 20 K it has been found that the mobility spectra are dominated by the Drude response for all time delays; excitons were not detected. The values extracted from a fit of the spectra using the equation 6.2.5 are displayed in Tab. 6.2. For the excitation densities $(1 - 6) \times 10^{19}$ photon.cm $^{-3}$ (black, red and dark-blue curves in Fig. 6.2 and the corresponding parts of Tab. 6.2) a system of free carriers is immediately formed with Drude-like mobility. This system may be composed of charge carriers with a distribution of scattering times; the average scattering time of the whole system is in the range of 10-30 fs. The yield ξ_A of this component is close to unity. For the excitation density of 1.7×10^{19} photon.cm $^{-3}$ the value ξ_A exceeds unity (see Tab. 6.2); this is due to the large error in the determination of the scattering time τ_A . In fact, the value $\tau_A = 12$ fs obtained from the fit is very close to the limit value of ~ 10 fs which can be experimentally resolved. It is then likely that the true value of τ_A is somewhat larger and ξ_A is close to unity.

During the initial 30 picoseconds the shape of the mobility spectra undergoes a significant modification related to dramatic changes in the transport mechanisms.

For $\tau_p \gtrsim \sim 30$ ps the spectra can be described by a sum of two Drude contributions: one with the scattering time in the range of 400-500 fs (denoted as A) and the other (denoted as B) with a very short scattering time (see Fig. 6.3). For lower excitation densities ($< 2 \times 10^{18}$ photon.cm⁻³) the mixture of two systems of charge carriers with long and short scattering times is formed immediately after photoexcitation (see Fig. 6.4).

The two Drude-like contributions (A and B) are spatially separated, i.e. they originate from different areas of the sample:

- The contribution A with long scattering time may be attributed to carriers generated deep in the ZnO crystal (deeper than the skin depth). In these regions the carrier concentration is low, therefore their response may resemble the one observed by Baxter et al. in Ref. 88.
- The contribution B characterized by the flat spectra can be associated with the formation of electron-hole plasma as it was observed by Hendry et al. in Ref. 18.

Although the number of carriers generated deep inside the crystal is smaller than that in the upper layer (the yield of the component A equals to only 0.01 – 0.05, see Tab. 6.2), their mobility is much higher due to the long scattering time. Consequently, they contribute significantly to the total THz signal. The measured carrier dynamics support this theory; after photoexcitation the total density of the electron-hole plasma decays from its initial value, while the contribution to the photoconductivity by high-mobility carriers raises until ~ 120 ps after photoexcitation and then starts to decay (see the increase of ξ_A in Tab. 6.2 observed between 40 and 90 or 120 ps after photoexcitation). This mechanism causes the non-monotonic behaviour of the THz signal at 1 THz for the excitation density 1.7×10^{19} photon.cm⁻³ (Fig. 6.2, pink curve). This late growth of the concentration of high-mobility carriers may be due to the diffusion of carriers from the dense plasma deeper into the sample.

At 80 K the dynamics of the yield-mobility product (see Fig. 6.5) is similar to that measured at 20 K, except for the fact that monotonic decrease is observed for each excitation density at 80 K. The lack of the late increase of the signal suggests that there are no such high-mobility states as at 20 K. From the examination of the measured spectra of the yield-mobility product it follows that the photoexcited carriers behave differently at different excitation densities. The yield-mobility spectra are fitted by the equation 6.2.5 and the parameters of the fit are listed in Tab. 6.3. For high excitation densities $(1 - 7) \times 10^{19}$ photon.cm⁻³ an electron-hole plasma is formed and the mobility of carriers in this plasma follows the Drude model with scattering times $\lesssim 10$ fs. Again values ξ_A exceeding unity are related to the uncertainty of the scattering time τ_A when its value is close to 10 fs. During the subsequent 200 picoseconds the density of carriers decreases and excitons are formed (see Tab. 6.3: the parameter C becomes greater

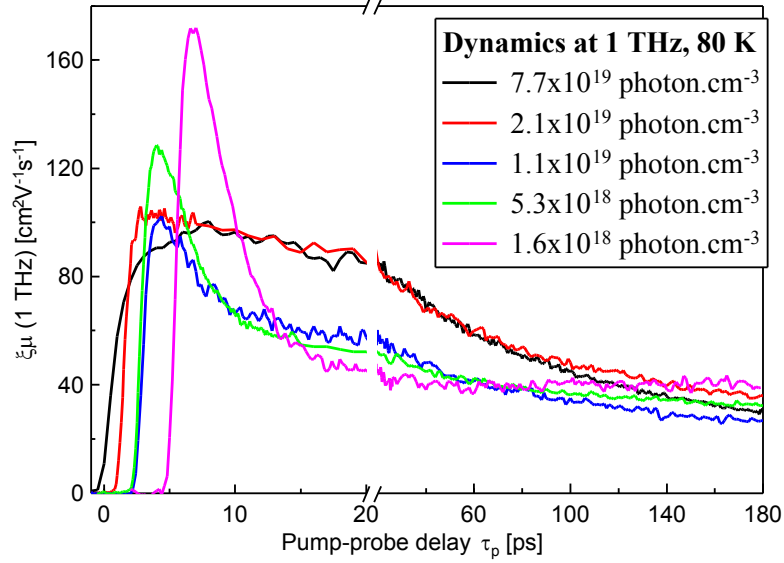


Figure 6.5: Dynamics of the carrier yield-mobility product at 1 THz, temperature 80 K. For clarity the time origin of the curves is shifted.

than zero for pump-probe delay 200 ps). The presence of excitons is directly inferred from the negative imaginary part of the mobility (see the spectra in Fig. 6.6). For lower excitation densities (5.3×10^{18} photon.cm $^{-3}$) excitons are formed more rapidly, they can be observed already 10 ps after photoexcitation (C is nonzero for these excitation intensities, cf. Tab. 6.3). The sum of the yields of free carriers and excitons ($\xi_A + \xi_c$) is close to unity 10 ps after photoexcitation. For even lower excitation densities (lower than 2×10^{18} photon.cm $^{-3}$), the excitons are not observed; instead, similarly as at 20 K, the carrier mobility can be described by the sum of a Drude-like term (A) with scattering time ~ 200 fs and a term (B) with constant real mobility (see Fig. 6.7). This behaviour is analogous to the one observed at 20 K, although the scattering time of the high-mobility carriers is twice smaller. The excitons may be generated in the deeper photoexcited regions of the sample, where the carrier concentration is low. It is not clear however, why their contribution vanishes when the excitation density is lowered to values of 1.6×10^{18} photon.cm $^{-3}$. Interestingly, it seems from our measurements that the presence of high-mobility states and excitons exclude each other. These two species were not observed simultaneously in any of the previous THz studies of bulk ZnO either. The reason may be that the high transient absorption of the high-mobility states hides the excitons, which have weaker absorption in our frequency range.

The threshold excitation intensity, where the behaviour of carriers changes, is similar at 20 and 80 K: it is around 1.6×10^{18} photon.cm $^{-3}$ and close to the Mott density.

At 120 K the yield-mobility spectra were fit by the equation 6.2.5. The results

ZnO: 80 K

$N_{\text{exc}} = 7.7 \times 10^{19} \text{ photon.cm}^{-3}$						
delay [ps]	A [$\text{cm}^2\text{V}^{-1}\text{s}^{-1}$]	ξ_A	τ_A [fs]	B [$\text{cm}^2\text{V}^{-1}\text{s}^{-1}$]	C [$10^{12} \text{ cm}^2\text{V}^{-1}$]	ξ_C
20	84	1.21	11	–	–	–
200	–	–	–	27	630	0.07

$N_{\text{exc}} = 2.1 \times 10^{19} \text{ photon.cm}^{-3}$						
delay [ps]	A [$\text{cm}^2\text{V}^{-1}\text{s}^{-1}$]	ξ_A	τ_A [fs]	B [$\text{cm}^2\text{V}^{-1}\text{s}^{-1}$]	C [$10^{12} \text{ cm}^2\text{V}^{-1}$]	ξ_C
10	93	1.49	10	–	–	–
200	32	0.17	30	–	3000	0.34

$N_{\text{exc}} = 1.1 \times 10^{19} \text{ photon.cm}^{-3}$						
delay [ps]	A [$\text{cm}^2\text{V}^{-1}\text{s}^{-1}$]	ξ_A	τ_A [fs]	B [$\text{cm}^2\text{V}^{-1}\text{s}^{-1}$]	C [$10^{12} \text{ cm}^2\text{V}^{-1}$]	ξ_C
5	–	–	–	81	–	–
20	–	–	–	57	1800	0.2
200	29	0.09	52	–	4100	0.46

$N_{\text{exc}} = 5.3 \times 10^{18} \text{ photon.cm}^{-3}$						
delay [ps]	A [$\text{cm}^2\text{V}^{-1}\text{s}^{-1}$]	ξ_A	τ_A [fs]	B [$\text{cm}^2\text{V}^{-1}\text{s}^{-1}$]	C [$10^{12} \text{ cm}^2\text{V}^{-1}$]	ξ_C
10	61	0.39	25	–	5000	0.57
200	35	0.1	54	–	4600	0.52

$N_{\text{exc}} = 1.6 \times 10^{18} \text{ photon.cm}^{-3}$						
delay [ps]	A [$\text{cm}^2\text{V}^{-1}\text{s}^{-1}$]	ξ_A	τ_A [fs]	B [$\text{cm}^2\text{V}^{-1}\text{s}^{-1}$]	C [$10^{12} \text{ cm}^2\text{V}^{-1}$]	ξ_C
2	106	0.09	190	69	–	–
200	24	0.02	240	34	–	–

$N_{\text{exc}} = 4.3 \times 10^{17} \text{ photon.cm}^{-3}$						
delay [ps]	A [$\text{cm}^2\text{V}^{-1}\text{s}^{-1}$]	ξ_A	τ_A [fs]	B [$\text{cm}^2\text{V}^{-1}\text{s}^{-1}$]	C [$10^{12} \text{ cm}^2\text{V}^{-1}$]	ξ_C
4	310	0.26	188	85	–	–

Table 6.3: Fit parameters for the yield-mobility spectra of the ZnO crystal measured at 80 K.

ZnO: 120 K

$N_{\text{exc}} = 7.7 \times 10^{19} \text{ photon.cm}^{-3}$						
delay [ps]	A [$\text{cm}^2\text{V}^{-1}\text{s}^{-1}$]	ξ_A	τ_A [fs]	B [$\text{cm}^2\text{V}^{-1}\text{s}^{-1}$]	C [$10^{12} \text{ cm}^2\text{V}^{-1}$]	ξ_C
10	–	–	–	67	–	–
200	–	–	–	34	–	–

$N_{\text{exc}} = 2.2 \times 10^{19} \text{ photon.cm}^{-3}$						
delay [ps]	A [$\text{cm}^2\text{V}^{-1}\text{s}^{-1}$]	ξ_A	τ_A [fs]	B [$\text{cm}^2\text{V}^{-1}\text{s}^{-1}$]	C [$10^{12} \text{ cm}^2\text{V}^{-1}$]	ξ_C
10	–	–	–	74	–	–
200	–	–	–	46	–	–

$N_{\text{exc}} = 1.2 \times 10^{19} \text{ photon.cm}^{-3}$						
delay [ps]	A [$\text{cm}^2\text{V}^{-1}\text{s}^{-1}$]	ξ_A	τ_A [fs]	B [$\text{cm}^2\text{V}^{-1}\text{s}^{-1}$]	C [$10^{12} \text{ cm}^2\text{V}^{-1}$]	ξ_C
3.6	89	0.49	29	–	6100	0.69
20	76	0.42	29	–	6500	0.74
200	55	0.30	29	–	3900	0.44

$N_{\text{exc}} = 4.4 \times 10^{18} \text{ photon.cm}^{-3}$						
delay [ps]	A [$\text{cm}^2\text{V}^{-1}\text{s}^{-1}$]	ξ_A	τ_A [fs]	B [$\text{cm}^2\text{V}^{-1}\text{s}^{-1}$]	C [$10^{12} \text{ cm}^2\text{V}^{-1}$]	ξ_C
4.4	110	0.40	45	–	7000	0.8
200	83	0.29	45	–	4400	0.5

$N_{\text{exc}} = 1.3 \times 10^{18} \text{ photon.cm}^{-3}$						
delay [ps]	A [$\text{cm}^2\text{V}^{-1}\text{s}^{-1}$]	ξ_A	τ_A [fs]	B [$\text{cm}^2\text{V}^{-1}\text{s}^{-1}$]	C [$10^{12} \text{ cm}^2\text{V}^{-1}$]	ξ_C
5	140	0.31	73	–	8200	0.93
20	140	0.31	73	–	7600	0.86
200	150	0.33	73	–	5800	0.66

Table 6.4: Fit parameters for the yield-mobility spectra of the ZnO crystal measured at 120 K.

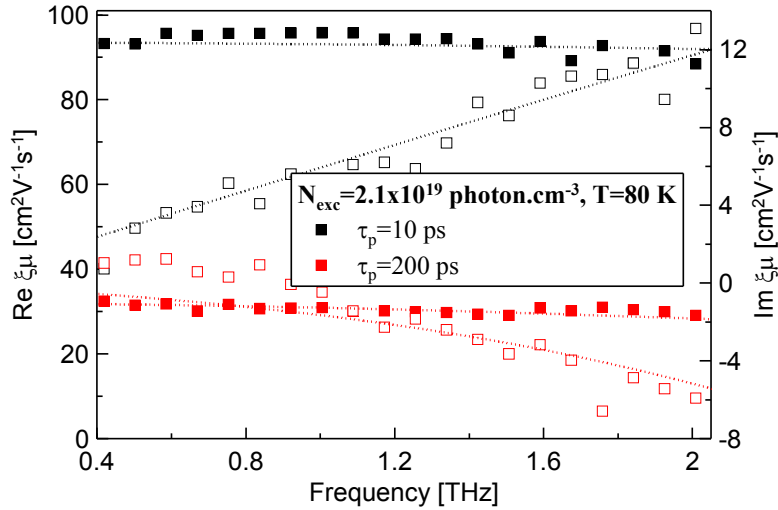


Figure 6.6: Spectra of the yield-mobility product measured with excitation density $2.1 \times 10^{19} \text{ photon.cm}^{-3}$, temperature 80 K. Spectra measured at pump-probe delays 10 ps and 200 ps are compared. Closed symbols show the real part of the yield-mobility product (left axis), the open symbols display the imaginary part (right axis). The dotted lines show the fits of the data by the equation 6.2.5.

are displayed in Tab. 6.4. The fit of the experimental data is slightly worse than at temperatures 20 and 80K but still acceptable. The evolution of the yield-mobility product is presented in Fig. 6.8. For excitation densities $(2 - 7) \times 10^{19} \text{ photon.cm}^{-3}$ only a system of free carriers with short carrier scattering time is created. At lower excitation intensities a mixture of free carriers and excitons with the oscillatory response is created several picoseconds after photoexcitation. The scattering time does not change during the next 200 picoseconds and it becomes longer with decreasing excitation density. The sum of the yield of free carriers and excitons is close to unity and in some cases it exceeds unity. The reason may be that the parameters of the mobility of the exciton may be somewhat different from those taken from Ref. 18. However, in our frequency range the response of excitons is so weak, that it is not possible to determine the resonance frequency and the damping parameter directly from the measured data. At the lowest excitation density $1.3 \times 10^{18} \text{ photon.cm}^{-3}$ the dynamics of the yield-mobility product is non-monotonic: after a short decrease, 10 ps after photoexcitation it increases slowly during the next 200 ps (see the pink curve in Fig. 6.8). In Tab. 6.4 it can be seen that the yield of free carriers ξ_A very slightly increases between pump-probe delays 20 ps to 200 ps, while the yield of excitons ξ_C decreases. Consequently, it may be possible that the dissociation of excitons causes the late increase of the conductivity.

At room temperature for high excitation densities it was found that the THz signal raises immediately after photoexcitation and remains constant for the next

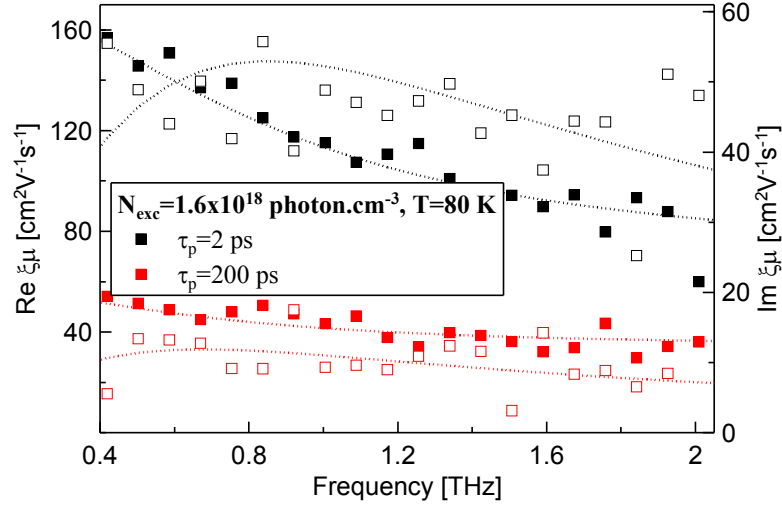


Figure 6.7: Spectra of the yield-mobility product measured with excitation density $1.6 \times 10^{18} \text{ photon.cm}^{-3}$, temperature 80 K. Spectra measured at pump-probe delays 2 ps and 200 ps are compared. Closed symbols show the real part of the yield-mobility product (left axis), the open symbols display the imaginary part (right axis). The dotted lines show the fits of the data by the equation 6.2.5.

200 picoseconds. The yield-mobility spectra were measured 10 ps after photoexcitation. It has been found for all excitation densities used that the spectra can be fitted by the Drude model. Assuming carrier effective mass equal to the electron effective mass in ZnO the quantum yield of the excitation process is equal to unity (see Fig. 6.9). Therefore the photoconductivity of ZnO is dominated by electrons and every absorbed photon creates an electron. The scattering time decreases with increasing excitation density (see Fig. 6.10).

6.2.1 Conclusion

We have examined the mobility of photogenerated carriers in bulk ZnO using time-resolved THz spectroscopy. It has been found that several types of response contribute to the carrier mobility:

- Free carriers with scattering time of several hundreds of fs. These carriers are formed only at temperatures lower than about 80 K and probably under condition of a low excitation density, i.e. in a deep part of the sample (deeper than the skin depth). This finding is consistent with the results published in Ref. 88.
- Dense electron-hole gas with Drude-like conductivity and short scattering time ($\lesssim 10$ fs). The formation and the dynamics of this system is similar to that reported in Ref. 18.

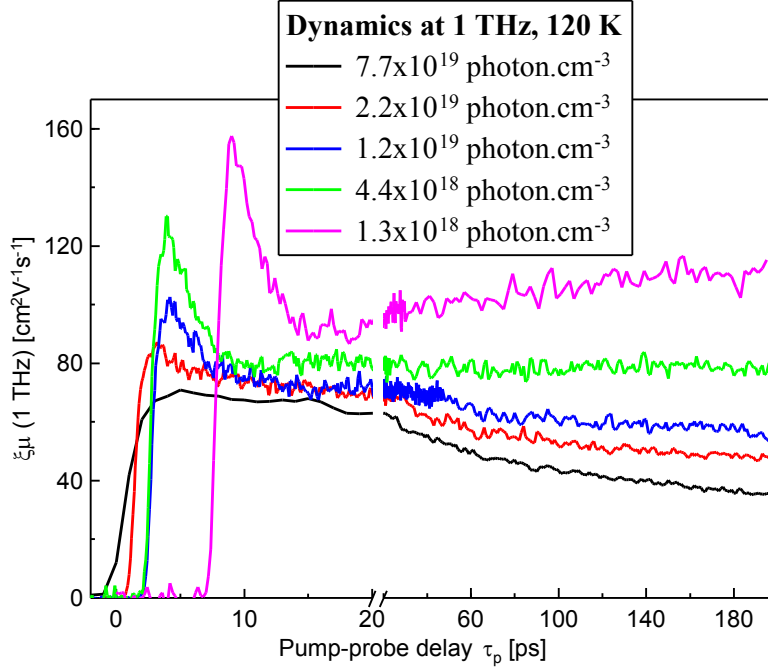


Figure 6.8: Dynamics of the carrier yield-mobility product at 1 THz, temperature 120 K. For clarity the time origin of the curves is shifted.

- Excitons with an oscillator response. The spectral shape of the mobility of these quasiparticles is similar to that reported in Ref. 18. However, unlike in Ref. 18, in our sample they are not observed at temperatures lower than 80 K. Their response may be hidden in the strong response of high-mobility free carriers, which dominate the mobility spectra at temperatures lower than 80 K.
- Free carriers with Drude-like response and scattering times in the range 10-100 fs dominate the photoconductivity of ZnO at temperatures higher than 80 K and carrier densities lower than $1 \times 10^{19} \text{ cm}^{-3}$.

From our results it has been found that the carrier dynamics, i.e. the formation of the above mentioned states, their recombination and their transformation from one species into another is crucially different at different excitation densities and in different regions of the sample. Due to the inhomogeneity of photoexcitation only a qualitative study could be carried out.

Our results agree to some degree with the findings of previous studies and in some points they disagree. From our comparison it is clear that the photocarrier response and dynamics differs substantially for different crystals. For a comprehensive study, one should systematically study samples elaborated by different methods and using simultaneously several experimental methods – for example to find out, how the density of defects and localized states influence the photocarrier

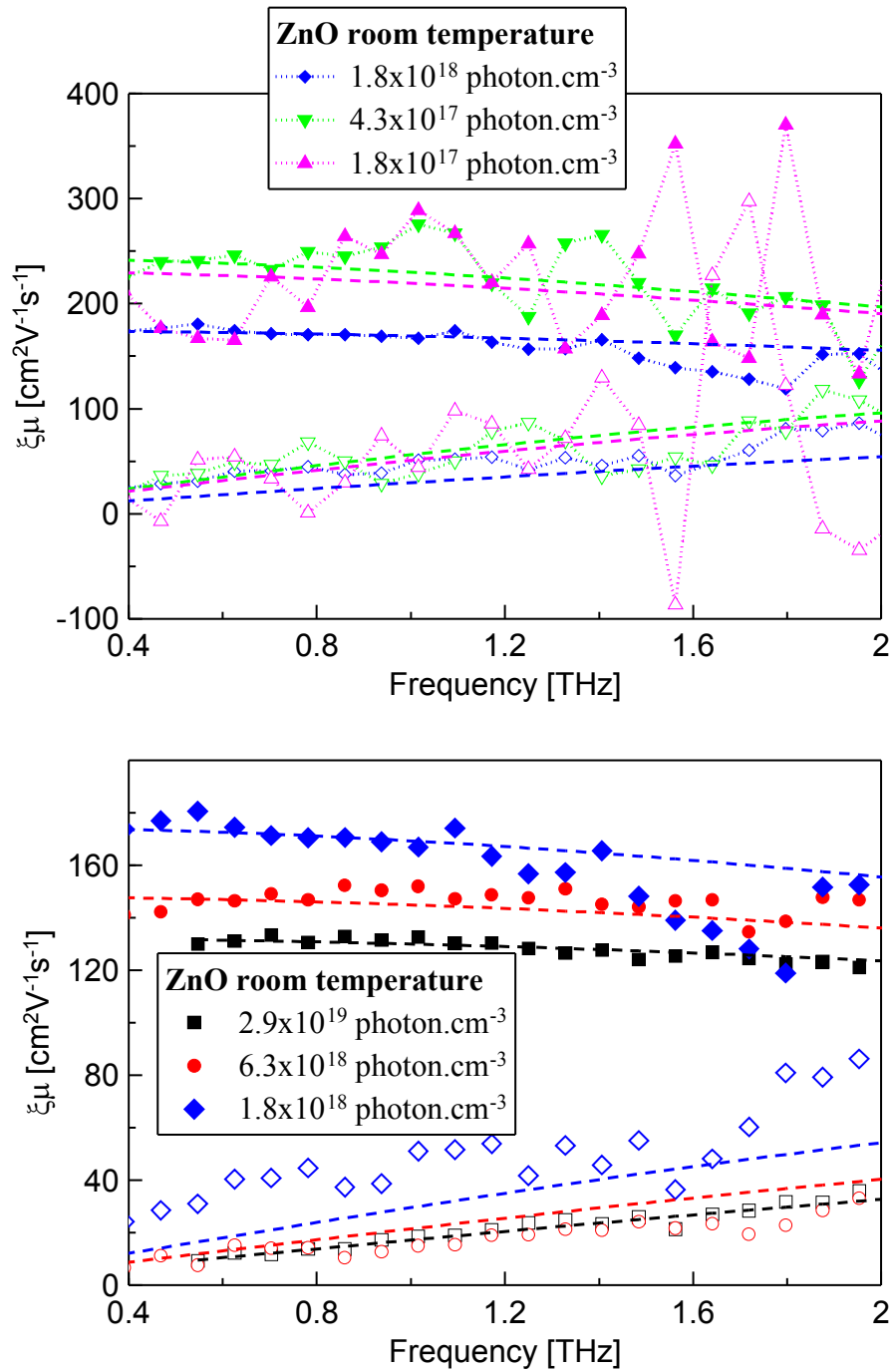


Figure 6.9: The spectra of electron mobility measured 10 ps after photoexcitation in bulk ZnO at room temperature. Closed symbols show the real part of the mobility, the open symbols display the imaginary part. The dashed lines show the fit of the data by the Drude model. For clarity the dataset is displayed in two separate graphs.

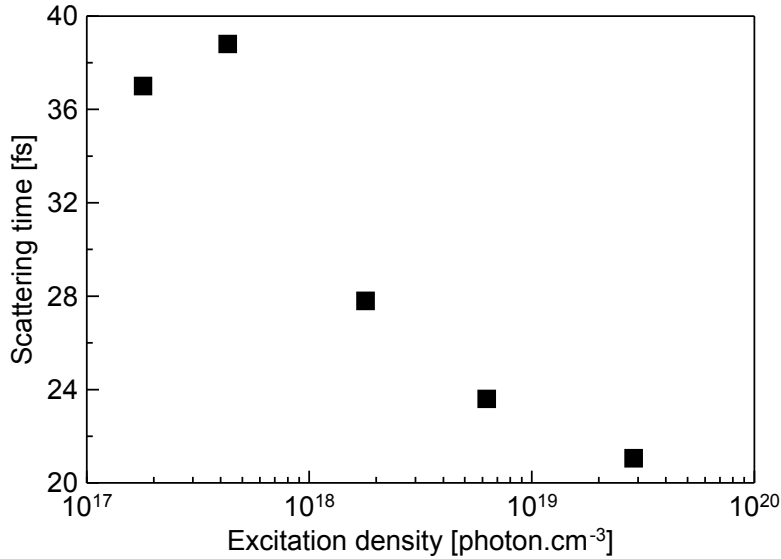


Figure 6.10: The scattering times extracted from the mobility spectra of ZnO at room temperature.

dynamics and response. Such a study is beyond the scope of this thesis. However, our results give an indication what kind of electron transport can be expected in nanocrystalline ZnO and may be valuable in combination with Monte-Carlo simulations of electron motion in ZnO nanocrystals.

6.3 Electron mobility and dynamics in nanocrystalline ZnO

We measured the photoconductivity of a nanocrystalline ZnO film deposited on sapphire at temperatures 20 and 293 K and at excitation densities $1 \times 10^{17} - 3 \times 10^{19}$ photon.cm⁻³. The nominal size of the nanocrystals was reported to be around 15 nm. The dynamics of the transient THz absorption was found to be similar to the one measured in Ref. 34: the yield-mobility product increases to its maximum value on a subpicosecond timescale and then it starts to decrease with a time constant larger than 200 picoseconds. The shape of the spectra of the yield-mobility product does not change with time. Here we present the spectra measured at 10 ps after photoexcitation. The spectra measured at room temperature are presented in Fig. 6.13, those measured at 20 K are displayed in Fig. 6.16.

The shape of the spectra changes with the excitation density. These changes are different for the two temperatures suggesting (in agreement with the discussion in Sec. 2.1) that they do not originate from the depolarization fields and that they cannot be accounted for by the effective medium theory. At room tempera-

ture the real part of the yield-mobility product changes only slightly. We deduce that the nanocrystals are percolated and the microscopic and macroscopic mobility are proportional to each other with a proportionality constant denoted as k_{EMA} .

To reveal the basic characteristics of the electron transport we compare the measured spectra with Monte-Carlo simulations of the electron motion, which were introduced in Subsec. 2.2.7. In our experiments the yield-mobility spectra are measured for two temperatures and several excitation densities. Both these parameters affect our simulations through the change of the kinetic energy of electrons:

- For very low excitation densities the conduction band electrons form a non-degenerated system of carriers and their velocity is thermal, i.e. determined by the lattice temperature.
- An increase of the photoexcitation density leads to a higher concentration of electrons in the conduction band. These electrons occupy conduction band states with higher energy due to the finite density of states at low energies. Consequently, their kinetic energy increases. For the highest used excitation densities (higher than 1×10^{19} photon.cm⁻³) the electron Fermi levels at 20 K and at room temperature do not differ much (see Fig. 6.11). In this case the electron gas is degenerated and only electrons with energy close to the Fermi level take part in the carrier transport. As a result, at high excitation densities the velocity of electrons contributing to the photoconductivity is the same at 20 K and at room temperature.

Experimentally, the yield-mobility spectra at the highest measured excitation densities ($\sim 3 \times 10^{19}$ photon.cm⁻³) are found to be temperature independent (see in Fig. 6.12). From this finding and from the considerations above it follows that simulation parameters – the quantum yield, the electron scattering time and the interaction parameters p_r , p_s – are similar for both 20 K and for room temperature.

The electron mobility is expected to vary upon variation of the excitation density as this is closely connected to the value of the average electron velocity. If this average velocity is low, the ballistic motion of electrons is slow and they do not interact often with the boundaries of the nanocrystals. Upon an increase of their kinetic energy electrons move faster and interact with the nanocrystal boundaries more often, therefore they feel a stronger localization and their response function reflects these changes.

At room temperature the average electron velocity decreases from 3.5×10^5 m/s (at the highest electron density of $\sim 3 \times 10^{19}$ cm⁻³ shown in 6.11) only to 2.2×10^5 m/s (for the lowest electron density of $\sim 3 \times 10^{17}$ cm⁻³). In contrast, at 20 K, the velocity decreases much more: from 3.5×10^5 m/s (for electron density 3×10^{19} cm⁻³) down to 0.57×10^5 m/s (for electron density $\sim 1.4 \times 10^{17}$ cm⁻³).

At both temperatures the upper bound of the velocity is given by the Fermi velocity at high electron densities; the minimal value of electron velocity at low electron densities is determined from the electron thermal velocity. Consequently, the variation of the excitation density has a much higher impact on the electron mobility spectra at 20 K than on those at 293 K (see Figures 6.13 and 6.16).

At room temperature the real part of the yield-mobility spectra is almost identical for all excitation densities (Fig. 6.13; a small change occurs probably only for the lowest excitation density of $\sim 3 \times 10^{17}$ photon.cm $^{-3}$; however, those data display a rather higher noise). The imaginary part can be characterized by a linear dependence with a negative slope. This negative slope was found to be incompatible with our simulations and we attribute it to the presence of excitons. Due to their large binding energy in ZnO, excitons can be present in ZnO even at room temperature. We assume that their response in nanocrystals is similar to the exciton response observed in bulk ZnO: oscillatory behaviour with circular frequency of $\omega_0 = 50$ rad.ps $^{-1}$ and damping frequency $\gamma = 6$ ps $^{-1}$. [18] In this case, their mobility in the THz frequency range is almost completely imaginary and the imaginary part can be characterized by a linear function with negative slope. The imaginary part clearly decreases with decreasing excitation density (see Fig. 6.13). We can then deduce that the relative population of the exciton states is the highest at low excitation densities; with the increase of the excitation density their contribution vanishes and mobile electrons dominate the mobility.

In our model we assume that each photon generates an electron-hole pair and the carriers then either become mobile or form excitons. The equation used to describe the observed yield-mobility spectra then reads:

$$(\xi\mu)_{meas}(\omega) = k_{EMA} \left(\xi_{mobile}\mu_{micro}(\omega) + (1 - \xi_{mobile}) \frac{-i\omega C_0}{\omega_0^2 - \omega^2 - i\gamma\omega} \right) \quad (6.3.1)$$

where k_{EMA} is the ratio of the microscopic and macroscopic mobility in the sample (effective medium approximation – see Eq. 2.1.18), ξ_{mobile} is the quantum yield of mobile electrons, C_0 represents the oscillator strength of an exciton and $\mu_{micro}(\omega)$ is the mobility spectrum of a mobile electron obtained by Monte-Carlo simulations. The model fits the data well (see Fig. 6.13). Our simulations are compatible with the measured data for $p_r = 0.75$, $p_s = 0.25$ and nanocrystal diameter 12 nm. From the fit of the measured data the value of the oscillator strength $C_0 = 2.8 \times 10^{16}$ cm 2 V $^{-1}$ is obtained. It is four times larger than the value expected from the equation 2.2.4 ($q/m_{eff} = 6.3 \times 10^{15}$ cm 2 V $^{-1}$). However, it has been shown that exciton polarizability may increase due to the confinement in nanocrystals. [90] The ratio of the macroscopic and microscopic mobility k_{EMA} was found to be 0.47, which is close to the value 0.54 calculated from the equation 2.1.17 under the assumption that the nanocrystals are aligned as random closely packed spheres (the volume fraction of the void matrix is in this case $s = 0.36$; for spheres $K = 2$). The extracted yield ξ_{mobile} clearly increases with increasing excitation density (see Fig. 6.14) This behaviour is common also in bulk semicon-

ductors around the Mott density. The scattering time used for the simulations is 7 fs for all excitation densities. This value is lower than the one measured in bulk ZnO, probably due to the enhanced electron-hole interaction observed also through the enhancement of the exciton oscillator strength. The scattering time is then expected to increase with decreasing excitation density. Apparently the effect of this increase on the measured spectra is too low to be observed; it may be due to the decreasing quantum yield ξ_{mobile} with decreasing excitation density.

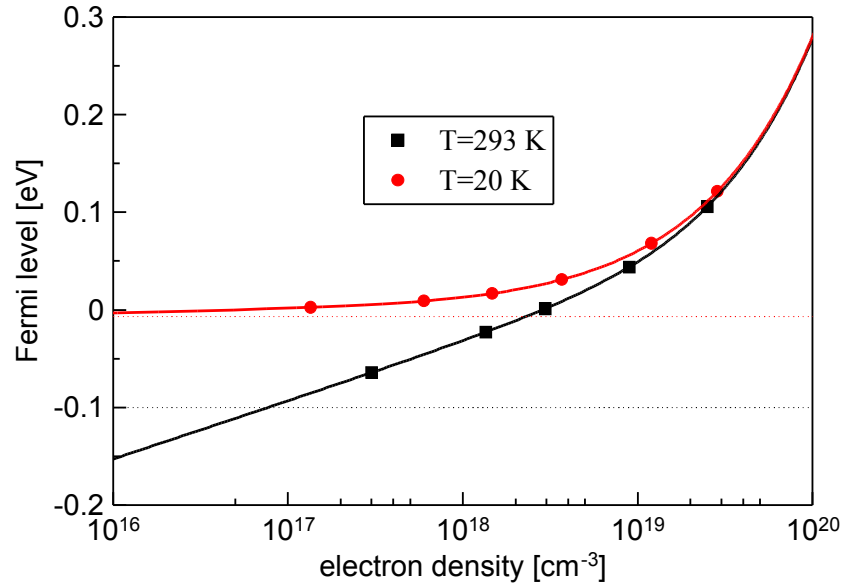


Figure 6.11: Fermi level of an electron gas system in ZnO. The dotted lines display the energy thresholds for Boltzmann distribution ($\approx -4k_B T$). The symbols correspond to the electron density generated in our experiments under the assumption that the quantum yield of the photoexcitation is unity.

At 20 K the imaginary part of the yield-mobility product does not change substantially; the large change of the imaginary part between the spectra corresponding to the two lowest pump intensities should be attributed to the noise due to the low measured signal (photoconductivity) (see Fig. 6.16). The photoinduced mobility is then attributed only to mobile electrons and the corresponding model is expressed by the equation:

$$(\xi\mu)_{meas}(\omega) = k_{EMA} \xi_{mobile} \mu_{micro}(\omega) \quad (6.3.2)$$

The model fits the data well, except for minor disagreements in the imaginary part of the yield-mobility product for excitation densities higher than $\sim 3 \times 10^{18}$ photon.cm⁻³ (see Fig. 6.16, upper panel). The interaction parameters were found to be the same as at room temperature, i.e. $p_r = 0.75$ and $p_s = 0.25$. The ratio of the macroscopic and microscopic mobility k_{EMA} is 0.47, i.e. the same as at room temperature. The yield is set to unity for each spectrum. For excitation

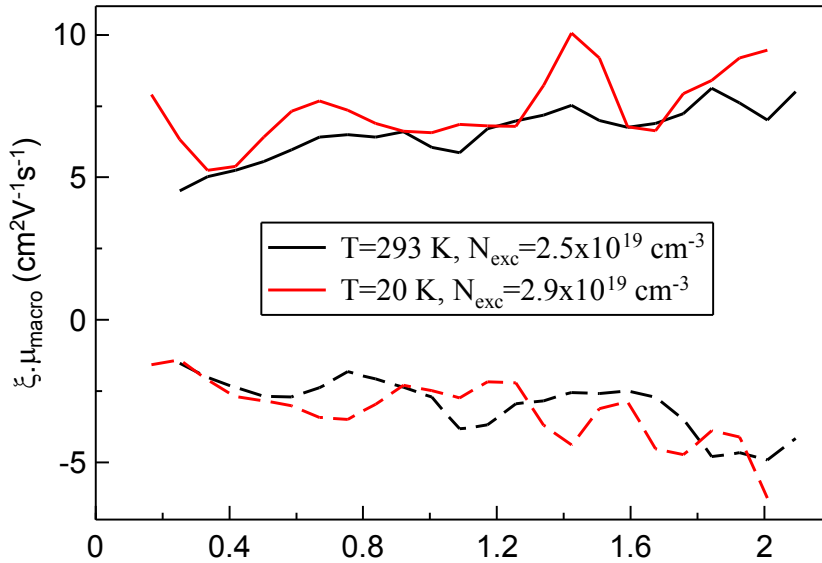


Figure 6.12: Comparison of spectra of the yield-mobility product measured at high excitation densities ($\approx 2.5 \times 10^{19}$ photon. cm^{-3}) at room temperature and at 20K.

densities lower than $\sim 3 \times 10^{18}$ photon. cm^{-3} the real part of the mobility was found to increase considerably with decreasing excitation density. This observation can be explained by an increase of the scattering time. The scattering times used in our simulations are displayed in Fig. 6.15. At excitation densities higher than $\sim 3 \times 10^{18}$ photon. cm^{-3} it was found to be about 7 fs, which is in agreement with the scattering time observed at room temperature. For the lowest excitation density the electron scattering time reaches 100 fs. Due to an increased noise in the spectra the uncertainty of this value is about 20%. The considerable change of the scattering time may again be explained by the strong electron-hole interaction in nanocrystalline ZnO at high carrier densities which was observed already at room temperature.

6.3.1 Conclusion

We have examined the mobility of photogenerated carriers in nanocrystalline ZnO using time-resolved THz spectroscopy. Measurements were carried out at room temperature and 20K. It has been shown that classical Monte-Carlo simulations may be used to model the electron transport for substantially different temperatures and for a wide range of carrier densities.

Several findings suggest an increased electron-hole interaction in nanocrystalline ZnO:

- At room temperature oscillatory carrier response was observed. This response was attributed to excitons. The oscillator strength was determined

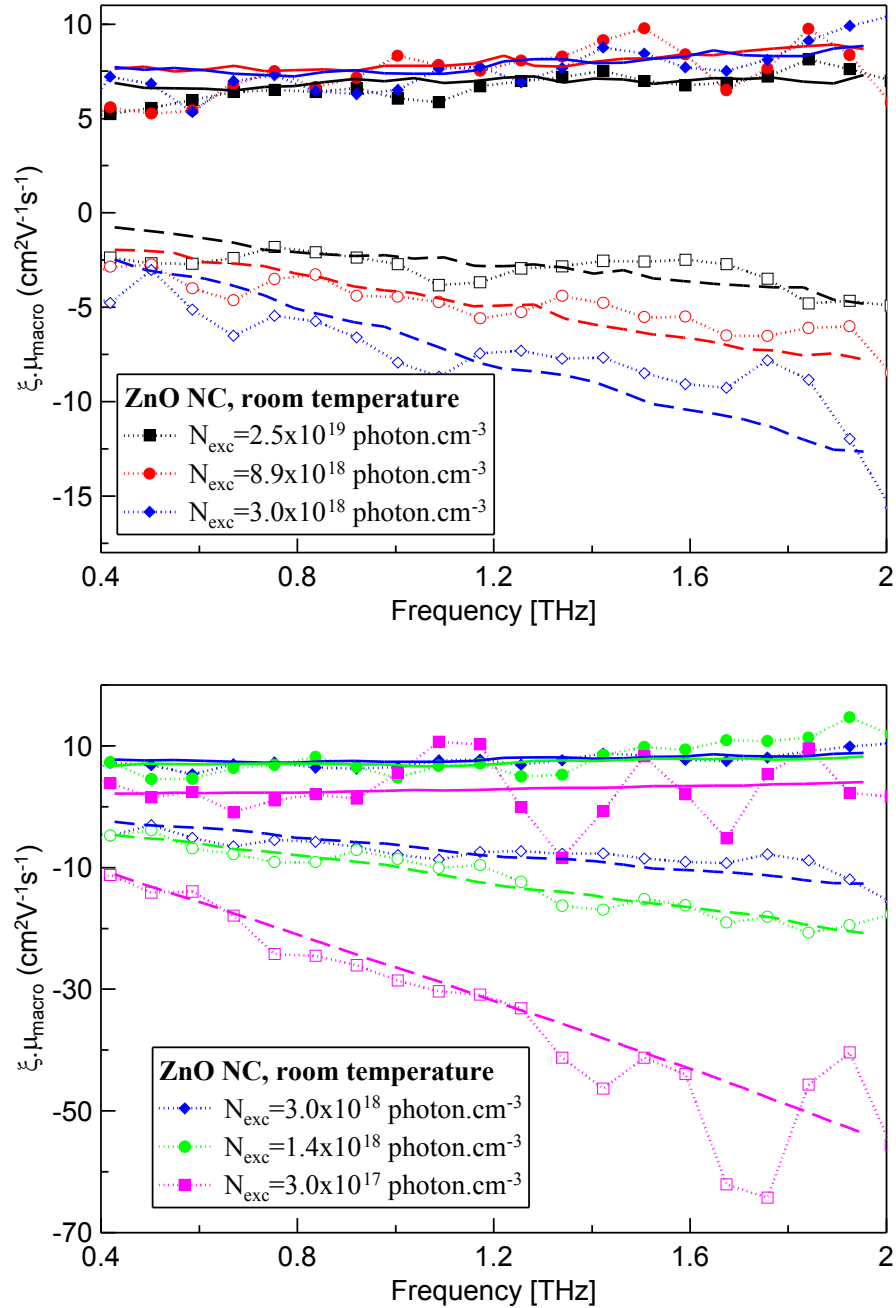


Figure 6.13: Measured spectra of yield-mobility product of nanocrystalline ZnO at room temperature. Closed symbols show the real part of the mobility, the open symbols display the imaginary part. The solid and dashed lines show the fit of the data by the equation 6.3.1. For clarity the dataset is displayed in two separate graphs.

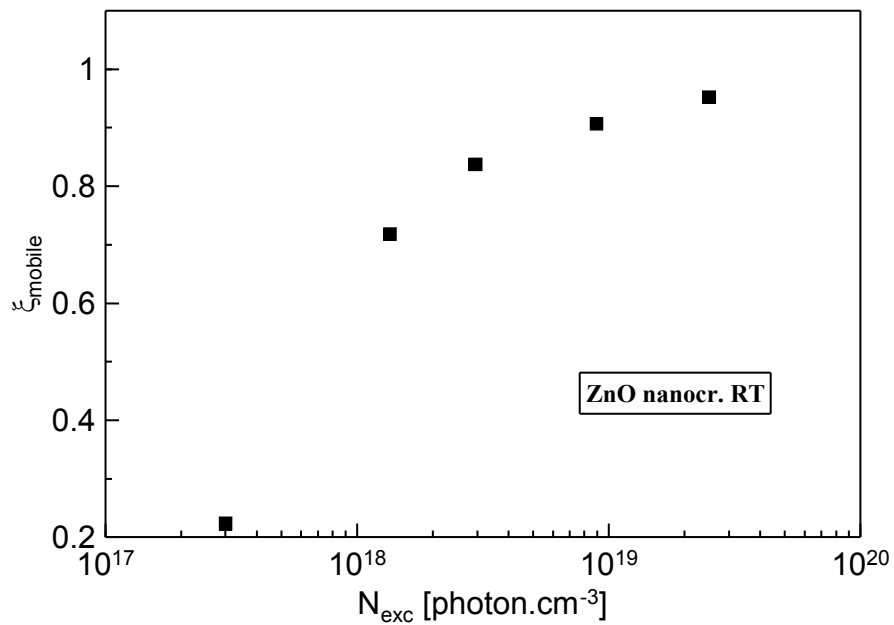


Figure 6.14: The yield of mobile electrons at room temperature.

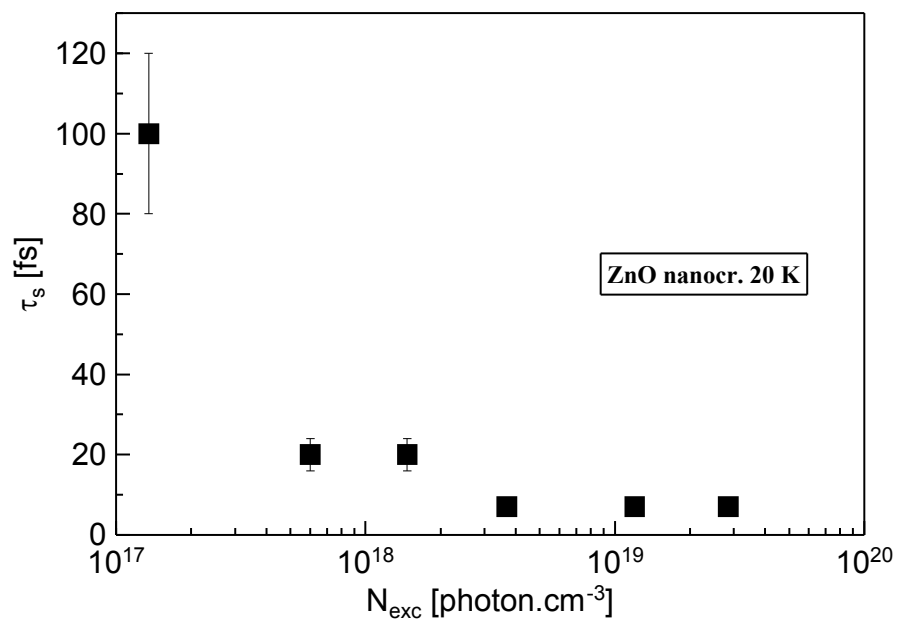


Figure 6.15: The electron scattering time at 20 K.

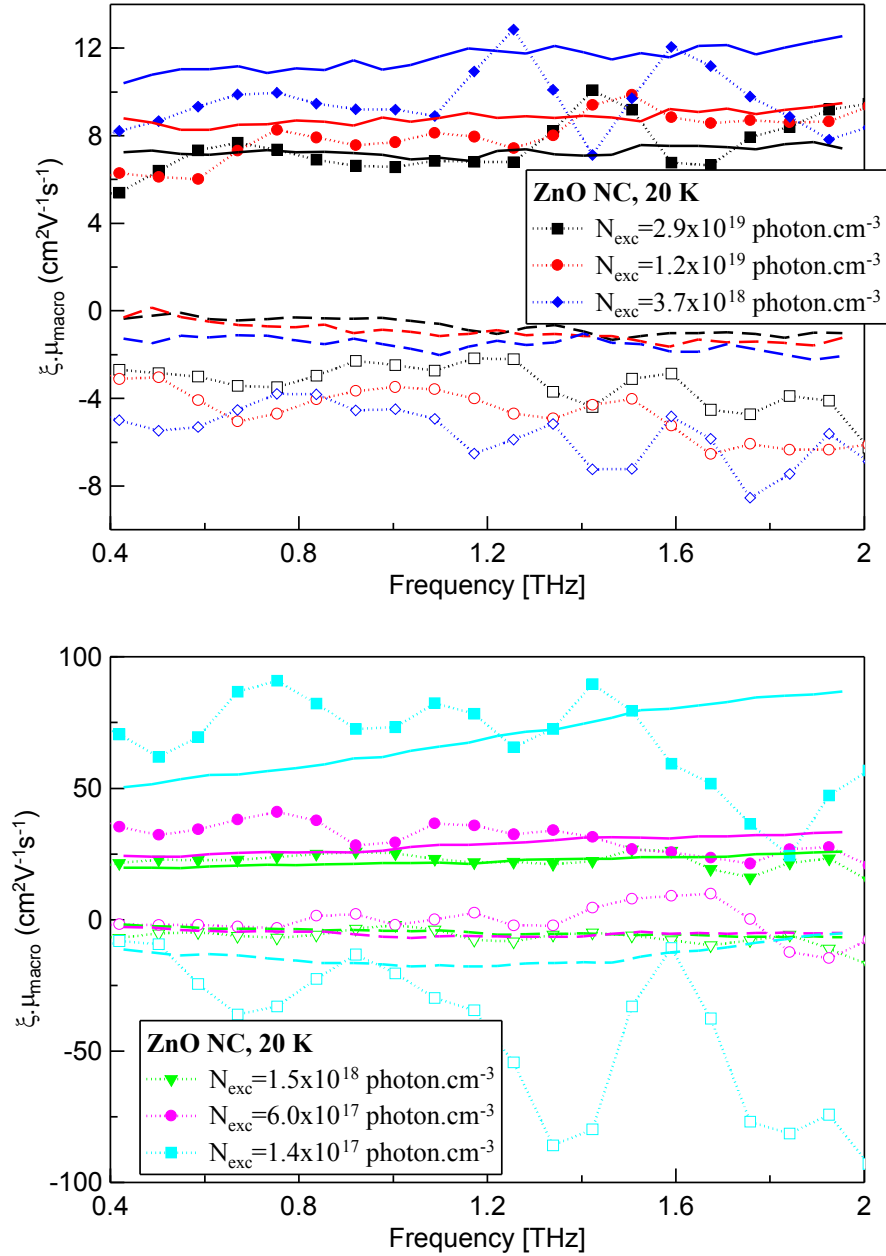


Figure 6.16: Measured spectra of yield-mobility product of nanocrystalline ZnO at 20 K. Closed symbols show the real part of the mobility, the open symbols display the imaginary part. The solid and dashed lines show the fit of the data by Monte-Carlo simulations. For clarity the dataset is displayed in two separate graphs.

to be higher than in bulk ZnO. Moreover, in bulk ZnO no exciton response was observed at room temperature.

- It has been found that the scattering time changes substantially with carrier density at 20 K. It is interesting that no excitons were observed at 20 K and it is in agreement with our findings in bulk ZnO.

6.4 Challenges and outlook for the study of carrier transport in ZnO

Very rich dynamical properties were measured both in bulk and in nanocrystalline ZnO. Our models describe quantitatively or semi-quantitatively many of the observed features. However, not all questions have been completely clarified: the origin of some surprising phenomena remains to be elucidated.

One of them is the reason of the coexistence of high density plasma with a very short scattering time and a less dense plasma with a quite long scattering time. We interpreted this phenomenon as to be due to the depth profile of the carrier density: the response of carriers in deeper areas of the sample, where their density is low, is strongly enhanced by their very long scattering time.

Another surprising feature observed both in bulk and in nanocrystalline samples is the absence of excitons in the spectra namely at 20 K. In nanocrystalline ZnO excitons were detected at room temperature. In contrast, in the bulk ZnO, excitons were observed at 80 and 120 K (and not at room temperature).

To probe the carrier transport exclusively in the high-density regime, the carrier density must be homogeneous in the sample. This may be accomplished by probing bulk ZnO in the form of a ~ 40 nm thin film. To assess the contribution of the holes to the total photoconductivity, samples oriented both parallel and perpendicular to the crystalline c -axis have to be studied.

For nanocrystalline ZnO, the mobility of electrons at low excitation densities should be more thoroughly studied with an experimental setup enabling a higher signal-to-noise ratio. The investigation should be also focused on nanocrystals without dye sensitization to exclude the possibility of interaction of charge carriers with the dye.

Chapter 7

Electron transport in nanocrystalline CdS

CdS is a II-VI semiconductor with direct bandgap. Its fundamental properties are summarized in Tab. 7.1. It has been shown that it is possible to fabricate CdS nanocrystals easily and cheaply by Chemical Bath Deposition (CBD). [91,92] This material was found to be useful in new generation Cu(In, Ga)Se₂ solar cells as a buffer layer between the active material and the transparent conductive oxide. [91] That is why it is important to study the carrier transport in nanocrystalline CdS prepared by CBD.

The CdS nanocrystals were deposited at 90 °C on a fused silica substrate by ammonia-free CBD. [92] The samples were provided by P. Němec from the Faculty of Mathematics and Physics, Charles University in Prague. The thickness of the film was around 1.3 μm. The diameter of the as-prepared nanocrystals was around 6.2 nm. The prepared film was then annealed for 45 min, which resulted in a growth of nanocrystals. By using different temperatures of annealing, nanocrystalline films with different nanocrystal size were obtained. The diameter of nanocrystals ranged from 6.2 nm (as-prepared nanocrystals) to 14.2 nm (see

Crystal structure [93]	hexagonal
Bandgap (300 K) [93]	2.5 eV
Bohr radius of exciton	~ 3 nm
electron effective mass [94]	0.2 m _e
light hole eff. mass [95]	0.7 m _e
heavy hole eff. mass [95]	5 m _e
refraction index at 1 THz (our measurements)	2.9
refraction index at 400 nm [93]	2.6 + i0.45
electron scattering time [96]	35 fs
DC mobility μ_{bulk}	~ 300 cm ² V ⁻¹ s ⁻¹

Table 7.1: Some important properties of bulk CdS

annealing temperature [°C]	–	400	500	550	600
nanocrystal diameter d [nm]	6.2	10.4	12.2	13.8	14.2

Table 7.2: Samples investigated in our study

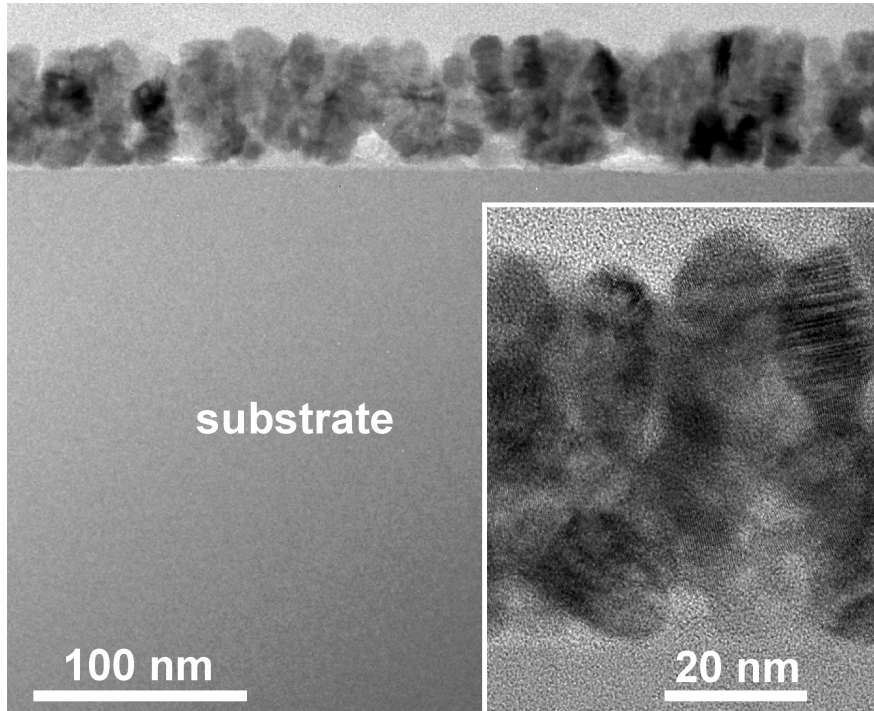


Figure 7.1: Transmission electron microscopy image of the cross section of a nanocrystalline CdS film prepared similarly as those investigated in our study.

Tab. 7.2). The porosity of the film can be seen from the transmission electron microscopy image (TEM) of the cross section of a film prepared similarly as those in our experiments (see Fig. 7.1). The image was made by Petr Formánek from the Institut für Strukturphysik, Technische Universität Dresden. From Fig. 7.1 it can be seen that the nanocrystals form clusters.

The carrier transport in nanocrystalline CdS films was probed at room temperature by time-resolved THz spectroscopy. In the majority of experiments the wavelength of the excitation beam was set to 400 nm, which generates mobile carriers in the nanocrystalline film through one-photon absorption. In the experiments we tuned the excitation density in the range of $6 \times 10^{17} - 2 \times 10^{20}$ photon.cm⁻³. It has been found that the shape of the spectra of the yield-mobility product does not change significantly with the pump-probe delay. In this case we can simplify our analysis; we present two kinds of experimental data:

- Spectra of the yield-mobility product 10 ps after photoexcitation.
- Time evolution of the yield-mobility product at 1 THz.

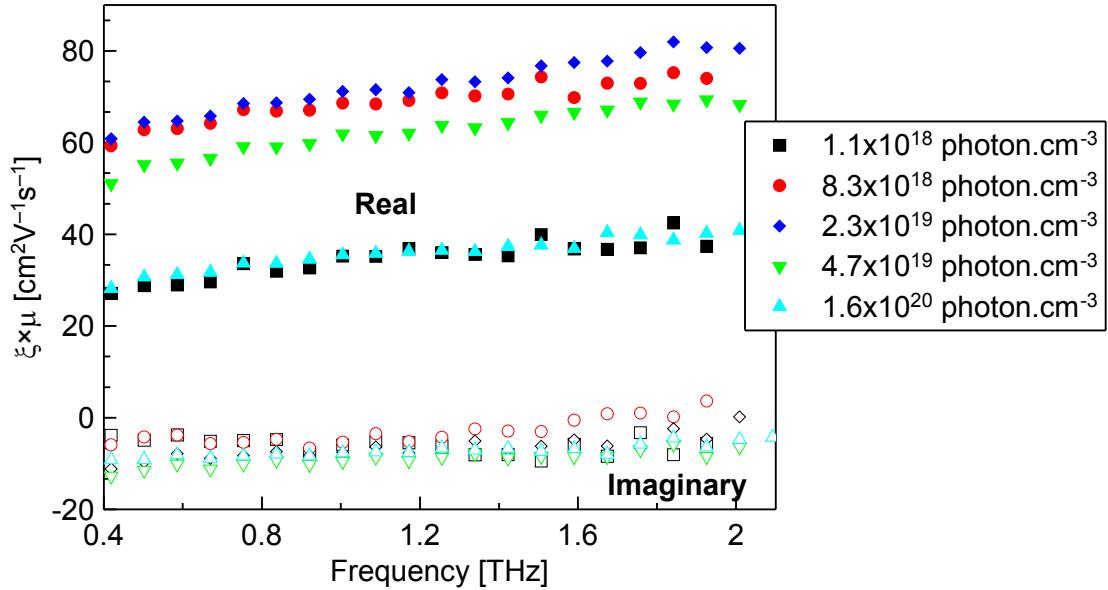


Figure 7.2: Measured spectra of the yield-mobility product for nanocrystalline CdS with nanocrystal size 10.4 nm.

7.1 Spectral response of carriers

The yield-mobility spectra for nanocrystals with diameter 10.4 nm are displayed in Fig. 7.2. The shape of the spectra is similar for all the other samples. From the measured data it is clear that the shape of the yield mobility product does not change significantly with the excitation density over a wide range of carrier densities. Moreover, the observed yield-mobility product in some cases reaches $80 \text{ cm}^2\text{V}^{-1}\text{s}^{-1}$, i.e. it exceeds 25% of the DC mobility in the bulk. Analyzing the experimental data in the light of the discussion in Subsection 2.1.1, we conclude that the change of the mobility with the excitation density originates from a change of the microscopic mobility in CdS nanocrystals, not from the depolarization fields. This picture is corroborated also by the transmission electron microscopy image in Fig. 7.1, where it is shown that the nanocrystals touch each other. To sum up, the nanocrystals are percolated and the depolarization fields do not modify the shape of the mobility spectra. The microscopic and macroscopic mobility are then proportional to each other with a proportionality constant denoted as k_{EMA} (see Eq. 2.1.18).

The effective mass of electrons in CdS is much lower than the effective mass of holes (see Tab. 7.1), therefore we assume that electrons dominate the mobility spectra and the mobility of holes can be neglected. Although the electron mobility is high, the real part of the mobility is clearly increasing and its imaginary part is negative, therefore the nanocrystal boundaries do confine the charge carriers. At first we show that our simulations with a single localization length scale (i.e. with similar structures as those discussed in Subsection 2.2.7) cannot explain our

data. In such simulations the real part of the mobility reaches its maximum at $f_{max} \approx 1.1 \times v_{therm} / (2d)$, i.e. close to the round-trip frequency in the nanocrystals. Above this frequency the diffusion length of carriers during one period of the driving electromagnetic radiation is smaller than the size of the nanocrystal and the electrons do not feel localization. On the other hand, below this frequency the electrons interact with nanocrystal boundaries and the real part of the mobility increases with the frequency. [5] For our samples the calculated value of f_{max} lies in the range of 6 – 13 THz. This is in disagreement with our measured spectra, where one expects a wide maximum of the mobility around 2 THz.

Let us estimate the second length scale which may account for the measured yield-mobility spectra. It has been shown that the ac mobility spectra of an electron inside a potential well with perfectly reflecting walls can be reasonably approximated by a Debye relaxation (see subsection 2.2.3) [20, 21]:

$$\mu_{ac}(\omega) = \mu_{bulk} \frac{1}{1 - i\pi^2 \frac{\mu_{bulk} k_B T}{L^2 \omega e_0}} \quad (7.1.1)$$

where L is the size of the box, T is the temperature, k_B is the Boltzmann constant and μ_{bulk} is the mobility of the electron inside the box (mobility in bulk CdS). The real part of this function is concave only for

$$\omega > \frac{\pi^2 k_B T \mu_{bulk}}{\sqrt{3} L^2 e_0} \quad (7.1.2)$$

and, comparing to our spectra which are concave above $\omega_{low} \approx 2\pi \times 0.4$ THz, we deduce that

$$L \geq \sqrt{\frac{k_B T \mu_{bulk} \pi^2}{\sqrt{3} \omega_{low} e_0}} \approx 40 \text{ nm} \quad (7.1.3)$$

We attribute this second length scale to clusters of nanocrystals, i.e. we assume that nanocrystals are aggregated into mutually separated clusters. This picture of the CdS film morphology, deduced from the measured spectra of the yield-mobility product, is in perfect agreement with the film morphology shown in Fig. 7.1.

Fortunately, our simulations are flexible enough, so that we take into account the second localization scale (i.e. clusters of nanocrystals). In our model we use the simplest possible geometrical distribution of nanocrystals in the clusters. Clusters are represented by cubes divided into smaller cubes representing the nanocrystals (see Fig. 7.3). The volume of the small cubes is the same as that of nanocrystals $V = \pi d^3 / 6$. The number of nanocrystals in a cluster is N^3 , where N is an integer. The interactions of carriers with nanocrystals and clusters are described by different parameter sets:

- p_{ER}, p_{ES}, p_{ET} (probability of reflection, scattering, tunnelling, respectively) characterizing interaction with nanocrystal boundaries; $p_{ER} + p_{ES} + p_{ET} = 1$.

Alternatively, we introduce the probability of blocking of carriers (i.e. the electron stays in the same nanocrystal after collision) $p_{EB} = p_{ER} + 1/2p_{ES}$ and the probability of transition into another nanocrystal $p_{EF} = p_{ET} + 1/2p_{ES}$.

- p_R, p_S, p_T (probability of reflection, scattering, tunnelling, respectively) for interaction characterizing cluster boundaries; $p_R + p_S + p_T = 1$. Alternatively, we introduce the probability of blocking of carriers (i.e. the electron stays in the same cluster after collision) $p_B = p_R + 1/2p_S$ and the probability of transition into another cluster $p_F = p_T + 1/2p_S$.

A detailed discussion on the two alternative representation of interaction probabilities can be found on page 26.

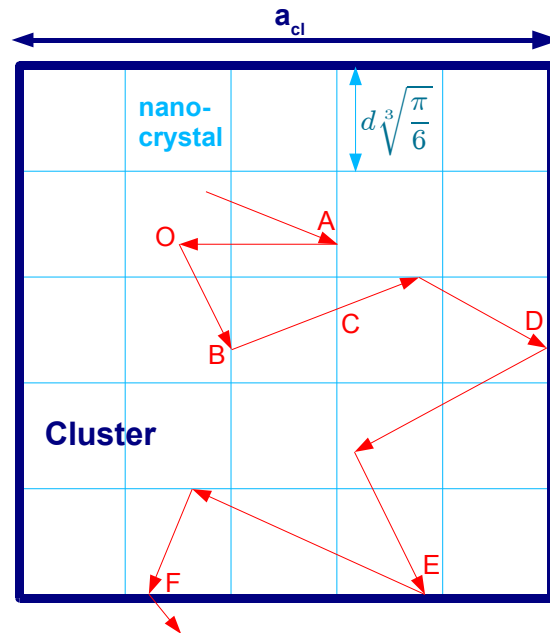


Figure 7.3: Representation of a CdS cluster in our simulations of electron motion. The nanocrystals are modeled as smaller cubes filling the cluster. An electron can be scattered in the bulk (**O**), reflected (**A**, with probability p_{ER}) or scattered (**B**, with probability p_{ES}) on nanocrystal boundaries or it can pass through nanocrystal boundaries without change of velocity (**C**, with probability p_{ET}). In addition it can be reflected (**D**, **E**, with probability p_R) or scattered (**F**, with probability p_S) on a cluster.

Some examples of the mobility spectra calculated by simulation of electron motion in clusters of nanocrystals are displayed in Fig. 7.4. It can be seen that by considering clusters with a large size in our simulations, the maximum of the mobility is shifted to lower frequencies. Weak interaction of electrons with nanocrystal boundaries and their strong interaction with cluster boundaries then result in a mobility spectra similar to those obtained in our measurements.

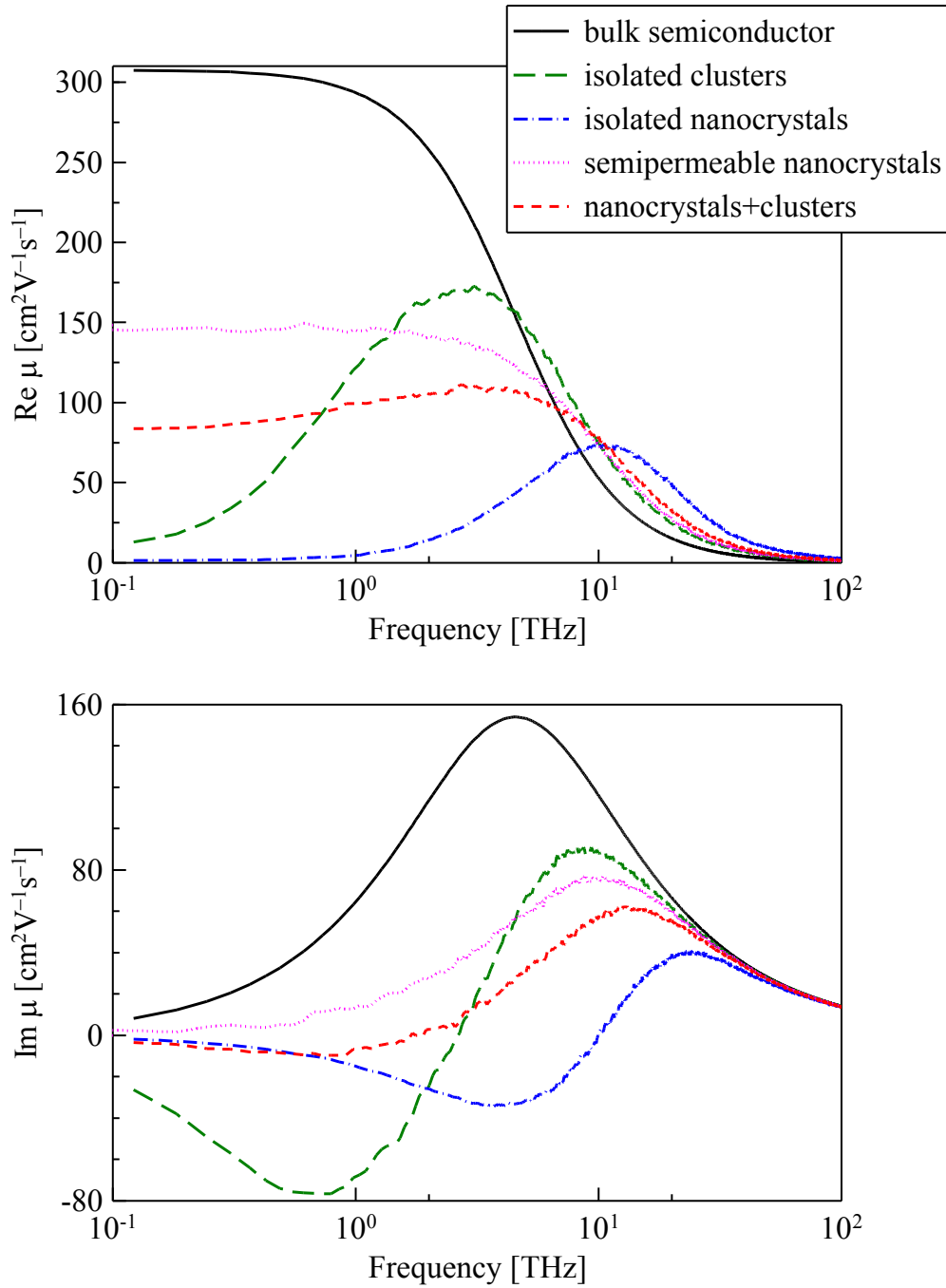


Figure 7.4: Comparison of simulated mobility spectra for bulk semiconductor ($p_B = 0$, $p_{EB} = 0$), isolated clusters ($p_B = 1$, $p_{EB} = 0$), isolated nanocrystals ($p_{EB} = 1$), semipermeable nanocrystals ($p_B = 0$, $p_{EB} = 0.66$) and clusters in combination with nanocrystals (2 localization length scales: $p_B = 0.9$, $p_{EB} = 0.66$). The size of nanocrystals is $d = 10.4$ nm, the size of clusters $a_{cl} = 33.5$ nm.

Although the basic shape of the yield-mobility spectra for various samples look similar to each other, it is interesting to follow the dependence of the yield-mobility product with the excitation density. For each sample the yield-mobility spectra measured below 1×10^{18} photon.cm $^{-3}$ do not depend on the excitation density. For example, for samples with nanocrystal sizes 5.8, 13.8 and 14.2 nm it can be seen that the spectra measured at excitation densities 5×10^{17} photon.cm $^{-3}$ and 10^{18} photon.cm $^{-3}$ are identical (see Figures 7.5, 7.8 and 7.9). The level of the real part of the yield-mobility product increases as the excitation density increases from 10^{18} to 10^{19} photon.cm $^{-3}$. We first focus on this part of the data, which can be modeled by Boltzmann statistics with a sufficient precision. The regime of decreasing mobility at higher excitation densities requires the implementation of Fermi-Dirac statistics and will be presented later in Sec. 7.3.

The yield-mobility spectra can be calculated under the assumption that the quantum yield of the excitation process does not depend on the excitation density. We apply Eq. 2.1.18 to relate the observed (macroscopic) response of the sample $(\xi\mu)_{meas}(\omega)$ and the calculated mobility μ_{micro} :

$$(\xi\mu)_{meas}(\omega) = k_{EMA} \xi_{mobile} \mu_{micro}(\omega) \quad (7.1.4)$$

where k_{EMA} is the ratio of the microscopic and macroscopic mobility in the sample (given by the effective medium approximation), ξ_{mobile} is the quantum yield of mobile electrons and $\mu_{micro}(\omega)$ is the mobility spectrum of a mobile electron obtained by Monte-Carlo simulations.

From the equation 7.1.4 it follows that one cannot determine the quantum yield ξ_{mobile} and k_{EMA} independently, only their product is evaluated. Its value has been found in the interval 0.4-0.7 for all the samples. As k_{EMA} is ~ 0.54 for a sample composed of randomly touching spheres (which resembles the structure of our samples) the quantum yield should be close to unity.

The measured spectra and the models are compared in Figures 7.5, 7.6, 7.7, 7.8 and 7.9. We calculated a series of spectra with different parameters of electron motion and selected those sets which matched the experimental data. By this method the appropriate set of parameters was found for each measured spectrum. The obtained size of the clusters is displayed in Fig. 7.10. We did not observe any significant dependence of the cluster size on the size of nanocrystals (i.e. on the temperature of annealing). This may be due to the recrystallization of the material with annealing; as the nanocrystals grow, their number in a single cluster is reduced. The probabilities of blocking of electron transport among nanocrystals p_{EB} and among clusters p_B are displayed in Fig. 7.11.

From the obtained probabilities of electron interaction with cluster and nanocrystal boundaries it is clear that the increase of the electron mobility with the excitation density is due to the reduction of the electron confinement (see Fig. 7.11). The extent of this reduction is much lower for clusters than for nanocrystals. For example, for the sample with nanocrystal size 10.4 nm the value of p_B characterizing the confinement in clusters changes from 0.94 (for $N_{exc} =$

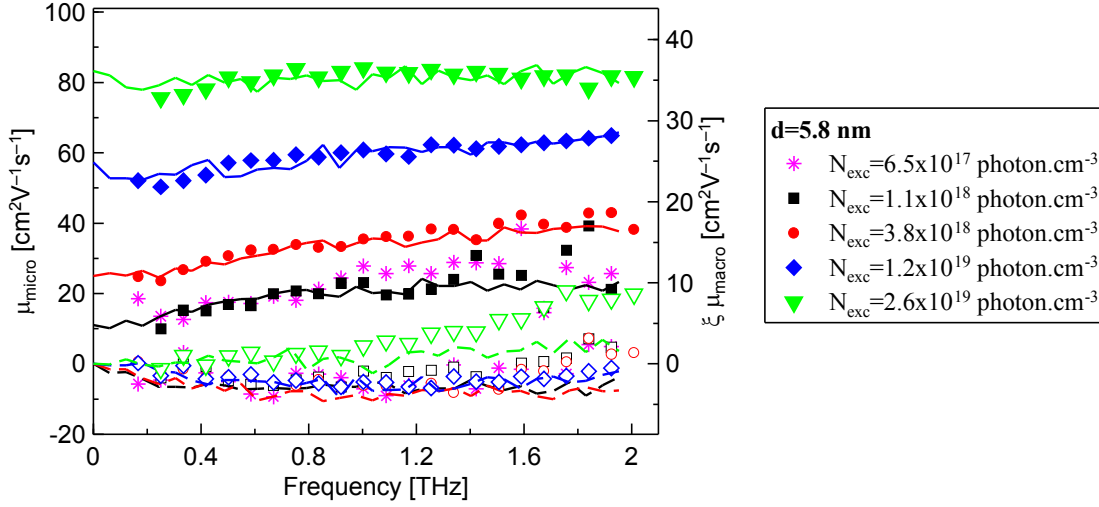


Figure 7.5: Measured yield-mobility spectra for nanocrystalline CdS with nanocrystal size 5.8 nm. The symbols represent the measured data (closed- real part, open symbols imaginary part) and the lines show the mobility spectra from Monte-Carlo simulations assuming Boltzmann statistics. The left axis shows the microscopic mobility, the right axis displays the measured yield-mobility product.

$1.1 \times 10^{18} \text{ photon.cm}^{-3}$) to 0.8 (for $N_{\text{exc}} = 8.3 \times 10^{18} \text{ photon.cm}^{-3}$), while p_{EB} (characterizing the confinement in nanocrystals) decreases from 0.66 to 0.33 (see Fig. 7.11). It is probably due to the fact that the electron confinement in clusters may be caused mainly by the geometry of clusters (i.e. separation of clusters in space by air voids), which is not changed by the pump fluence. On the other hand, the electron confinement due to nanocrystal boundaries clearly depends on the density of carriers. We have found that the investigation of the dynamics of electron mobility is crucial for the explanation of the origin of this phenomenon.

7.2 Ultrafast electron dynamics

The measured dynamics of the yield-mobility product for the sample with the nanocrystal size 10.4 nm is displayed in Fig. 7.12. All the other samples exhibit a very similar behaviour:

- At low excitation densities ($\leq 10^{19} \text{ photon.cm}^{-3}$) the THz dynamics contains an ultrafast (hundreds of femtoseconds) decay component (see Fig. 7.13). This ultrafast decay component vanishes at excitation densities exceeding $10^{19} \text{ photon.cm}^{-3}$. To reveal its origin, we probed the carrier dynamics also using longer excitation wavelength (510 nm) which generates carriers with very low excess energy. It has been found that at low photon densities ($\leq 10^{18} \text{ photon.cm}^{-3}$) the dynamics of the yield-mobility product at excitation wavelength 510 nm does not contain any ultrafast feature (see

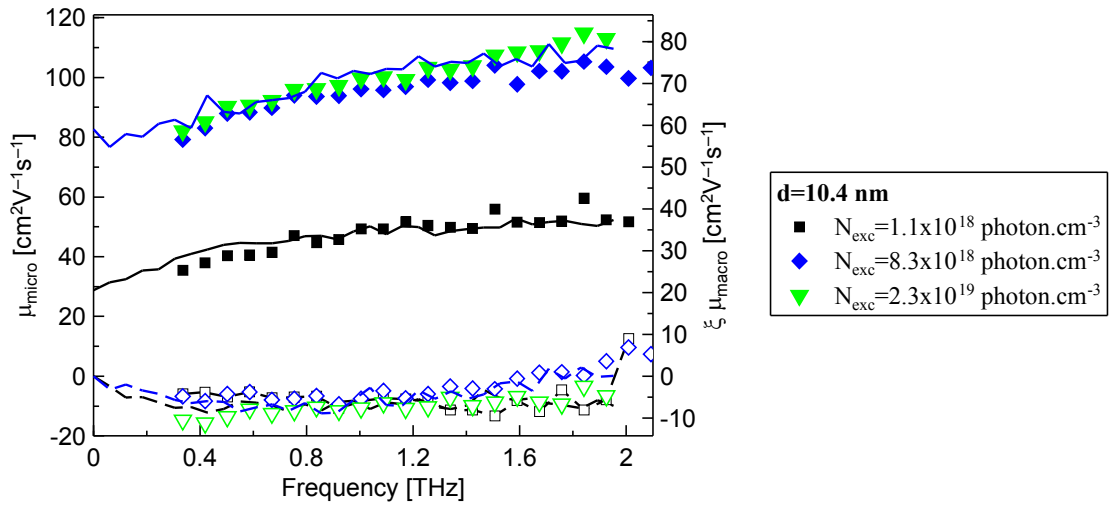


Figure 7.6: Measured yield-mobility spectra for nanocrystalline CdS with nanocrystal size 10.4 nm. The symbols represent the measured data (closed- real part, open symbols imaginary part) and the lines show the mobility spectra from Monte-Carlo simulations assuming Boltzmann statistics. The left axis shows the microscopic mobility, the right axis displays the measured yield-mobility product.

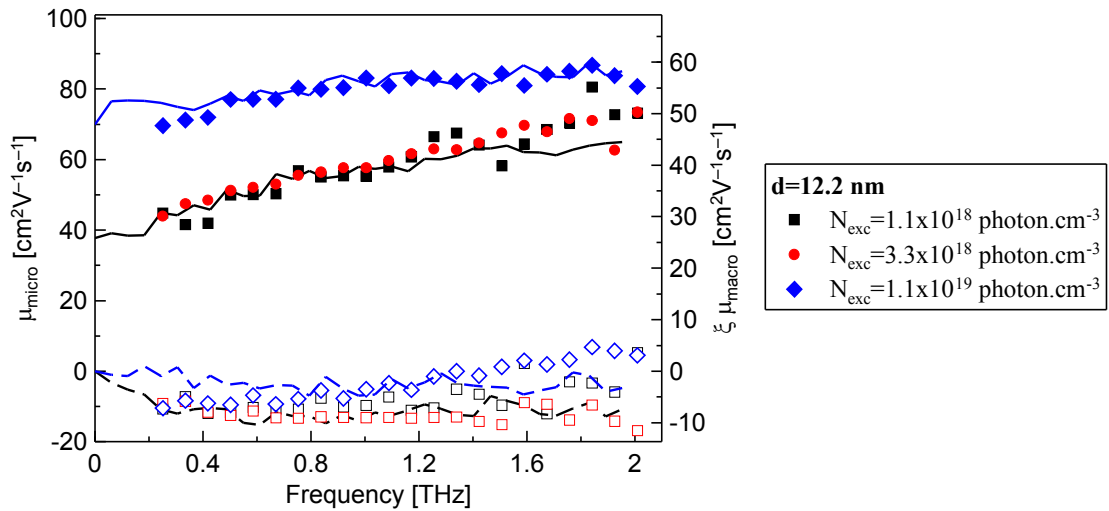


Figure 7.7: Measured yield-mobility spectra for nanocrystalline CdS with nanocrystal size 12.2 nm. The symbols represent the measured data (closed- real part, open symbols imaginary part) and the lines show the mobility spectra from Monte-Carlo simulations assuming Boltzmann statistics. The left axis shows the microscopic mobility, the right axis displays the measured yield-mobility product.

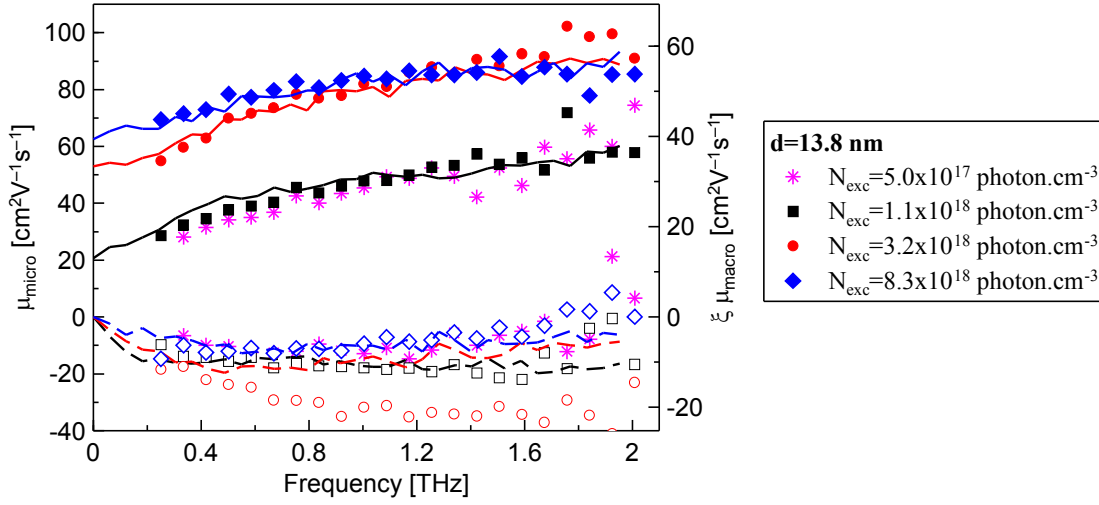


Figure 7.8: Measured yield-mobility spectra for nanocrystalline CdS with nanocrystal size 13.8 nm. The symbols represent the measured data (closed- real part, open symbols imaginary part) and the lines show the mobility spectra from Monte-Carlo simulations assuming Boltzmann statistics. The left axis shows the microscopic mobility, the right axis displays the measured yield-mobility product.

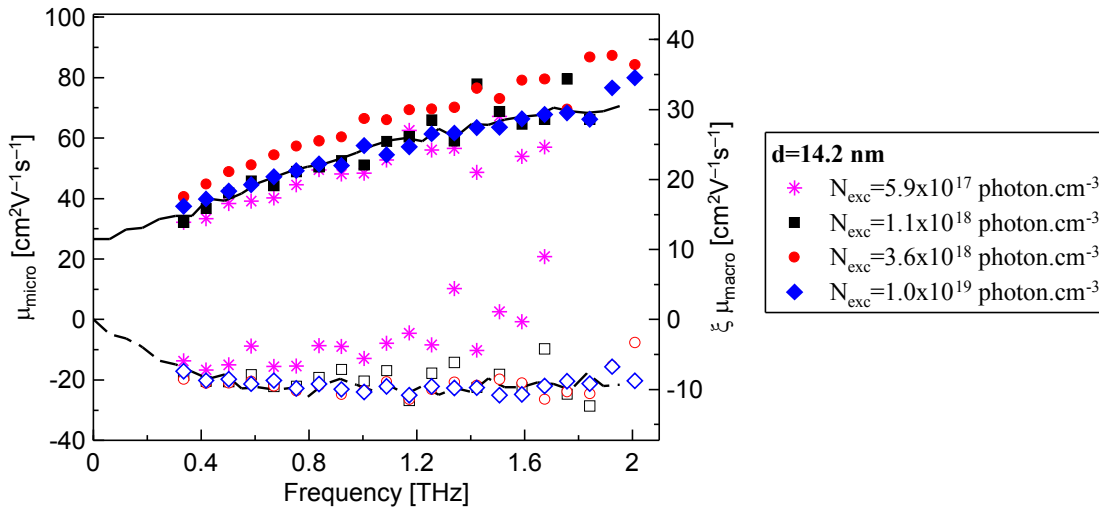


Figure 7.9: Measured yield-mobility spectra for nanocrystalline CdS with nanocrystal size 14.2 nm. The symbols represent the measured data (closed- real part, open symbols imaginary part) and the lines show the mobility spectra from Monte-Carlo simulations assuming Boltzmann statistics. The left axis shows the microscopic mobility, the right axis displays the measured yield-mobility product.

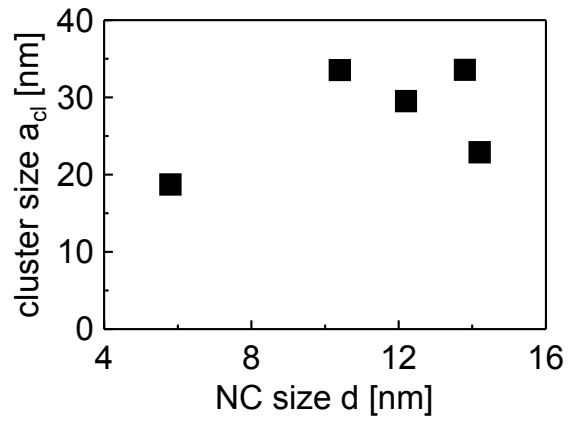


Figure 7.10: Size of the clusters of nanocrystals as a function of the nanocrystal size.

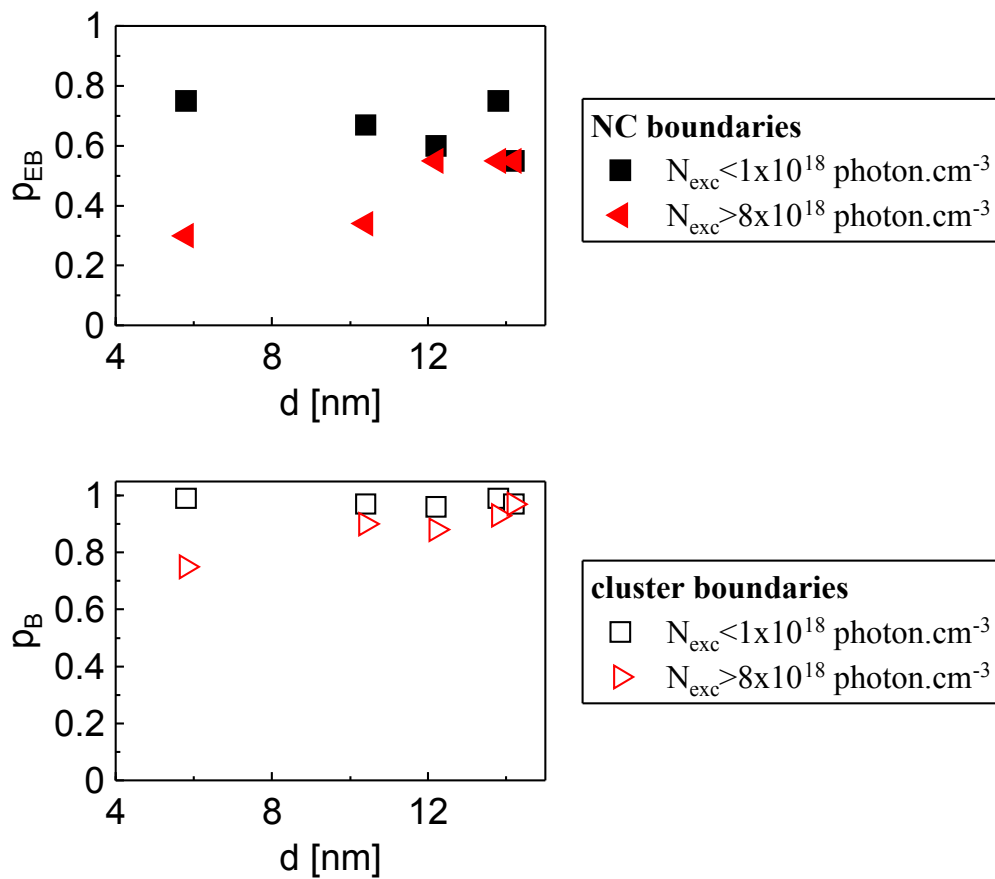


Figure 7.11: Probability of the blocking of electrons on the boundaries of nanocrystals (upper panel) and clusters (lower panel).

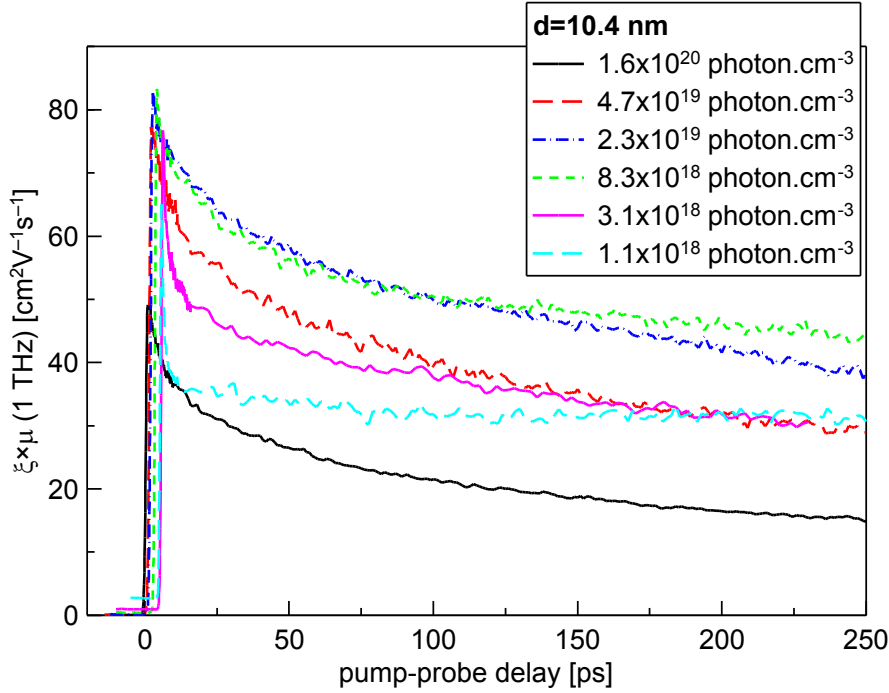


Figure 7.12: Measured dynamics of the yield-mobility product for nanocrystalline CdS with nanocrystal size 10.4 nm.

Fig. 7.14, curve c). Consequently, the carrier dynamics strongly depend on the initial excess energy of the carriers; we attribute the observed ultrafast decay of mobility to the relaxation of the excess energy.

- For high excitation densities the yield-mobility product decreases with a time constant ~ 200 ps. It becomes slower with decreasing excitation density and ultimately vanishes at $\sim 3 \times 10^{18}$ photon.cm $^{-3}$. We attribute this slow decrease to the decrease of the quantum yield $\xi_{mobile}(t)$, i.e. the electron density decays due to recombination or Auger process. [97]

To gain a detailed insight into the carrier dynamics, we developed a simple two-level model (Fig. 7.14 and Fig. 7.15). Carriers with low/high excess energy are characterized by a mobility μ_L and μ_H , respectively. The density of available electron states (number of states per unit volume) at the lower level is finite: N_0 . The kinetic equations for the electron population per unit volume then read:

$$\begin{aligned} \frac{\partial N_H}{\partial t} &= G_H(t) - \frac{N_H}{\tau_{HL}} \left(1 - \frac{N_L}{N_0}\right) - D_H(N_H, N_L) \\ \frac{\partial N_L}{\partial t} &= G_L(t) + \frac{N_H}{\tau_{HL}} \left(1 - \frac{N_L}{N_0}\right) - D_L(N_H, N_L) \end{aligned} \quad (7.2.1)$$

where N_H and N_L are the concentrations of electrons at the high and low-mobility level, respectively. The terms $D_H(N_H, N_L)$ and $D_L(N_H, N_L)$ in Eq. 7.2.1 describe

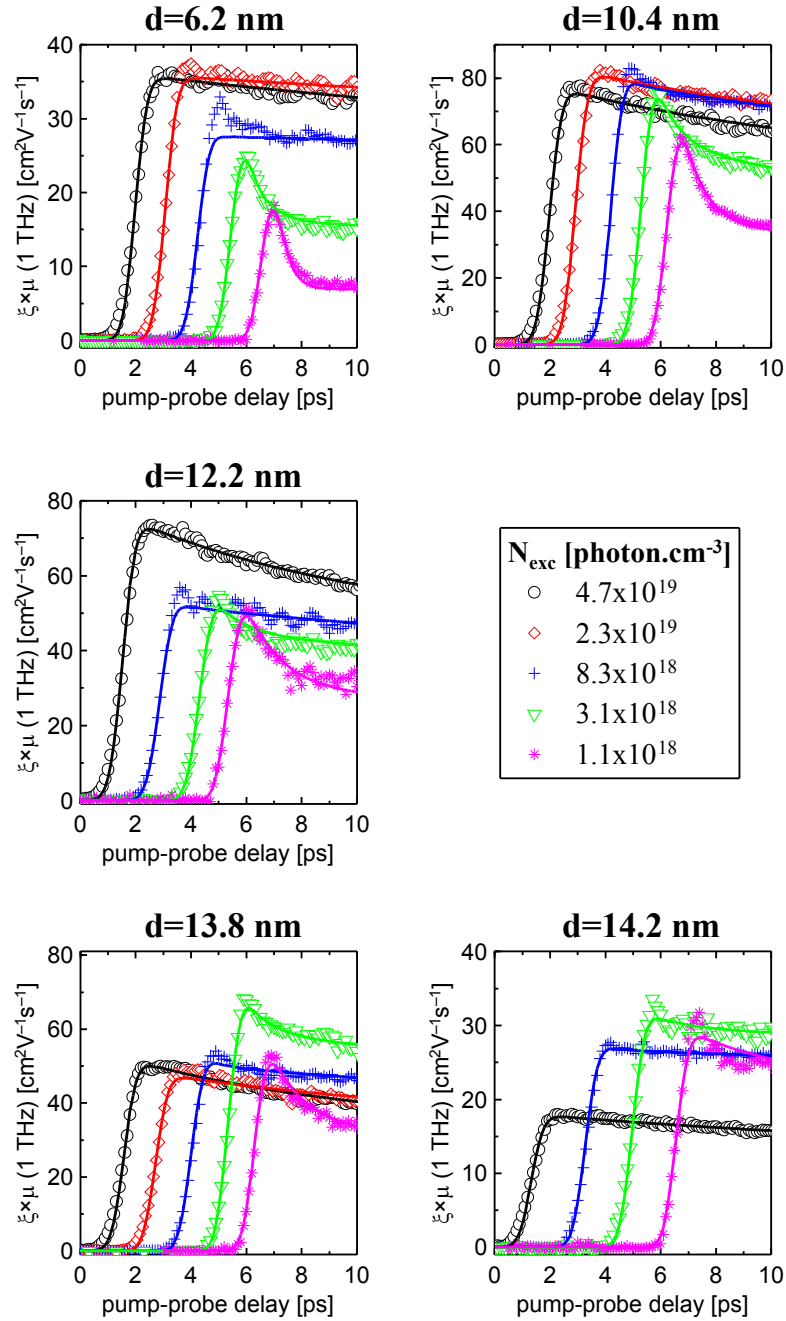


Figure 7.13: Early ultrafast THz dynamics of the studied nanocrystalline CdS samples. The symbols represent the measured data, the lines display a fit by our model of energy relaxation. For clarity the time origin of the curves is shifted.

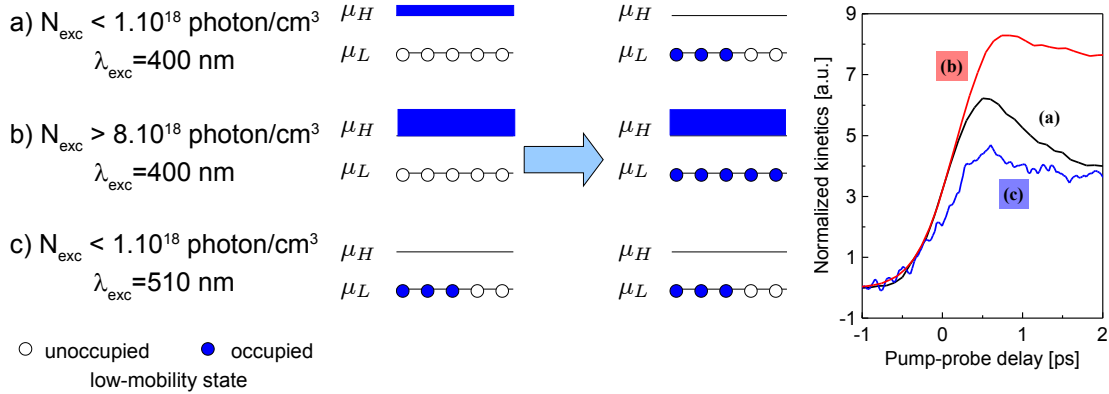


Figure 7.14: Model of the dynamics of the carrier energy relaxation in nanocrystalline CdS. a) For low excitation densities and high photon energies carriers with high mobility μ_H are generated. During thermalization their excess energy is lost, and their mobility decreases to μ_L . b) For high excitation densities and high photon energies carriers with high mobility μ_H are generated. During thermalization the low-mobility states become filled with a small fraction of the generated carriers and the decrease in electron mobility is not observed. c) For low excitation densities and low photon energies electrons with low mobility are generated. Their mobility during thermalization does not change.

the slow decay of the electron concentration. The generation rates depend on the excitation wavelength λ_{exc} :

- for $\lambda_{exc} = 400$ nm $G_H = N_{exc} \delta(t)$ and $G_L = 0$
- for $\lambda_{exc} = 510$ nm $G_H = 0$ and $G_L = N_{exc} \delta(t)$

The electron concentrations are connected with the photoconductivity of the sample by the following equation:

$$(\xi\mu)_{meas}(t) = \frac{N_H(t) \mu_H + N_L(t) \mu_L}{N_{exc}} \quad (7.2.2)$$

Our explanation for the early dynamics of the electron transport in nanocrystalline CdS is the following. Electrons photogenerated by a 400 nm laser pulse have a high excess energy, therefore they are generated exclusively on the upper level ($G_L(t) \equiv 0$). During their thermalization they fall down to the lower level with a time constant τ_{HL} ; this process is accompanied by a decrease of the electron mobility (Fig. 7.14 a). If the excitation density is high, the lower level fills up during the thermalization and the majority of electrons remains on the upper level. Consequently, one cannot observe a decrease of mobility (Fig. 7.14 b). If the wavelength of the excitation pulse is longer (510 nm), electrons are generated directly at the lower level ($G_H(t) \equiv 0$) and the thermalization does not have any effect on the carrier mobility (Fig. 7.14 c).

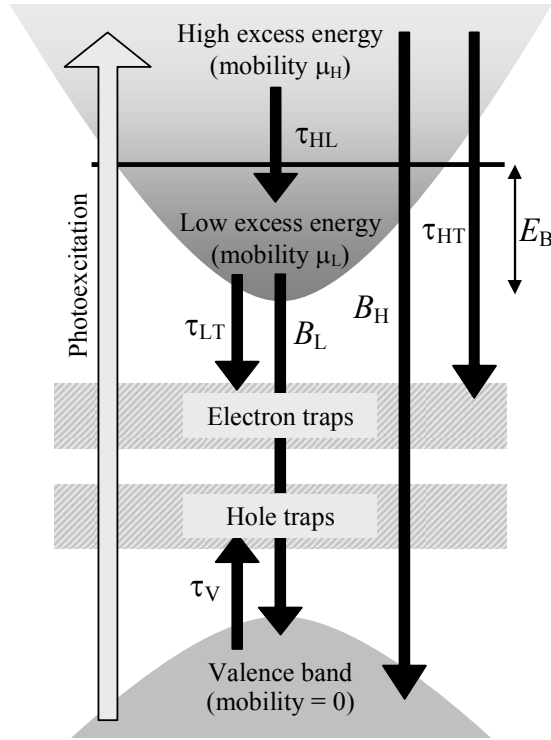


Figure 7.15: Two-level model in a semiconductor: electrons with kinetic energy above E_B have high mobility μ_H , whereas those with excess energy below E_B have low mobility μ_L . Scheme of carrier dynamics: recombination and trapping.

The two-level model may be connected with an energy barrier E_B in the conduction band; electrons with excess (kinetic) energy above E_B are more delocalized than those with kinetic energy below E_B (see Fig. 7.15). Assuming parabolic conduction bands in CdS nanocrystals, the barrier height is connected to the concentration of available states N_0 at the lower level by the following equation:

$$E_B = \frac{h^2}{2m_e} \left(\frac{3N_0}{8\pi} \right)^{\frac{2}{3}} \quad (7.2.3)$$

where h is the Planck-constant. By comparing this simple model with the measured THz dynamics the mobility of electrons on the upper and lower level and the height of the energy barriers E_B can be determined. The obtained value of E_B is displayed for each sample in Fig. 7.17. It decreases with increasing nanocrystal size. This behaviour is very similar to the increase of transparency of nanocrystal and cluster boundaries calculated in the previous section – here the difference between the probability of electron blocking on nanocrystal boundaries at low and high excitation densities [$p_{EB}(\text{low}) - p_{EB}(\text{high})$] clearly decreases with increasing nanocrystal size (see Fig. 7.11).

The energy barriers controlling the carrier transport may originate from the electrostatic interaction of electrons with holes. It has been shown that holes become rapidly trapped mostly within the nanocrystal where they were created. [98] The trapped hole creates an electrostatic field which affects the electron motion. The energy which is needed to bring an electron from the nanocrystal infinitely far away ranges from $U_{in} = 3e_0^2 / (4\pi\epsilon_0\epsilon_r d)$ (electron in the center of the nanocrystal) to $U_{surf} = e_0^2 / (2\pi\epsilon_0\epsilon_r d)$ (electron at the surface of the nanocrystal). Indeed, we see that E_B is comparable with U_{surf} (Fig. 7.17).

An estimation on the height of the energy barriers can be gained also from the measured yield-mobility spectra. The simulation was generalized by adding a piecewise harmonic potential which modulates the electron motion inside the nanocrystals. The height of the energy barriers E_B then corresponds to the difference of the electric potential between the centre of a nanocrystal and its surface (see Fig. 7.16).

For simplicity, we assumed that electrons with high excess energy do not feel the additional potential – the blocking probabilities then correspond to those shown in Fig. 7.11 for $N_{exc} > 8 \times 10^8$ photon.cm⁻³. These blocking probabilities are then kept also for electrons with low excess energy. The increase of the blocking probabilities is then accomplished by switching on the additional potential. The potential depth E_B is set to such a value that the simulation fits the electron mobility measured in the low density regime (see the agreement between the simulated and measured spectra in Fig. 7.16). The heights of the energy barriers extracted from the measured spectra correspond well to the values calculated from the carrier dynamics (see Fig. 7.17). Note that this approach is an independent confirmation of the existence and height of the barriers.

Let us briefly discuss the terms $D_H(N_H, N_L)$ and $D_L(N_H, N_L)$ in Eq. 7.2.1 which describe the slow decay of the electron concentration due to recombination or due to the Auger process. Auger recombination is a process which is expected to be enhanced in nanocrystals due to the spatial confinement of charge carriers. [97] In this process one electron-hole pair recombines nonradiatively giving its energy to another carrier, e.g. to an electron (eeh process) which is promoted to a state with a high excess energy. In turn, this can lead to an enhancement of the conductivity in spite of the fact that the total number of excited carriers decreases. The localized carriers can also take part in the Auger process due to its Coulomb-interaction origin. However, taking into account the fact that the fast energy relaxation is likely to be much faster than the Auger recombination process, a possible increase in the average mobility dynamics should be negligible.

In our fits we found that a dominant Auger recombination is not compatible with the shape of our kinetics in CdS, while a significant bimolecular recombination may take place. For example, for recombination coefficients in the sample with nanocrystal size $d = 10.4$ nm we have found $B_H \approx 4.5 \times 10^{-22}$ cm³ps⁻¹ and $B_L \approx 5.1 \times 10^{-21}$ cm³ps⁻¹ (see the meaning of the coefficients in Fig. 7.15). For the other samples these values are roughly comparable. These values are sim-

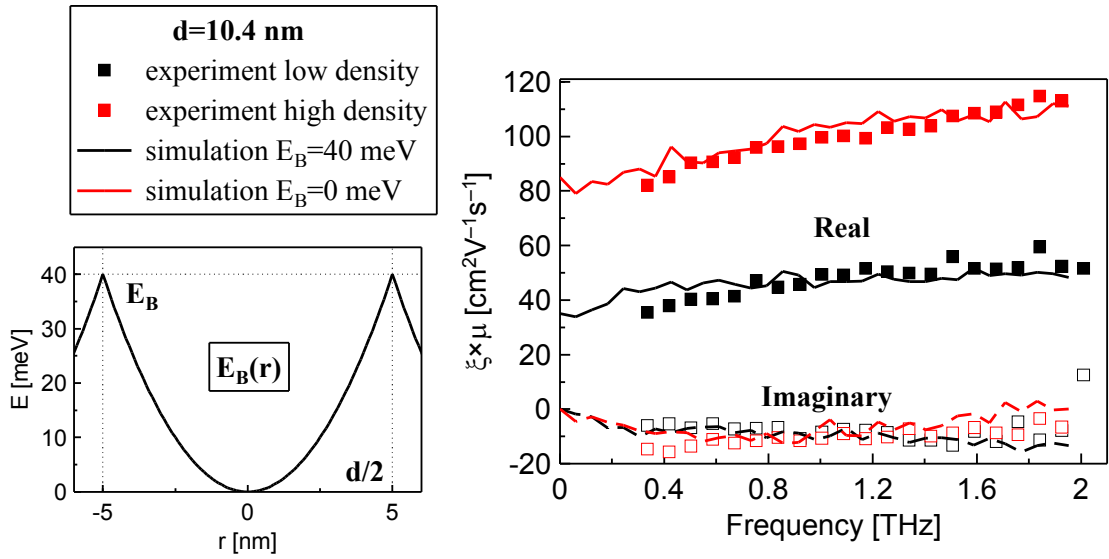


Figure 7.16: Left panel: model of energy barriers in our simulations – harmonic potential inside nanocrystals. Right panel: simulations compared with experimental data for the sample with nanocrystal size 10.4 nm.

ilar to those found in 5-nm CdS NCs by Juodkazis et al. [99]. These authors also reported the value of Auger recombination coefficient $\sim 3 \times 10^{-42} \text{ cm}^6 \text{ps}^{-1}$, which leads to the Auger recombination time of ~ 130 ps for the highest excitation density we used in our experiments. However, our measurements were done in a limited time window and using a narrow range of excitation fluences; consequently, the Auger recombination could not be clearly distinguished from the bimolecular one in our data. On the one hand, this limits the accuracy of our determination of B_L and B_H , and, on the other hand, we can conclude that $\sim 3 \times 10^{-42} \text{ cm}^6 \text{ps}^{-1}$ is the upper limit for the Auger coefficient in the CdS NCs grown by CBD.

7.3 Electron mobility spectra for high excitation densities. Fermi-Dirac statistics.

If the electron concentration exceeds 10^{19} cm^{-3} , the Fermi level of the system of electrons becomes considerably higher than the electron thermal energy and the Monte Carlo simulations should be performed using Fermi-Dirac statistics. The electron velocity is in this regime determined by the Fermi velocity: with increasing electron concentration the Fermi-level increases and so does the electron velocity. Electrons with higher velocity interact more often with nanocrystal and cluster boundaries, therefore with the increase of the electron density the mobility becomes smaller (see Subsec. 2.2.7). Such a decrease is observed also in our

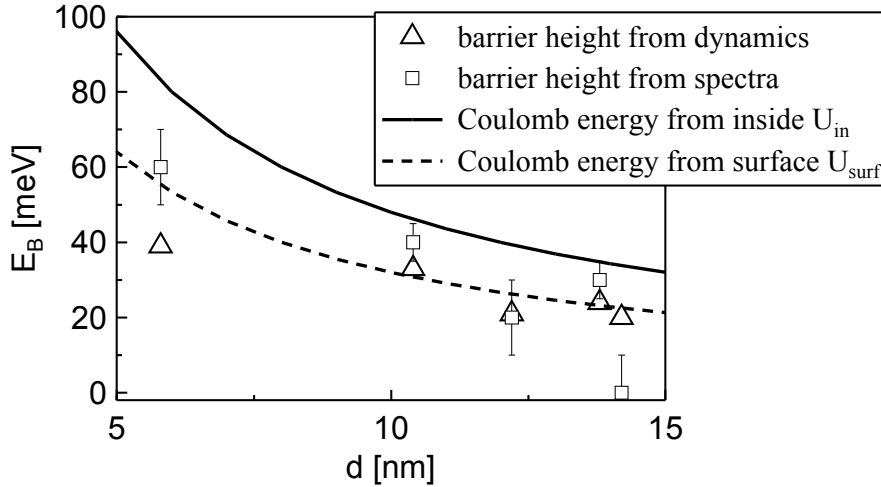


Figure 7.17: The height of the energy barriers deduced from the measured electron dynamics (Eq. 7.2.1) (triangles) and spectra (squares) compared to the energy needed to bring an electron from the centre (solid line)/surface (dashed line) of a nanocrystal charged by a single hole.

experiments, therefore our model qualitatively explains the electron mobility in the nanocrystalline samples even for high excitation densities.

For the sample with the largest nanocrystal size ($d = 14.2$ nm) we obtain a quantitative agreement between the experiment and the simulations. We found that, provided we use a shorter value of the scattering time: $\tau = 10$ fs, the experimental spectra can be sufficiently well reproduced by the simulated ones for the whole range of excitation densities and with the same blocking probabilities on nanocrystal and cluster boundaries as with Boltzmann statistics (see Fig. 7.23). As to the shorter scattering time: although the value of 10 fs is smaller than the scattering time in bulk CdS, such a choice can be justified by a possible higher density of defects in nanocrystalline samples than in bulk CdS.

For the rest of the samples ($d < 14.2$ nm) the agreement between the simulations and measurements is only qualitative. We attempted to improve the quality of our model by adjusting parameters of electron blocking. It has been found that the best agreement is reached if we assume that for electron densities $\gtrsim 10^{19}$ cm $^{-3}$ the electrons do not feel the nanocrystal boundaries at all, i.e. $p_{ET} = 1$.

To illustrate our models we compare the measured mobility at 1 THz with that obtained from simulations using Boltzmann and Fermi-Dirac statistics. This approach is justified by the fact that the shape of the spectra does not change significantly with the electron density. In Figures 7.19, 7.20, 7.21 and 7.22 we present the measured electron mobility for various samples. The data are compared to the results of simulations which involve:

1. Boltzmann statistics with simulation parameters identical to those used in Sec. 7.1.

2. Fermi-Dirac statistics with parameters identical to those used in Sec. 7.1. For excitation densities $\gtrsim 10^{19}$ photon.cm $^{-3}$ all the simulation parameters are identical, except for the Fermi-level.
3. Fermi-Dirac statistics with permeable nanocrystals ($p_{ET} = 1$).

It can be seen that using Fermi-Dirac statistics and assuming permeable nanocrystal boundaries our model is significantly improved for excitation densities around $\sim 10^{19}$ photon.cm $^{-3}$. On the other hand, for higher excitation densities the electron mobility is still somewhat underestimated by the simulations with Fermi-Dirac statistics.

We attempted to explain this discrepancy by saturation of optical absorption in nanocrystalline CdS. In this case the electron concentration increases sublinearly with increasing pump fluence. If the sample is much thicker than the skin depth, the absorption depth increases. As a result, the total number of photo-generated electrons does not change. The combination of the sublinear growth of electron concentration and enlarged photoexcited sample volume would result in a slower decrease of mobility than in the case of a linear regime, where the pump fluence and electron density are directly proportional to each other. We performed additional optical experiments in order to confirm or reject this hypothesis. We measured the optical transmission coefficient for nanocrystalline CdS films thinner than those studied by THz spectroscopy, but similar in other properties. We have found that the absorption depth did not change in the whole range of excitation densities used in our study. Saturation of optical absorption therefore cannot explain the electron mobility at high densities.

The difficulty to explain this problem may originate from the fact that the dependence of the electron mobility on the electron density is determined by two phenomena:

- Reduction of electron blocking due to the increase of electron excess energy (with increasing electron density) results in an increase of the electron mobility, which is visible for electron densities lower than $\sim 10^{19}$ cm $^{-3}$.
- In the regime of degenerated electron system the increase of the Fermi-level results in a decrease of the electron mobility. It is observed for electron densities higher than 10^{19} cm $^{-3}$.

The crossover between the two regimes leads to a plateau in the electron mobility which is visible for example in Fig. 7.22 between excitation densities 3×10^{18} cm $^{-3}$ and 4×10^{19} cm $^{-3}$. From the current number of measured data points it is not possible to distinguish between the two phenomena and characterize both of them separately. The ultimate solution of this problem remains an open challenge.

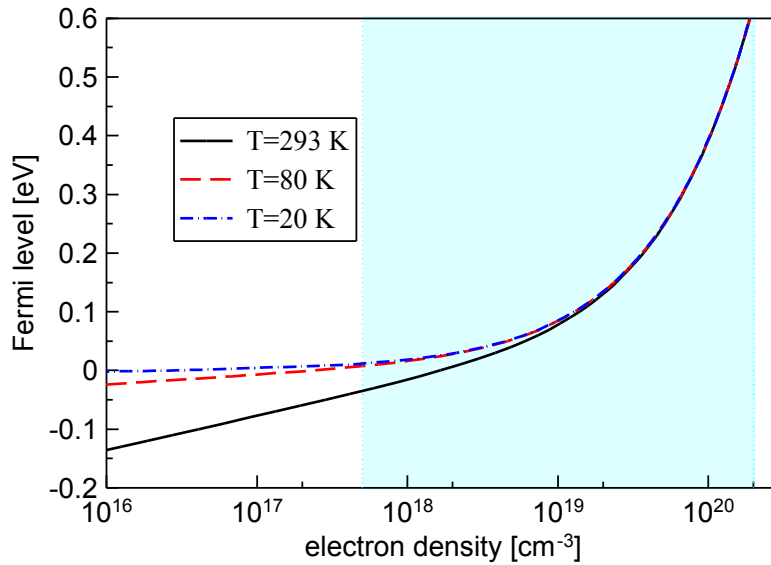


Figure 7.18: Fermi level of an electron gas system in CdS. The range of electron densities in our experiments is highlighted.

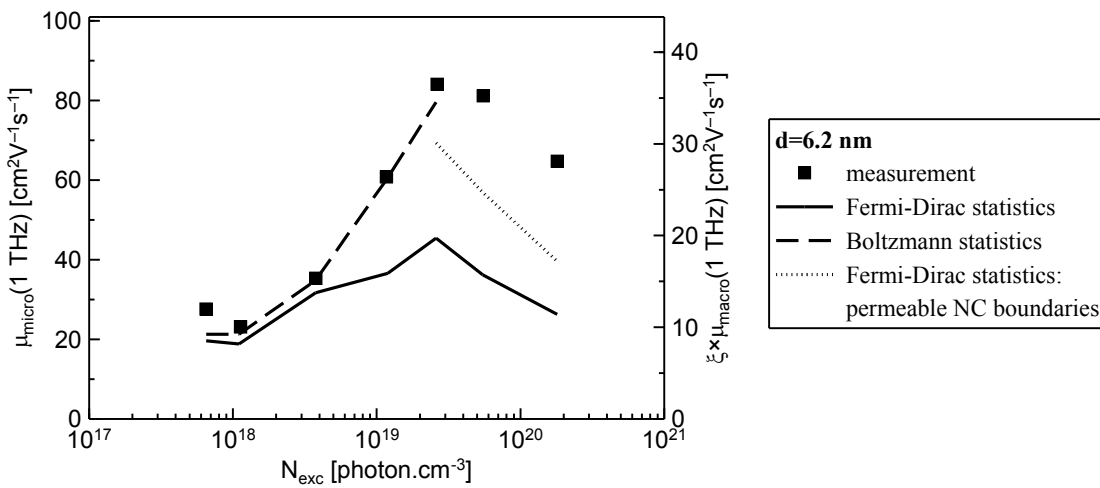


Figure 7.19: Comparison of measured (dots) and simulated (lines) electron mobility for CdS nanocrystals with size $d=6.2$ nm. The solid line represents simulations using Fermi-Dirac statistics with parameters identical to those used in Sec. 7.1, the dashed line shows simulations using Boltzmann statistics (Sec. 7.1) and the dotted line displays simulations using Fermi-Dirac statistics and permeable nanocrystals ($p_{ET} = 1$).

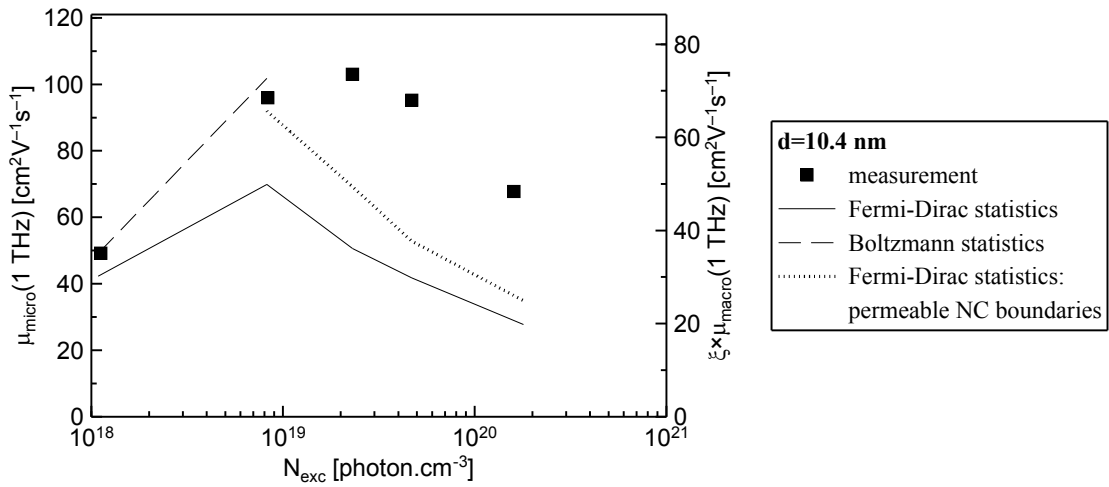


Figure 7.20: Comparison of measured (dots) and simulated (lines) electron mobility for CdS nanocrystals with size $d=10.4$ nm. The solid line represents simulations using Fermi-Dirac statistics with parameters identical to those used in Sec. 7.1, the dashed line shows simulations using Boltzmann statistics (Sec. 7.1) and the dotted line displays simulations using Fermi-Dirac statistics and permeable nanocrystals ($p_{ET} = 1$).

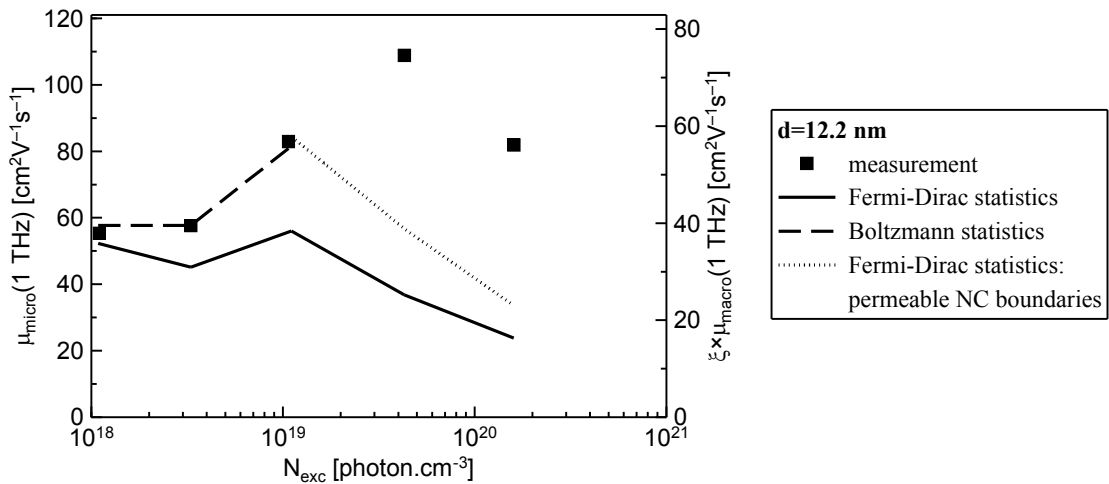


Figure 7.21: Comparison of measured (dots) and simulated (lines) electron mobility for CdS nanocrystals with size $d=12.2$ nm. The solid line represents simulations using Fermi-Dirac statistics with parameters identical to those used in Sec. 7.1, the dashed line shows simulations using Boltzmann statistics (Sec. 7.1) and the dotted line displays simulations using Fermi-Dirac statistics and permeable nanocrystals ($p_{ET} = 1$).

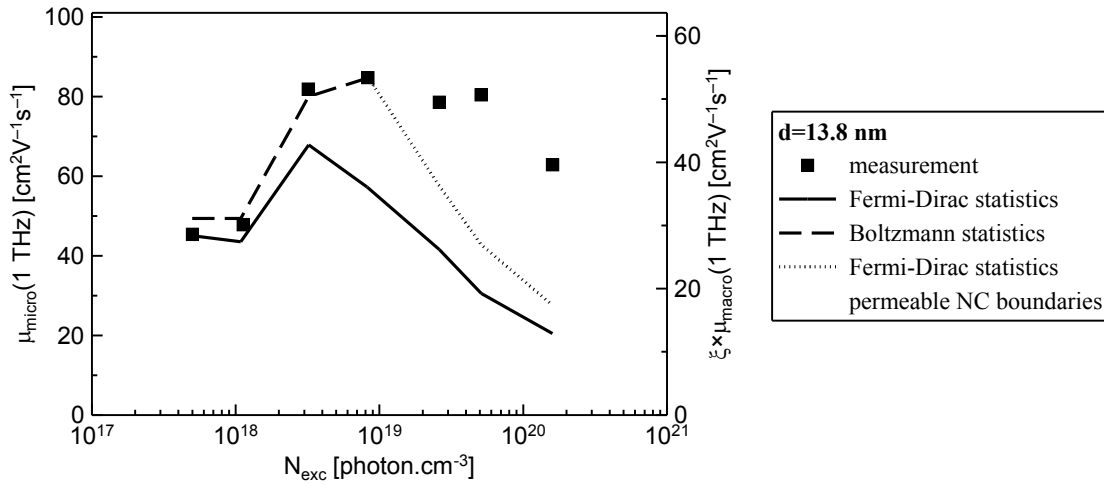


Figure 7.22: Comparison of measured (dots) and simulated (lines) electron mobility for CdS nanocrystals with size $d=13.8 \text{ nm}$. The solid line represents simulations using Fermi-Dirac statistics with parameters identical to those used in Sec. 7.1, the dashed line shows simulations using Boltzmann statistics (Sec. 7.1) and the dotted line displays simulations using Fermi-Dirac statistics and permeable nanocrystals ($p_{ET} = 1$).

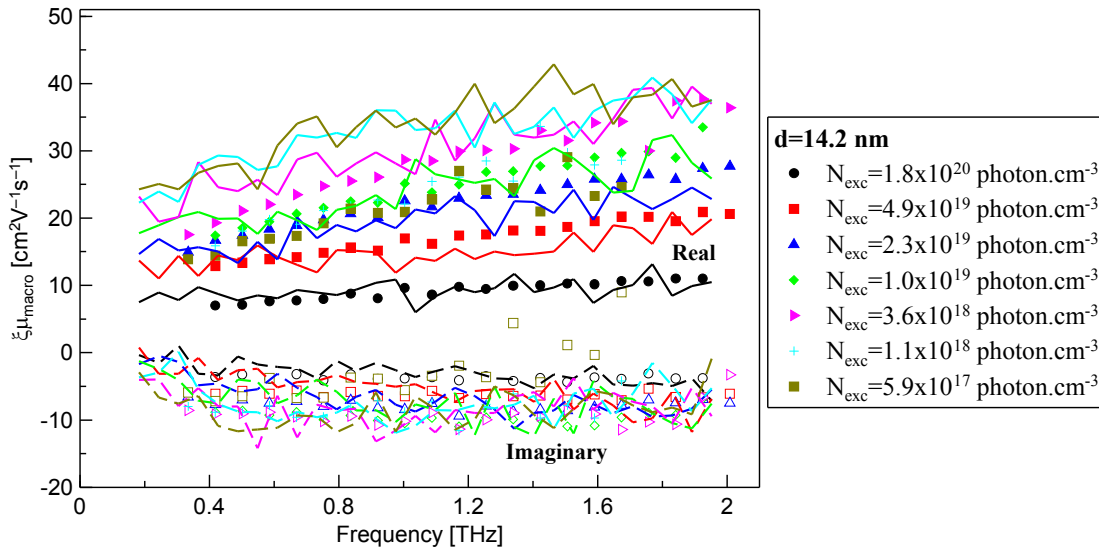


Figure 7.23: Electron mobility spectra of nanocrystalline CdS with nanocrystal size 14.2 nm . The symbols represent the measured data, the lines display the simulated mobility.

7.4 Electron transport at low temperatures

Time-resolved THz measurements were carried out to explore the electron transport in nanocrystalline CdS also at temperatures 20 K and 80 K. The behaviour of the mobility spectra in the excitation density range of $10^{18} - 10^{20}$ photon.cm⁻³ is similar to that measured at room temperature. It has been found that at low electron densities the mobility increases with decreasing temperature (see Fig. 7.24) and at high electron densities the mobility spectra are temperature-independent (see Fig. 7.25). Our simulations give a similar result which can be explained as follows. At low excitation densities the electron system obeys the Boltzmann statistics and the electron velocity is governed by the temperature. Consequently, the average electron velocity is lower at 20 K than at room temperature. Slower electrons interact with nanocrystal boundaries less frequently, therefore they are less localized and their mobility is higher. On the other hand, at high electron densities the carrier transport is determined by the Fermi velocity, which is temperature independent under these conditions (see Fig. 7.18). As a result, the mobility is also independent of temperature. At low temperatures the electron dynamics exhibits a similar ultrafast decrease of electron mobility as that described in section 7.2, although the time constant is slightly larger (see Fig. 7.26). We find $\tau_{HL} \approx 0.5$ ps at room temperature and $\tau_{HL} \approx 4$ ps at 20 K.

For low excitation densities the electron mobility at 20 K is larger than at room temperature. This gave us the possibility to measure low-temperature mobility spectra at even lower excitation densities. We discovered that the mobility significantly increases upon a decrease of the pump fluence. This fact allowed us to decrease further the excitation density by nearly 2 orders of magnitude. For excitation densities $2 - 4 \times 10^{16}$ photon.cm⁻³ it has been found that the mobility spectra do not exhibit a localized character anymore, they remind mobility spectra of delocalized charges: we observe a decreasing real part and a positive imaginary part (see Fig. 7.27). In other words, with a decreasing electron density a crossover has been observed between delocalized and localized regime. Such a behaviour is possible only if the electrons are delocalized over several nanocrystals, as suggested by our simulations; i.e. from the point of view of the carrier transport the electrons do not feel any confinement. This is in a contrast with the optical spectra which clearly reflect the electron confinement at 20 K. Here we touch a long-lasting controversy [100] between an optically observed quantum confinement of charges and bulk-like dc transport in the electrical measurement. In other words, we observe a contrast between a coherent regime at optical frequencies determined by wavefunctions of confined electrons and a presumably incoherent regime of carrier transport where collisions of other coherence-breaking phenomena may occur during the period of the probing THz field.

The quantitative characterization of the electron transport at low temperatures in nanocrystalline CdS requires both the characterization of bulk CdS at low temperatures and the solution of the problem of transition between delocal-

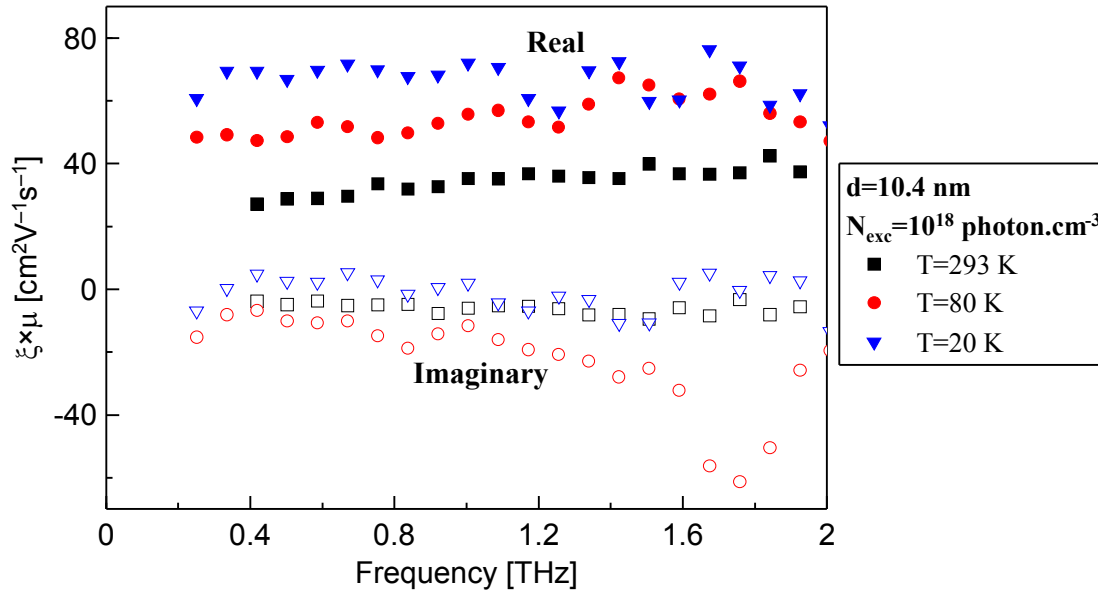


Figure 7.24: Electron yield-mobility product measured for low excitation densities and different temperatures.

ized and localized states at low electron densities. These tasks are beyond the scope of a single thesis and provide a strong motivation for the continuation of this research.

7.5 Conclusion

We have examined the mobility of photogenerated carriers in nanocrystalline CdS using time-resolved THz spectroscopy. Measurements were carried out for samples with different nanocrystal size and in a wide range of electron densities.

We have found a quantitative connection between the shape of the electron mobility spectra and the structure of the material. Using our simulations we have been able to identify electron localization on two different length scales.

It has been found that the mobility of electrons changes substantially with their kinetic energy. The magnitude of this change was found to decrease with increasing nanocrystal size. A hypothesis was formulated based on this fact explaining the observe change of mobility by an electrostatic interaction between electrons and trapped holes. Our simulations were able to describe the measured electron mobility also at high electron densities and at low temperatures.

Furthermore it has been found that at 20 K and electron densities $2 \times 10^{16} \text{ cm}^{-3}$ electrons experience a transition from a localized to a delocalized regime; this may be a starting point for further experiments in this field under conditions of very low excitation densities.

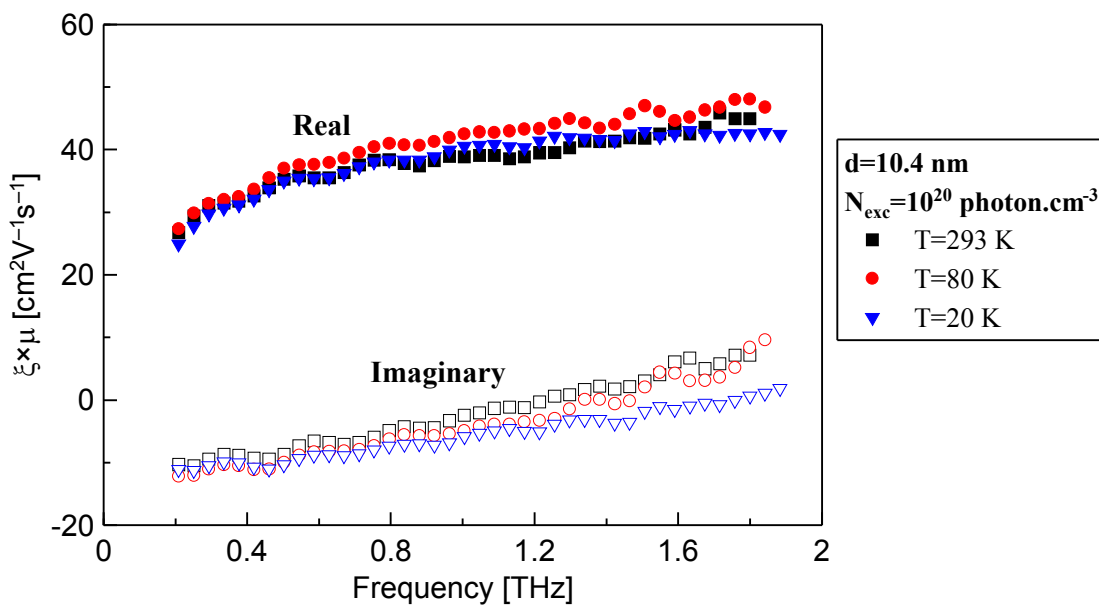


Figure 7.25: Electron yield-mobility product measured for high excitation densities and different temperatures.

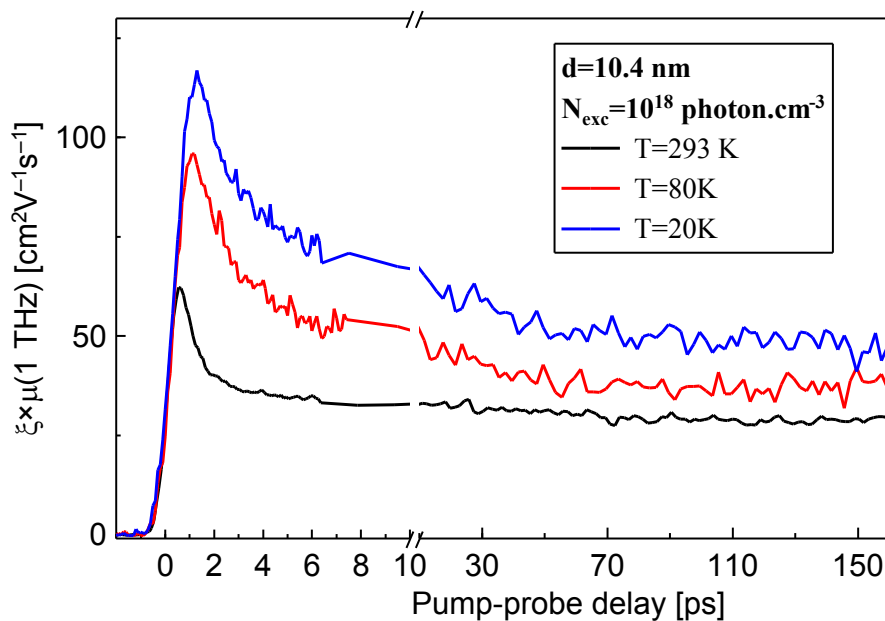


Figure 7.26: Electron kinetics measured for low excitation densities and different temperatures.

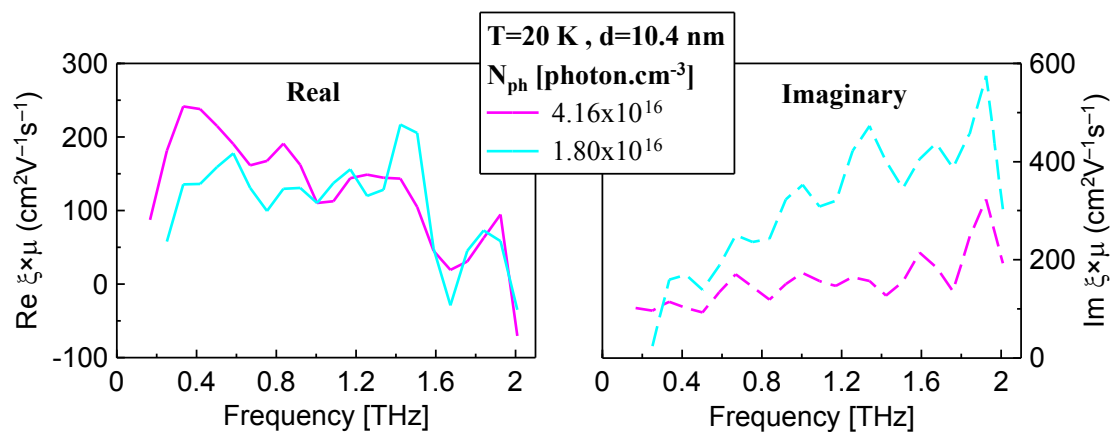


Figure 7.27: Electron mobility spectra for nanocrystalline CdS at 20 K and very low electron densities.

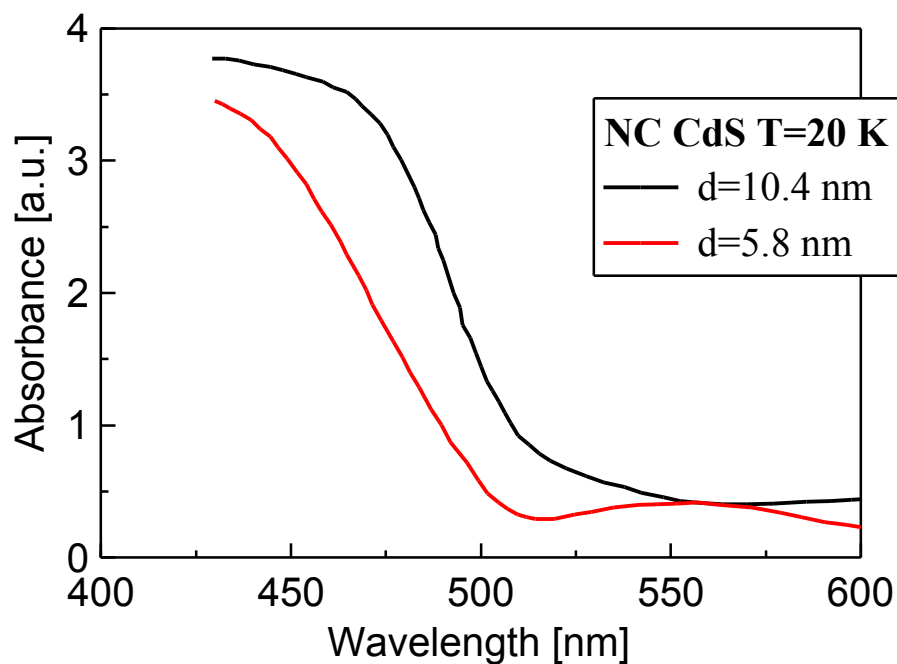


Figure 7.28: Optical absorption spectra of nanocrystalline CdS at 20 K for different nanocrystal sizes.

Chapter 8

Conclusion

This thesis investigates systems of charge carriers experiencing different degrees of delocalization. It has been shown that a combination of two methods, THz spectroscopy and simulation of carrier thermal motion is able to give a detailed quantitative picture of carrier transport in nanocrystalline systems for a wide range of parameters such as temperature and carrier density. We investigated several systems:

- The mechanism of carrier transport in pellets of niobium-doped titania nanoparticles was clearly identified using THz time-domain spectroscopy. It has been shown that the carrier transport is dominated by hopping. The influence of the depolarization fields on the carrier transport was modeled by the Bergman theorem; a simple parametrization of the Bergman spectral function was used. It consists of two delta functions: one describes a percolated component and the other represents the contribution of isolated inclusions. Using this model the effect of annealing and of the Nb doping on the pellets could be evaluated. It has been found that annealing improves the crystallinity of the samples, namely, it leads to an increase of the percolation of their crystalline part. Nb-doping introduces lattice deformations in the titania nanoparticles which lead to high extrinsic losses. These results are summarized in Fig. 4.4.
- We investigated electron states populated by photoionization in water and aqueous solutions of various salts by time-resolved spectroscopy. The density of solvated electrons was measured by optical pump–optical probe spectroscopy. The mobility of intermediate electron states generated within 1 ps after photoexcitation was probed by optical pump–THz probe spectroscopy. We have not observed any spectral feature from these states in the THz frequency range. Based on this fact we determined that the intermediate states cannot be delocalized over a length scale longer than ~ 5 nm within 100 – 300 fs.
- We studied the photoconductivity of bulk ZnO using time-resolved THz

spectroscopy. We have identified several types of carriers: free carriers with high mobility at temperature lower than 80 K and at low carrier densities, high density electron-hole plasma and excitons which were interestingly observed only for temperatures higher than 80 K. Our investigation allowed to establish a relation between two previous studies on the photoconductivity of bulk ZnO, which were seemingly incompatible. [18, 88]

- Using the combination of THz time-resolved measurements and simulations a complete study was performed on the photoconductivity of nanocrystalline ZnO. At 20 K only mobile carriers, while at room temperature mobile carriers and excitons were observed. The response of mobile carriers originates from their thermal motion which involves backscattering on nanocrystal boundaries. Upon such interactions the probability that the electron moves to another nanocrystal is only 25% in our samples. The strong oscillator strength of the excitons and the significant change of electron scattering time at 20 K shows an enhanced electron-hole interaction due to the confinement in nanocrystals.
- The mobility of photogenerated electrons was studied in nanocrystalline CdS. It has been shown that carriers experience localization on two length scales corresponding to the size of nanocrystals and clusters of nanocrystals. The fact, that the carrier mobility could be simulated in such a complicated structure, demonstrates the flexibility of our model. It has been found that the extent of carrier localization is lowered with increasing electron excess energy. This phenomenon is related to the existence of energy barriers at nanocrystal boundaries. The energy barriers may be connected with the interaction between mobile electrons and trapped holes.
- At 20 K and at low electron densities ($2 \times 10^{16} \text{ cm}^{-3}$), the carrier mobility in nanocrystalline CdS exhibits a Drude-like character showing that electrons are not localized anymore. Simultaneously, the optical absorption spectra of the material show electron states corresponding to confined electrons. This remains a challenge for further research.

Bibliography

- [1] N. V. Smith, Phys. Rev. B **64**, 155106 (2001).
- [2] B. O'Regan and M. Grätzel, Nano Lett. **6**, 755 (2006).
- [3] P. U. Jepsen, D. G. Cooke, and M. Koch, Laser Photonics Rev. **5**, 124 (2010).
- [4] F. A. Hegmann, O. Ostroverkhova, and D. G. Cooke, in *Photophysics of molecular materials*, edited by G. Lanzani (Wiley-VCH Verlag & Co. KGaA, Weinheim, 2006), Chap. Probing organic semiconductors with terahertz pulses, pp. 367–428.
- [5] H. Němec, P. Kužel, and V. Sundström, Phys. Rev. B **79**, 115309 (2009).
- [6] H. Nemeč, P. Kužel, and V. Sundström, J. Photochem and Photobiol. A-Chemistry **215**, 123 (2010).
- [7] E. Hendry, M. Koeberg, B. O'Regan, and M. Bonn, Nano Lett. **6**, 755 (2006).
- [8] D. J. Bergman, Phys. Rep. **43**, 377 (1978).
- [9] K. Ghosh and R. Fuchs, Phys. Rev. B **38**, 5222 (1988).
- [10] C. Pecharrromán and F. J. Gordillo-Vázquez, Phys. Rev. B **74**, 035120 (2006).
- [11] J. C. M. Garnett, Philos. Trans. R. Soc. London **205**, 237 (1906).
- [12] H.-K. Nienhuys and V. Sundström, Appl. Phys. Lett. **87**, 012101 (2005).
- [13] Z. Mics, F. Kadlec, P. Kužel, P. Jungwirth, S. E. Bradforth, and V. A. Apkarian, J. Phys. Chem. **123**, 104310 (2005).
- [14] H. Němec, P. Kužel, F. Kadlec, D. Fattakhova-Rohlfing, J. Szeifert, T. Bein, V. Kalousek, and J. Rathousky, Appl. Phys. Lett. **96**, 062103 (2010).
- [15] D. A. G. Bruggeman, Ann. Phys. **24**, 636 (1935).

-
- [16] J. Sturm, P. Grosse, and W. Theiss, *Z. Phys. B – Condensed Matter* **83**, 361 (1991).
- [17] M. C. Beard, G. M. Turner, and C. A. Schmuttenmaer, *J. Appl. Phys.* **2**, 983 (2002).
- [18] E. Hendry, M. Koeberg, and M. Bonn, *Phys. Rev. B* **76**, 045214 (2007).
- [19] R. A. Kaindl, M. A. Carnahan, D. Hägele, R. Lövenich, and D. S. Chemla, *Nature* **423**, 734 (2003).
- [20] P. Prins, F. C. Grozema, J. M. Schins, T. J. Savenije, S. Patil, U. Scherf, and L. D. A. Siebbeles, *Phys. Rev. B* **73**, 045204 (2006).
- [21] H. Němec, H.-K. Nienhuys, E. Perzon, F. Zhang, O. Inganas, P. Kužel, and V. Sundström, *Phys. Rev. B* **79**, 245326 (2009).
- [22] L. Fekete, P. Kužel, H. Němec, F. Kadlec, A. Dejneka, J. Stuchlík, and A. Fejfar, *Phys. Rev. B* **79**, 115306 (2009).
- [23] J. C. Dyre, *J. Appl. Phys.* **64**, 2456 (1988).
- [24] M. C. Beard, G. M. Turner, and C. A. Schmuttenmaer, *Phys. Rev. B* **62**, 15764 (2000).
- [25] T.-I. Jeon and D. Grischkowsky, *Phys. Rev. Lett.* **78**, 1106 (1997).
- [26] J. B. Baxter and C. A. Schmuttenmaer, *Phys. Rev. B* **80**, 235205 (2009).
- [27] X. Ai, M. C. Beard, K. P. Knutsen, S. E. Shaheen, G. Rumbles, and R. J. Ellingson, *J. Phys. Chem. B* **110**, 25462 (2006).
- [28] M. Walther, D. G. Cooke, C. Sherstan, M. Hajar, M. R. Freeman, and F. A. Hegmann, *Phys. Rev. B* **76**, 125408 (2007).
- [29] G. M. Turner, M. C. Beard, and C. M. Schmuttenmaer, *J. Phys. Chem. B* **106**, 11716 (2002).
- [30] M. C. Beard, G. M. Turner, J. E. Murphy, O. I. Micic, M. C. Hanna, A. J. Nozik, and C. A. Schmuttenmaer, *Nano. Lett.* **3**, 1695 (2003).
- [31] J. B. Baxter and C. A. Schmuttenmaer, *J. Phys. Chem. B* **110**, 25229 (2006).
- [32] D. G. Cooke, A. N. MacDonald, A. Hryciw, J. Wang, Q. Li, A. Meldrum, and F. A. Hegmann, *Phys. Rev. B* **73**, 193311 (2006).
- [33] L. V. Titova, T. L. Cocker, D. G. Cooke, X. Wang, A. Meldrum, and F. A. Hegmann, *Phys. Rev. B* **83**, 085403 (2011).

-
- [34] H. Němec, J. Rochford, O. Taratula, E. Galoppini, P. Kužel, T. Polívka, A. Yartsev, and V. Sundström, *Phys. Rev. Lett.* **104**, 197401 (2010).
- [35] C. F. Klingshirn, *Semiconductor Optics* (Springer, Berlin Heidelberg, 2006).
- [36] R. Kubo, *J. Phys. Soc. Jpn.* **12**, 570 (1957).
- [37] R. P. Budoyo, Ph.D. thesis, Wesleyan University, Middletown, USA, 2008.
- [38] A. Pashkin, M. Kempa, H. Němec, F. Kadlec, and P. Kužel, *Rev. Sci. Instrum.* **74**, 4711 (2003).
- [39] H. Němec, A. Pashkin, P. Kužel, M. Khazan, S. Schnüll, and I. Wilke, *J. Appl. Phys.* **90**, 1303 (2001).
- [40] N. Klein, P. Lahl, U. Poppe, F. Kadlec, and P. Kužel, *J. Appl. Phys.* **98**, 014910 (2005).
- [41] H.-T. Chen, R. Kersting, and G. C. Cho, *Appl. Phys. Lett.* **83**, 3009 (2003).
- [42] A. Dreyhaupt, S. Winnerl, T. Dekorsy, and M. Helm, *Appl. Phys. Lett.* **86**, 121114 (2005).
- [43] D. H. Auston, K. P. Cheung, and P. R. Smith, *Appl. Phys. Lett.* **45**, 1984 (1984).
- [44] A. Nahata, A. S. Weling, and T. F. Heinz, *Appl. Phys. Lett.* **69**, 2321 (1996).
- [45] C. Winnewisser, P. U. Jepsen, M. Schall, V. Schyja, and H. Helm, *Appl. Phys. Lett.* **70**, 3069 (1997).
- [46] G. Gallot and D. Grischkowsky, *J. Opt. Soc. Am. B* **16**, 1204 (1999).
- [47] M. J. Tauber, R. A. Mathies, X. Chen, and S. E. Bradforth, *Rev. Sci. Instr.* **74**, 4958 (2003).
- [48] L. Duvillaret, F. Garet, and J.-L. Coutaz, *Appl. Opt.* **38**, 409 (1999).
- [49] P. Kužel, H. Němec, F. Kadlec, and C. Kadlec, *Opt. Express* **18**, 15338 (2010).
- [50] L. Duvillaret, F. Garet, and J.-L. Coutaz, *IEEE J. Selected Topics in Quantum Electron.* **2**, 739 (1996).
- [51] P. Kužel and J. Petzelt, *Ferroelectrics* **239**, 949 (2000).
- [52] A. Pashkin, E. Buixaderas, P. Kužel, M.-H. Liang, C.-T. Hu, and I.-N. Lin, *Ferroelectrics* **254**, 113 (2001).

- [53] M. C. Beard and C. A. Schmuttenmaer, *J. Chem. Phys.* **114**, 2903 (2001).
- [54] P. Kužel, F. Kadlec, and H. Němec, *J. Chem. Phys.* **127**, 024506 (2007).
- [55] H. Němec, F. Kadlec, and P. Kužel, *J. Chem. Phys.* **117**, 8454 (2002).
- [56] H. Němec, F. Kadlec, S. Surendan, P. Kužel, and P. Jungwirth, *J. Chem. Phys.* **122**, 104503 (2005).
- [57] H. Němec, F. Kadlec, C. Kadlec, P. Kužel, and P. Jungwirth, *J. Chem. Phys.* **122**, 104504 (2005).
- [58] T. Minami, *Semicond. Sci. Technol.* **20**, S35 (2005).
- [59] D. Fattakhova-Rohlfing, T. Brezesinski, J. Rathousky, A. Feldhoff, T. Oekermann, M. Wark, and B. Smarsly, *Adv. Mater.* **18**, 2980 (2006).
- [60] Y. Furubayashi, T. Hitosugi, Y. Yamamoto, K. Inaba, G. Kinoda, Y. Hirose, T. Shimada, and T. A. Hasegawa, *Appl. Phys. Lett.* **86**, 252101 (2005).
- [61] Y. Liu, J. M. Szeifert, J. M. Feckl, B. Mandlmeier, J. Rathousky, O. Hayden, D. Fattakhova-Rohlfing, and T. Bein, *ACS Nano* **4**, 5373 (2010).
- [62] R. J. Gonzalez, R. Zallen, and H. Berger, *Phys. Rev. B* **55**, 7014 (1997).
- [63] S. R. Elliott, *Adv. Phys.* **36**, 135 (1987).
- [64] A. Pashkin, Ph.D. thesis, Charles university in Prague, Czech republic, 2004.
- [65] H. Němec, Z. Mics, M. Kempa, P. Kužel, O. Hayden, Y. Liu, T. Bein, and D. Fattakhova-Rohlfing, *J. Phys. Chem. C* **115**, 6968 (2011).
- [66] B. C. Garrett, D. A. Dixon, D. M. Camaioni, D. M. Chipman, M. A. Johnson, C. D. Jonah, G. A. Kimmel, J. H. Miller, T. N. Rescigno, P. J. Rossky, S. S. Xantheas, S. D. Colson, A. H. Laufer, D. Ray, P. F. Barbara, D. M. Bartels, K. H. Becker, K. H. Bowen, S. E. Bradforth, I. Carmichael, J. V. Coe, L. R. Corrales, J. P. Cowin, M. Dupuis, K. B. Eisenthal, J. A. Franz, M. S. Gutowski, K. D. Jordan, B. D. Kay, J. A. LaVerne, S. V. Lymar, T. E. Madey, C. W. McCurdy, D. Meisel, S. Mukamel, A. R. Nilsson, T. M. Orlando, N. G. Petrik, S. M. Pimblott, J. R. Rustad, G. K. Schenter, S. J. Singer, A. Tokmakoff, L.-S. Wang, C. Wittig, and T. S. Zwier, *Chem. Rev.* **105**, 355 (2005).
- [67] B. Boudaïffa, P. Cloutier, D. Hunting, M. A. Huels, and L. Sanche, *Science* **287**, 1658 (2000).

- [68] T. Frigato, V. Joost, B. Schmidt, C. Schutte, and P. Jungwirth, *J. Phys. Chem. A* **112**, 6125 (2008).
- [69] O. Marsalek, F. Uhlig, T. Frigato, B. Schmidt, and P. Jungwirth, *Phys. Rev. Lett.* **105**, 043002 (2010).
- [70] X. Chen and S. E. Bradforth, *Annu. Rev. Phys. Chem.* **59**, 203 (2008).
- [71] P. Kambhampati, D. H. Son, T. W. Kee, and P. F. Barbara, *J. Phys. Chem.* **106**, 2374 (2002).
- [72] J. V. Coe, A. D. Earhart, M. H. Cohen, G. J. Hoffman, H. W. Sarkas, and K. H. Bowen, *J. Chem. Phys.* **107**, 6023 (1997).
- [73] J. W. Boag, *Phys. Med. Biol.* **10**, 457 (1965).
- [74] A. Baltuska, Ph.D. thesis, University of Groningen, 2000.
- [75] C. L. Thomsen, D. Madsen, S. R. Keiding, J. Thogersen, and O. Christiansen, *J. Chem. Phys.* **110**, 3453 (1999).
- [76] D. H. Son, P. Kambhampati, T. W. Kee, and P. F. Barbara, *Chem. Phys. Lett.* **342**, 571 (2001).
- [77] H. R. Zelsmann, *J. Mol. Struct.* **350**, 95 (1995).
- [78] Z. Mics, P. Kužel, P. Jungwirth, and S. E. Bradforth, *Chem. Phys. Lett.* **465**, 20 (2008).
- [79] D. M. Bagnall, Y. F. Chen, Z. Zhu, T. Yao, S. Koyama, M. Y. Shen, and T. Goto, *Appl. Phys. Lett.* **70**, 2230 (1997).
- [80] U. Ozgur, Y. I. Alivov, C. Liu, A. Teke, M. A. Reshchikov, S. Dogan, V. Avrutin, S. J. Cho, and H. Morkoc, *J. Appl. Phys.* **98**, 041301 (2005).
- [81] R. L. Hoffman, B. J. Norris, and J. F. Wager, *Appl. Phys. Lett.* **82**, 733 (2003).
- [82] J. B. Baxter and E. S. Aydil, *Appl. Phys. Lett.* **86**, 053114 (2005).
- [83] M. Law, L. E. Greene, J. C. Johnson, R. Saykally, and P. D. Yang, *Nature Mater.* **4**, 455 (2005).
- [84] D. C. Olson, J. Piris, R. T. Collins, S. E. Shaheen, and D. S. Ginley, *Thin Solid Films* **496**, 26 (2006).
- [85] C. Klingshirn, *Chem. Phys. Chem.* **8**, 782 (2007).

-
- [86] O. Taratula, E. Galoppini, D. Wang, D. Chu, Z. Zhang, H. Chen, G. Saraf, and Y. Lu, *J. Phys. Chem. B* **110**, 6506 (2006).
- [87] M. A. M. Versteegh, T. Kuis, H. T. C. Stoof, and J. I. Dijkhuis, *Phys. Rev. B* **84**, 035207 (2011).
- [88] J. B. Baxter and C. A. Schmuttenmaer, *Phys. Rev. B* **80**, 235206 (2009).
- [89] E. Hendry, Ph.D. thesis, University of Amsterdam, 2005.
- [90] F. Wang, J. Shan, M. A. Islam, I. P. Herman, M. Bonn, and T. F. Heinz, *Nature Mat.* **5**, 861 (2006).
- [91] S. Taunier, J. Siex-Kurdi, P. P. Grand, A. Chomon, O. Ramdani, L. Parissi, P. Panheleux, N. Naghavi, C. Hubert, M. Ben-Faraha, J. P. Fauvarque, J. Connolly, O. Roussel, P. Morgensen, E. MAhe, J. F. Guillemoles, D. Lincot, and O. Kerree, *Thin Solid Films* **480-481**, 526 (2005).
- [92] P. Němec, I. Němec, P. Nahálková, K. Knížek, and P. Malý, *J. Cryst. Growth* **240**, 484 (2002).
- [93] S. Ninomiya and S. Adachi, *J. Appl. Phys.* **78**, 1183 (1995).
- [94] M. Balkanski and J. J. Hopfield, *Phys. Stat. Sol.* **2**, 623 (1962).
- [95] J. J. Hopfield and D. G. Thomas, *Phys. Rev.* **122**, 35 (1961).
- [96] D. L. Rode, *Phys. Rev. B* **2**, 10 (1970).
- [97] I. Robel, R. Gresback, U. Kortshagen, R. D. Schaller, and V. I. Klimov, *Phys. Rev. Lett.* **102**, 177404 (2009).
- [98] V. I. Klimov, C. J. Schwarz, D. W. McBranch, C. A. Leatherdale, and M. G. Bawendi, *Phys. Rev. B* **60**, 2177 (1999).
- [99] S. Juodkazis, E. Bernstein, and J. C. Plenet, *Opt. Comm.* **148**, 242 (1998).
- [100] G. Hodes, A. Albu-Yaron, F. Decker, and P. Motisuke, *Phys. Rev. B* **36**, 4215 (1987).